2018-04-26

Development and experimental validation of a CFD model for Pd-based membrane technology in H2 separation and process intensification

Rui Ma

Development and experimental validation of a CFD model for Pd-based membrane technology in H_2 separation and process intensification

by

Rui Ma

A Dissertation

Submitted to the faculty of the

Worcester Polytechnic Institute

In partial fulfillment of the requirement for the

Degree of Doctor of Philosophy

In Chemical Engineering

by

April, 2018

APPROVED BY

Dr. Anthony Dixon, Advisor

Dr. Nikolaos K. Kazantzis, Committee Member

Dr. Michael T. Timko, Committee Member

Dr. John M. Sullivan, Committee Member

Acknowledgement

With my sincere appreciation, I want to give my special thanks to my advisors Professor Dixon and Professor Ma. I am very lucky to have both of them as my advisors in research and mentors in my life. I want to thank Professor Dixon for his guidance, selfless support and endless patience. As a prestigious researcher, he loves research and at the same time so easy going with the student. As an advisor, he stands on his students' point of view to guide us when we are facing questions not only in research but also with our career. I also want to thank Professor Ma for giving me this opportunity to do my PhD at WPI. Professor Ma is a highly respected scholar; he dedicated his career to the study of palladium membrane, I am proud to be one of his students. This experience has opened a new chapter in my life and has brought me a lot of possibilities in my life. Further acknowledgement goes to my funding source Department of Energy for making this project possible.

I want to give my special thanks to Professor Castro-Dominguez, we worked closely during the first two years of my PhD. He guided me through my toughest times when I was lost about research and about my path. I enjoyed all of our discussions and the pace we have for the research, our efficient work style established many publications and hopefully more to come. I also want to thank Professor Mardilovich, for his wise suggestions for my research.

Special thanks to my committee members, Professor Timko, Professor Sullivan and Professor Kazantzis. Thank you very much for all your advice and suggestions of my research.

I want to thank all the members of Chemical Engineering Department, especially Professor Kazantzis and Professor Kmiotek for being such great mentors for us. Also, thank you Felicia and Tiffany for all your help during the past five years!

Additionally, I want to thank Monica and Bo for being such amazing manager and supervisor at Praxair during my internship, I learned a lot during the summer there.

To my lab mates, Liang-Chih Ma, Behnam Partopour and Yan Wu, I want to thank you for your company and your support during the 5 years. I really enjoyed our time together. To my friends, Xue, Sangshan, Anqi, Satish, Lida, Shi, Sarah, Zhiru, my boyfriend Kyle. I cherish all the time we spend together, thank you for making my life easier and happier.

Last but not the least, I want to thank my Parents Shuqin Liu and Shuqing Ma, my aunt Shudong and my uncle Lin; you are my dearest mentors and I love you so much!

Abstract

Syngas production and hydrogen separation technologies are very mature, and also extremely important for energy and chemical industries. Furthermore, these processes are the most expensive elements for many applications such as hydrogen production from renewable sources. Enhancing or intensifying these very mature technologies is very challenging, but would have tremendous impact on the performance and economics of many processes.

Traditional Integrated Gasification Combined Cycle (IGCC) for syngas production need to include a carbon capture process in order to regulate their carbon dioxide emission as more and more countries and regions have implemented carbon tax policy. Integration of this process with Pd membrane has long been considered a key component to make it more feasible. With these two technologies combined together, we can produce high purity hydrogen while capturing carbon dioxide and toxic gases from the syngas product. Besides, although manufacturing the membrane reactor is expensive, after considering the carbon tax factor, it actually is more economically preferable compare with the traditional Pressure Swing Adsorption (PSA) process.

Most research on Pd membrane technology has been conducted at lab scale; nonetheless, the contribution of a palladium membrane technology to economic and societal development requires its commercialization, diffusion and utilization. To generate enough incentives for commercialization, it is necessary to demonstrate the scalability and robustness of the membranes in industrial settings. Consequently, a multitube membrane module suitable for IGCC system was designed and manufactured and sent to National Carbon Capture Center (NCCC) for testing. This work developed a Computational Fluid Dynamics (CFD) model for the module and validated the model utilizing the pilot-scale experimental data generated under industrial conditions. The model was then up-scaled and used to determine the intrinsic phenomena of palladium membrane scale up. This study reveals the technical/engineering requirements for the effective design of large-scale multitube membrane modules. Mass transfer limitations and concentration polarization effects were studied quantitatively with the

developed model. Methods for diminishing the concentration polarization effect were proposed and tested through the simulations such as i) increasing convective forces and ii) designing baffles to create gas recirculation. For scaled-up membrane modules, mass transfer limitation is an important parameter to consider as large modules showed severe concentration polarization effects.

IGCC systems produce H_2 from coal combustion; other ways of H_2 production include steam-reforming processes, using natural gas or bio-ethanol as the reactant. The product contains a mixture of H_2, CH_4, CO, CO_2 and steam. Thus, steam-reforming processes are often followed by a Pressure Swing Adsorption (PSA) unit in order to obtain pure hydrogen. Palladium membrane, on the other hand, can be integrated with steam-reforming processes and achieve the simultaneous production and purification of H_2 in a single unit by reaching process intensification. Higher H_2 production rate can be reached by process intensification as one of the products H_2 is constantly being removed. Temperature control is a very important topic in steam reforming processes, as the reaction is overall highly endothermic; although implementing an in-unit membrane improves H_2 production rate, it also makes the temperature control more difficult as the reaction equilibrium is altered by the removal of one of the products H_2. Hereby, an experimental study of catalytic membrane reactor (CMR) was carried out along with both isothermal and non-isothermal CFD simulations that are validated by the experimental data in order to visualize the temperature distribution inside the reactor and understand the influence of the operating conditions including temperature, pressure and the sweep gas flow patter on the permeate side.

Executive Summary

Palladium (Pd) membrane is an efficient technology to obtain high purity hydrogen for industrial applications. Computational Fluid Dynamics (CFD) simulations made it possible for deeper understanding and further optimization of H_2 separation processes with Pd membranes. This study provided insight into the performance of palladium membrane modules that can be implemented into the Integrated Gasification Combined Cycle (IGCC) along with the study of Steam Reforming Reactions with Catalytic Membrane Reactors (CMRs).

1. Multitube membrane module for H_2 separation from syngas

Coal combustion through IGCC systems produces syngas with components including H_2, N_2, CO, CO_2 and H_2O. Pure H_2 can be obtained by implementing a Pd membrane module with the system. Most research on Pd membrane modules has been conducted at lab scale; nonetheless, the contribution of a palladium membrane technology to economic and societal development requires its commercialization, diffusion and utilization. To generate enough incentives for commercialization, it is necessary to demonstrate the scalability and robustness of the membranes in industrial settings. Thus, a seven-tube palladium membrane module suitable for IGCC systems (Fig s1.) with a total surface area of 1050 cm^2 was designed and manufactured at WPI and tested at National Carbon Capture Center (NCCC).

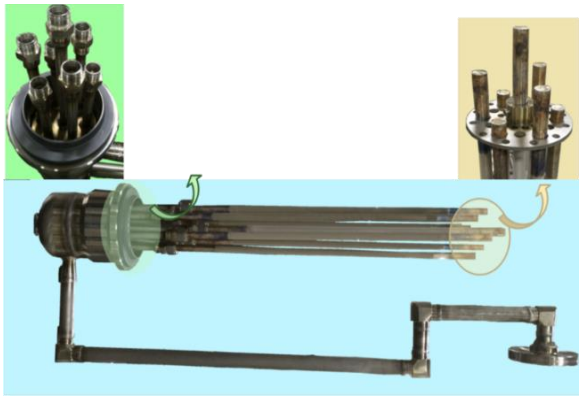

Fig s1. Seven-tube membrane module experimental set-up

Three-dimensional CFD simulations (Fig s2.) were developed and validated utilizing the pilot-scale experimental data generated under industrial conditions. Hydrogen concentration

polarization cross-section plot allows us to observe the concentration polarization effect visually. Along with the model, concentration polarization coefficient (CPC) and effective average CPC (EAC) were defined to measure the concentration polarization effect quantitatively.

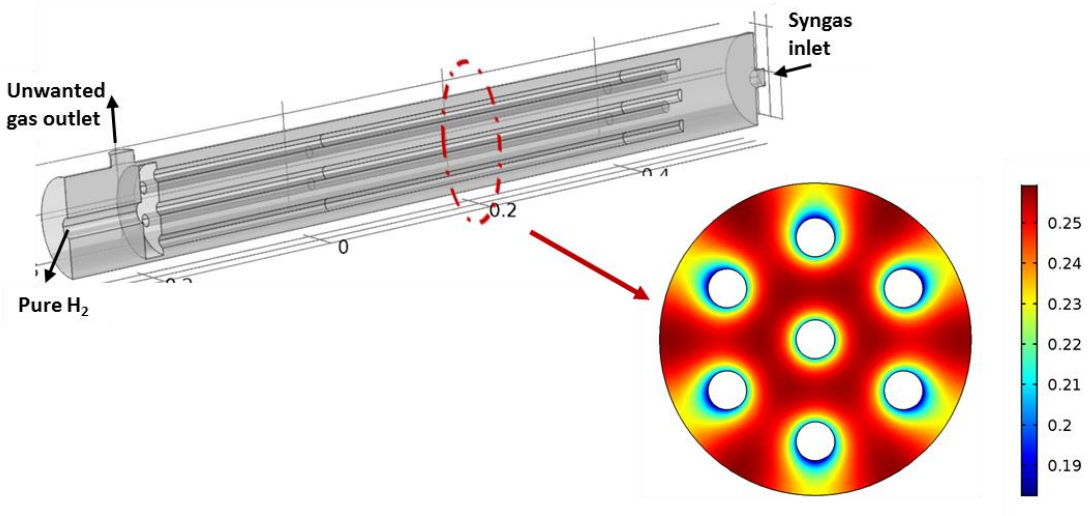

Fig s2. CFD simulation geometry and hydrogen concentration plot at cross section

Concentration polarization effect is observed and is quite strong at the front end of the membrane as this section has the highest partial pressure difference. Afterwards, concentration polarization increases steadily (Fig s3.). Higher convective force effectively reduces the concentration polarization effect by reducing the thickness of the boundary layer.

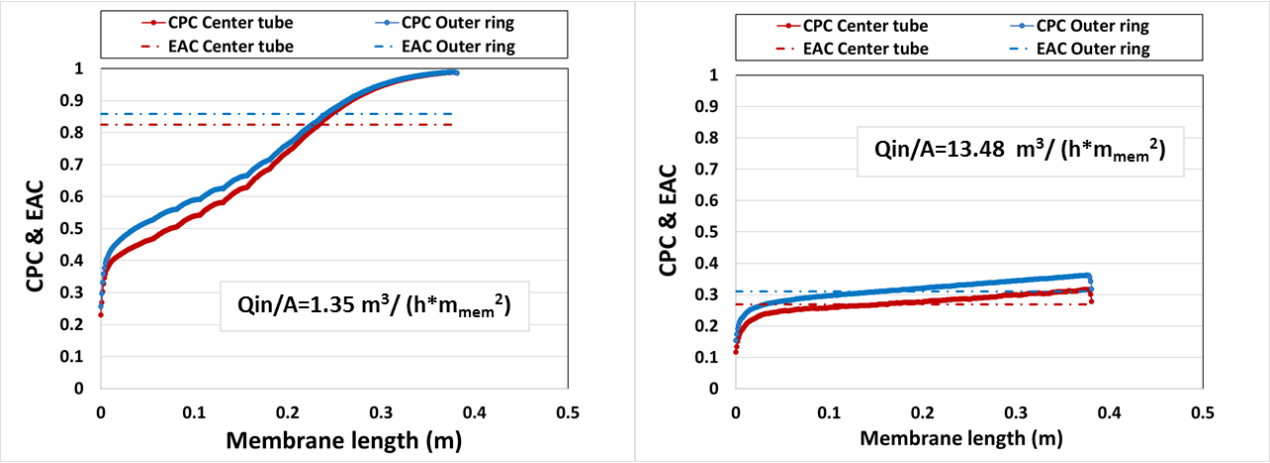

Fig s3. Concentration polarization effect of modules at different flow rate conditions

Another way to reduce concentration polarization is to add baffles to the module referencing the geometry of a shell and tube heat exchanger (Fig s4).

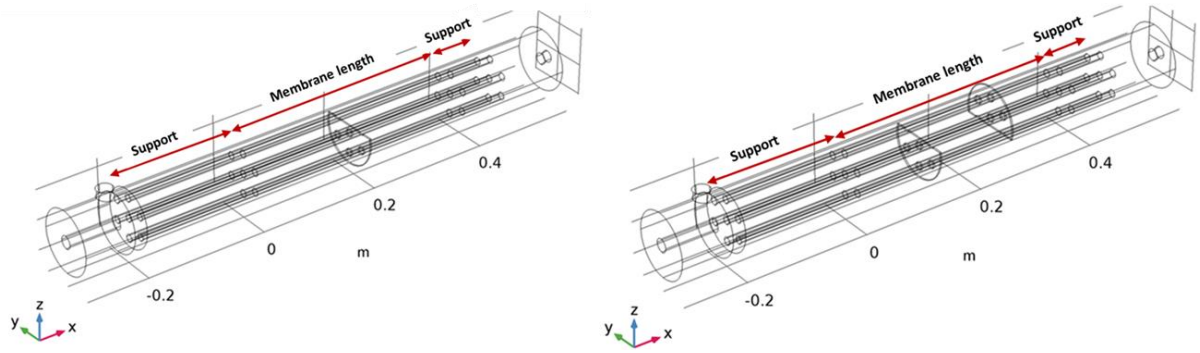

Fig s4. Geometry of membrane modules with one and two baffles

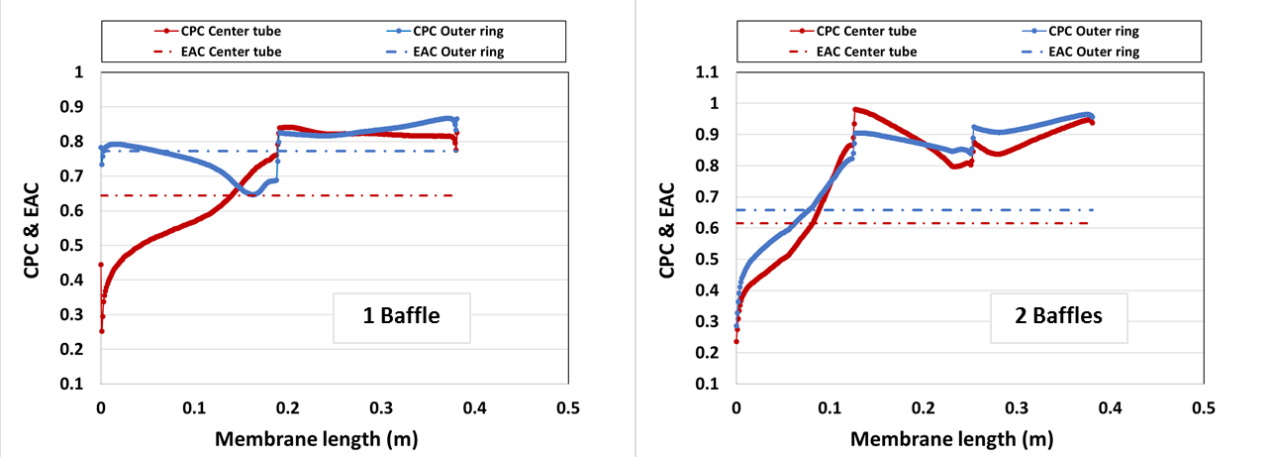

Fig s5. Concentration polarization effect of modules with baffles @ Qin/A = 1.35 $m^3/(h*m_{mem}^2)$

Between the two methods, adding baffles to the module is preferred as increasing the feed flow rate also leads to a lower hydrogen recovery, while adding baffles can reduce the concentration polarization effect without sacrificing the hydrogen recovery.

A further scaled-up module with 19 tubes is studied as well by adding another ring of membrane tubes in the module (Fig s6.). The module showed a higher concentration polarization effect, which also decreased by increasing convective force. Furthermore, a tube-to-tube performance analysis was carried out in order to understand the efficiency of each tube, as one of the disadvantage of larger scale is to potentially waste the newly added membrane surface area. The result shows that the outer layer of tubes has a lower hydrogen

flux through the membrane, and the effect is less severe at higher flow rate conditions as more recirculation is generated while the flow is directed across the membrane tubes.

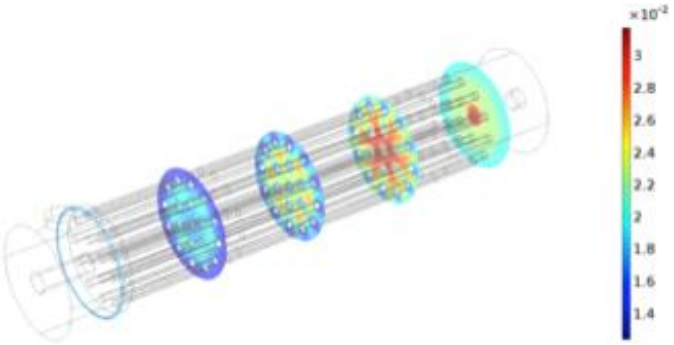

Fig s6. H_2 concentration distribution of 19-tube membrane module

2. Steam reforming in catalytic membrane reactors

As another major method of H_2 production, steam-reforming processes using natural gas and bio-ethanol were studied. Catalytic membrane reactors can achieve the simultaneous production and purification of H_2 in a single unit and increase H_2 production rate by reaching process intensification. Temperature control is an important topic for these highly endothermic processes, thus, experiments along with CFD simulations were carried out in order to understand the behavior of these processes and further optimize them.

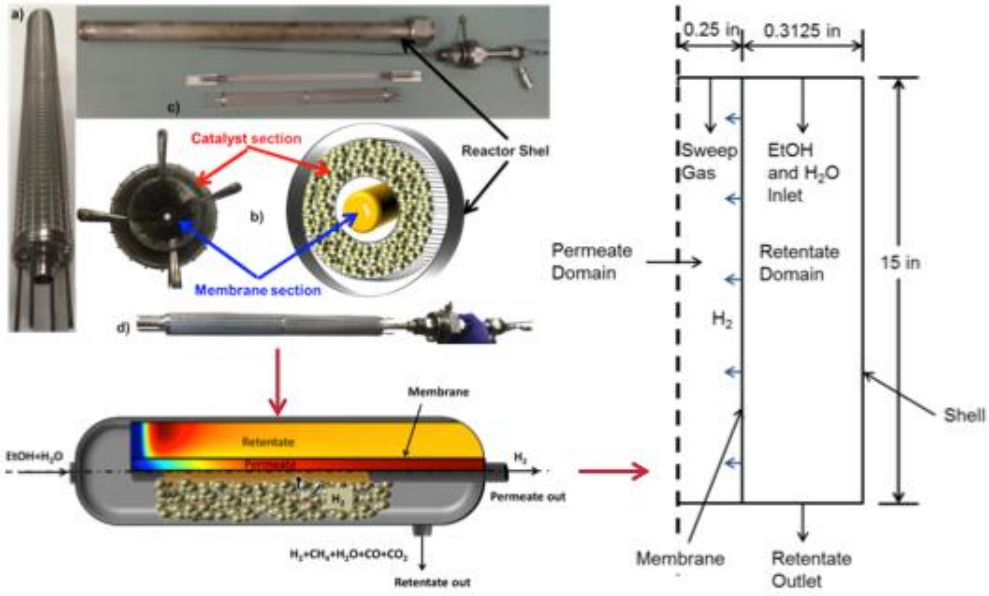

Fig s7 Experimental and CFD simulation set-up

For the ethanol-steam-reforming process, the experiment and simulation set up is shown above. The experiment was operated for 300 hours and shows a 100% conversion of ethanol. The simulation has an accuracy of 91% after the validation with the experimental data. The benefit of process intensification is proved by comparing CMR with traditional packed bed reactor; higher pressure and membrane permeance also enhances this improvement.

From the non-isothermal simulation, a relatively large “cold-spot” is observed, which is a disadvantage for the process as methanation is observed from the individual reaction analysis. Using counter-current sweep gas flow pattern can efficiently improve the temperature control.

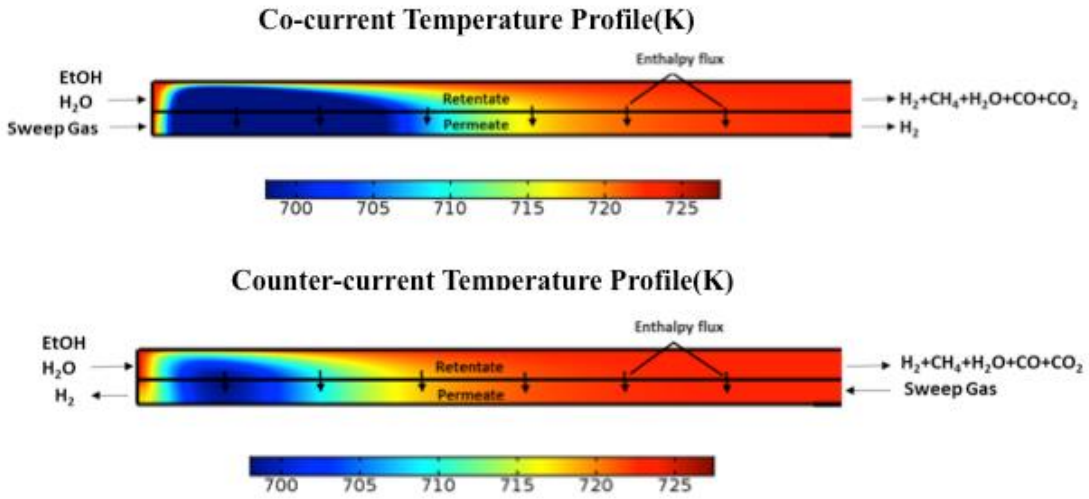

Fig s8. Temperature profile of ESR with CMR with different sweep gas flow pattern

In addition to the ethanol-steam-reforming process, methane-steam-reforming (MSR) and water-gas-shift reaction (WGS) with CMR were also studied by exploring the method of two catalysts packing in series. The performance of the CMR with two catalysts (MSR & WGS catalysts) in series was evaluated by comparing 1) a conventional packed bed reactor (PBR) with MSR catalyst, 2) a PBR with five layers of the two catalysts packed in series (Fig s9.). For the PBR, a stainless steel pipe was used instead of a membrane tube.

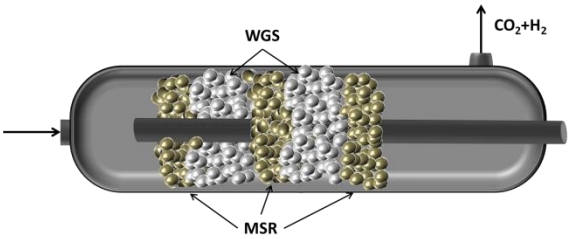

Fig s9. Schematic of the catalyst distribution throughout the PBR reactor.

It was found that the dual-catalyst CMR module showed a significant reduction in the CO content, which was shown to be the result of the subsequent “packing step” with the WGS catalyst introduced in the module design. Notice that palladium membranes are capable of operating at temperatures between 300-600 °C, matching with the temperature range of high temperature WGS catalysts (310-450 °C). Traditionally, low temperature WGS also is needed in order to reach a higher CO conversion, as the reaction is exothermic. However in CMRs, it is no

longer required as high CO conversion can be achieved through a single CMR unit as a result of process intensification.

3. Conclusion remarks

This work successfully developed a 3-D CFD model for a pilot-scale membrane module suitable for IGCC system and provided insights for large-scale membrane module design. Radial mass transfer limitations and the tube-to-tube variation must be thoroughly analyzed, as they are the main issue while scaling up the membrane modules. Furthermore, the work explored steam-reforming processes with catalytic membrane reactors, through both experimental and simulation study. The advantage of the process intensification, temperature control, and catalysts packing in series are explored, evaluated technical performance of CMRs and provided insights into the process optimization.

Publication list

Published peer reviewed articles:

R. Ma, B. Castro-Dominguez, I.P. Mardilovich, A.G. Dixon, Y.H. Ma, Experimental and Simulation Studies of the Production of Renewable Hydrogen through Ethanol Steam Reforming in a Large-Scale Catalytic Membrane Reactor, Chem. Eng. J. 303 (2016) 302-313

B. Castro-Dominguez, I.P. Mardilovich, L.C. Ma, R. Ma, A. G. Dixon, N. Kazantzis, Y.H. Ma, Integration of Methane Steam Reforming and Water Gas Shift Reaction in a Pd/Au/Pd-based Catalytic Membrane Reactor for Process Intensification, Membranes. (2016) 6(3), 44

B. Castro-Dominguez, I.P. Mardilovich, R. Ma, N.K. Kazantzis, A.G. Dixon, Y.H. Ma, Performance of a Pilot-scale Multitube Membrane Module under Coal-Derived Syngas for Hydrogen Separation, J. Membrane Sci. 523 (2017) 515- 523

R. Ma, B. Castro-Dominguez, I.P. Mardilovich, A.G. Dixon, Y.H. Ma, CFD Study of Heat and Mass Transfer in Ethanol Steam Reforming in a Catalytic Membrane Reactor. Int. J. Hydrogen Energy. 43 (2018) 7662-7674

In preparation:

R. Ma, B. Castro-Domingues, A.G. Dixon, Y.H. Ma, Scalability of Multitube Membrane Modules for Hydrogen Separation: Technical Considerations, Issues and Solutions. Ready for submission to Journal of Membrane Science

Selected Conference presentations:

R. Ma, B. Castro-Dominguez, I.P. Mardilovich, N.K Kazantzis, A.G. Dixon, Y.H. Ma, Non-isothermal CFD Study of Ethanol Steam Reforming in a Catalytic Membrane Reactor, 2017 AICHE Annual Meeting, Minneapolis

R. Ma, B. Castro-Dominguez, I.P. Mardilovich, N.K Kazantzis, A.G. Dixon, Y.H. Ma, CFD Analysis of Pilot-Scale Multitube Pd Membrane Module for Hydrogen Purification from Coal-Derived Syngas, 2017 AICHE Annual Meeting, Minneapolis

R. Ma, B. Castro-Dominguez, I.P. Mardilovich, A.G. Dixon, Y.H. Ma, CFD Study of Heat and Mass Transfer in Ethanol Steam Reforming in a Catalytic Membrane Reactor, 13th International Conference on Catalysis in Membrane Reactors, Houston (2017)

R. Ma, B. Castro-Dominguez, I.P. Mardilovich, A.G. Dixon, Y.H. Ma, Experimental and Simulation Study of Ethanol Steam Reforming Reaction for Hydrogen Production in Large Scale Catalytic Membrane Reactor, 2016 AICHE Annual Meeting, San Francisco

R. Ma, B. Castro-Dominguez, I.P. Mardilovich, A.G. Dixon, Y.H. Ma, A Computational Fluid Dynamic Study of a Pilot-scale Multitube Membrane Module for Hydrogen Purification, 2016 AICHE Annual Meeting, San Francisco

R. Ma, B. Castro-Dominguez, A.G. Dixon, Y.H. Ma, Three-dimensional CFD Model of a Multitube Pd/Au Membrane Module for Hydrogen Purification, 2015 AICHE Annual Meeting, Salt Lake City

Contents

1. Introduction

As 2015 starts with the atmosphere carbon dioxide (CO_2) level reaching 400 parts per million (ppm) milestones, discussion about global warming continues. May 9, 2013, the world's CO_2 concentration passed 400ppm for the first time in 800,000 years, which covers the whole human civilization period, and the level is reached more often since then (Thompson et al. 2015). From the beginning of the Industrial Revolution, the global average temperature has risen 1.8 °F due to the greenhouse gas (Carbon dioxide: CO_2; water vapor: H_2O; methane: CH_4; nitrous oxide: N_2O) emission (Kahn et al. 2014). Over the years, ocean works as a CO_2 sink, it helps to reduce the CO_2 concentration in the atmosphere, but in the meantime, it leads to a problem of ocean acidification (Doney et al. 2009). Acidification can put the ocean ecosystem in danger since it can directly damage the shelled organisms by weakening their shells; therefore influencing the entire food-chain under and above the sea (Doney et al. 2009). To regulate the CO_2 emission, carbon tax is growing around the world, which is giving an increasing economic pressure to industries.

Greenhouse gas is mainly discharged by energy production from fossil energy carriers. Despite this well-known fact, the U.S. energy consumption is still growing 0.4% annually for the economic developing demand (U.S. Energy Information Administration (U.S. EIA) 2014). For the reasons listed above, carbon capture and sequestration (CCS) system integrated with energy producer is being intensely studied for its advantage of simultaneously generating energy source or clean energy carrier and reducing CO_2 emission. Among all the CCS integrated systems, hydrogen (H_2) production plants with catalytic membrane reactors (HP-CMR) attracts most interest for its high carbon capture efficiency (reduce CO_2 emission by 70% compared to traditional technologies) as well as a significant reduction of coal-feed demand due to its advantage in process intensification (Ma et al 2015).

H_2 takes part in a lot of chemical industrial processes such as ammonia and methanol production, fossil fuel upgrading process, oil saturating process and also H_2 driven proton exchange membrane fuel cells. Besides, H_2 serves as an efficient and clean energy carrier which

has the highest energy density of 120.7kJ/g (Akpan et al. 2007). In the discussion of clean fuel development for conventional crude oil replacement, H_2 gains more and more attention as an energy carrier and as a liquid fuel. Compared with the limitation of traditional fuel, hydrogen is an environmentally-friendly fuel as the only product of hydrogen combustion is pure water (Iulianelli et al. 2016). Some of the benefits of building a H_2 economy include: environmentally-friendly properties when oxidized as a fuel, availability of multiple transportation methods, large storage capacity (unlike electricity), applicability as fuel or for electrical generation, and potential production through multiple sources/pathways (Rosen et al. 2015). Currently, the production of H_2 relies heavily on fossil fuel-based sources such as natural gas and coal, but can potentially extended to renewable sources such as biomass. According to the U.S. Office of Energy Efficiency and Renewable Energy (U.S. Office of Energy Efficiency and Renewable Energy n.d.), methane steam reforming accounts for 95% of the H_2 produced in the United States; simultaneously, it is expected that coal gasification will be deployed in the mid-term time frame.

In order to utilize hydrogen in most of the industrial applications, ultrapure hydrogen with a purity of 99.99-99.9995% is required. As a result, in the hydrogen production process, the hydrogen purification/filtration method takes up to 50% of the entire production cost (Al-Mufachi et al. 2015; Nenoff 2006). Palladium membrane reactors are able to separate and collect hydrogen with close to 100% purity, which can be further used for other applications. In the meantime, concentrated CO_2 is collected from the other side of the membrane (retentate), which can be directly captured and sequestrated. Although these features are technically important, there are constraints which need to be addressed. Therefore, the proposed research will target the following issues: i) process scale up, ii) integration of different physical phenomena, iii) optimization of operating condition.

Currently, many lab scale studies of palladium membrane have been done; however, to actually apply this technology to industry the system requires scaling up. In this work, a pilot scale membrane reactor with seven membrane tubes is being studied. Besides, the optimization of operating conditions in multi-tube membrane modules is a complex process. The multiple physics and irregular geometries involved on these systems create a challenge for predicting

their performance. Furthermore, when reaction is introduced to the system, taking into account the non-isothermal property of the reactions as well as the varying concentration profile of each species, the system performance within the module become more difficult to predict. This requires a simulation method which can better model the performance of the reactor and thus provide valuable data before implementing this technology. In this work, CFD simulation models along with their experimental validation were developed for both multi-tube membrane system and catalytic membrane reactor for process intensification. In addition, besides making it possible to predict the performance of the reactor under different operation conditions, the simulation model also visualize the flow pattern inside the reactor and thus help to better understand the physics behind the results.

2. Literature review

2.1 Palladium membranes for hydrogen separation

2.1.1 Palladium membranes for hydrogen purification

Since Palladium (Pd) has been discovered by William Hyde Wollaston at 1803, Pd membrane tubes have been first developed by Johnson Matthey (Grashoff et al. 1983). Lab scale Pd membrane reactors for H_2 separation are developed for decades by different research groups. Pd-based membrane technology has been shown to be effective in the generation of ultrapure molecular H_2 at high fluxes, as well as facilitating the capture of CO_2 when integrated as a catalytic membrane reactor (Grashoff et al. 1983, Nenoff et al. 2006). Furthermore, it has been shown that this technology can exhibit superior economic performance compared to conventional technologies under specific market and regulatory conditions when it is integrated with different H_2 production and/or energy systems (Wellington et al. 2006; Ma et al. 2015).

Palladium was observed to have a high permeability and selectivity while used for hydrogen separation. The mechanism of the hydrogen transport through the membrane follows solution-diffusion mechanism (Ward et al. 1999; Ma et al. 2014)

1) Hydrogen transport through the gas bulk in the module/reactor to the membrane surface.
2) Reversible chemisorption of hydrogen on the membrane surface.
3) Reversible dissolution of hydrogen atoms into the palladium bulk.
4) Diffusion of hydrogen atoms through the palladium bulk.
5) Migration of hydrogen atoms from the palladium bulk to the membrane surface with lower hydrogen partial pressure.
6) Recombination and desorption of hydrogen from the membrane surface.
7) Hydrogen transport into the gas bulk from the membrane surface.

The above process takes place exclusively for hydrogen, thus hydrogen selectivity of palladium membrane can reach infinity theoretically. Considering the CO_2 emission regulations like carbon

tax, when integrated with energy generation systems like Integrated Gasification Combined Cycle (IGCC) or catalytic membrane reactors (CMRs), palladium membrane technology is economically preferred. Compared with traditional pressure swing adsorption (PSA) method, using palladium membrane for hydrogen separation can reduce the capital cost by 26% while considering the carbon regulation. Currently, studies of the palladium membranes mainly focused on lab scale tests and have shown promising results (Lu et al. 2007, Catalano et al. 2012, Guazzone et al. 2012). In order to apply this technology, larger scale modules with larger membrane surface area need to be studied for evaluating the membrane module commercialization potential. Considering the manufacturing cost of the membrane module, larger membrane surface area to module volume ratio is desired (Sanders et al. 2013). However, studies of multitube membrane module under real industrial conditions are very limited. Mardilovich et al. (2015) reported a study of a seven-tube palladium alloy membrane module that can be used to separate pure hydrogen from coal-derived syngas. In the study, membranes with different palladium-alloys were tested first under the condition of H_2/N_2 mixture and syngas feed, 450°C and 12.6 atm. The membranes were tested for 4275 hours in total and maintained a satisfying stability and hydrogen product purity in the range of 99.95% - 99.00%. Due to the presence of sulfur in the syngas, the membrane permeance decreased during the process. Furthermore, it was observed that for Pd, Pd-Au, Pd-Pt and Pd-Au-Pt alloys, Pd-Au alloy has the best performance, which agrees with the literature (Chen et al. 2010, Lu et al. 2007, Guazzone et al. 2013) The operating temperature (450°C) is in between the Au Tamman temperature (395°C) and Pd Tamman temperature (641°C), and Au has a higher mobility at this temperature. Pd remains immobile at 450 °C while Au diffuses into the Pd layer and fill in the defects on that developed during the operation. Tosti et al. (2008) designed a finger-like membrane reactor with 19 membrane Pd-Ag membrane tubes for ethanol steam reforming. The reactor has a total membrane surface area of 1490 cm^2 and is able to produce hydrogen with a rate of 6L/min. Diniz da Costa et al. (2009) designed a multitube silica membrane for water gas shift reaction, which can produce hydrogen product with a 98% purity. Parsley et al. (2014) studied a multitube carbon molecular sieve membrane with 86-tube and 7600 cm^2 surface area. The module was tested under real industrial coal-derived syngas

condition and yield hydrogen product with 90% purity. Besides, Yun et al. (2011) and Ravanchi et al. (2009) summarized the development and the applications of palladium membranes, which are very informative.

2.1.2 Mass transfer limitation

The mass transfer limitation of the retentate side, concentration polarization, is caused by the rapid depletion of H_2 molecules at the surface of the membrane (Mori et al. 2007). This depletion is caused by the difference in membrane permeance (high) and H_2 diffusion (low). The driving force in palladium membranes is the H_2 partial pressure difference across the membrane; consequently, as the concentration of H_2 reduces at the membrane surface in the retentate, the performance of the membrane declines downstream. Concentration polarization is an often-neglected topic, however, the effect is more significant for membranes with higher permeance. As palladium alloy membrane has infinite selectivity theoretically, it is important to study the concentration polarization effect. Methods (manipulating the operating conditions and module/reactor configuration) for improving the mass transfer of the membrane were explored (Zhang et al. 2006; Mourgues et al. 2005). For instance, Mori et al. (2007) studied the concentration polarization effect of a membrane reactor for methane stream reforming reaction and concluded that increasing the GHSV (gas hourly space velocity) by reducing the reactor radius can effectively improve the mass transfer inside the reactor and increase the methane conversion as a result. Besides, adding baffles to the module can also efficiently reduce the concentration polarization effect (Mori et al., 2007; Guazzone et al., 2012).

2.1.3 Module scale-up

Module scale-up is an important topic that can provide insight for future industrial applications. While scaling up the potential module, maintaining the same operating condition is necessary for accurate comparison (Wenten et al., 2016). Module scale-up strategies include both empirical scale-up and theoretical scale-up. Empirical scale-up studies apply the lab-scale experimental framework to a larger scale module while theoretical scale-up studies utilize simulation methods to study the differences of modules with different scales. Yang et al. (

2017) reported a scale-up study of membrane modules using numerical methods. Different operating conditions were studied, and the module's sensitivity to the operating conditions change was monitored for both scales.

2.1.4 Membrane poisoning

Membrane reactors have been widely used for separation of syngas and to carry out reactions such as reforming of hydrocarbons to produce H_2, however, when gas mixture is introduced to the system, a decrease of H_2 permeation is usually observed (Murmura et al. 2015). Two reasons have been proposed: first, concentration polarization effect lowers the H_2 partial pressure adjacent to the membrane surface; however, introducing higher feed space velocity reduces this effect. Second, components such as CO, steam, and CO_2 compete for the combining site with H_2, and restrains H_2 from binding with the membrane (Camara et al. 2002). Additionally, hydrocarbons such as methanol and ethanol may lead to a coking phenomenon on the membrane surface, which also diminishes the H_2 permeation. However, by adding more steam into the system, hydrocarbons can be oxidized and therefore membrane performance is maintained. H_2S also has a severe poisoning effect on Pd membrane, however, since in the hydrogen separation process, H_2S is always removed to protect the membrane, thus the influence of H_2S is not discussed in this section.

To analyze the influence of different components, Hou et al. (2002) developed a simulation model only considering the influence of mass transfer resistance, and studied the inhibition effect of different components by comparing the practical result to the simulation result. Through measuring the membrane permeance under combinations of CO_2 and H_2, CO and H_2, H_2O and H_2, they concluded that, among these three components, steam has the highest inhibition effect, followed by CO and then CO_2 has a negligible effect on membrane permeance as shown in the figure 2.1 (Hou et al. 2002) below.

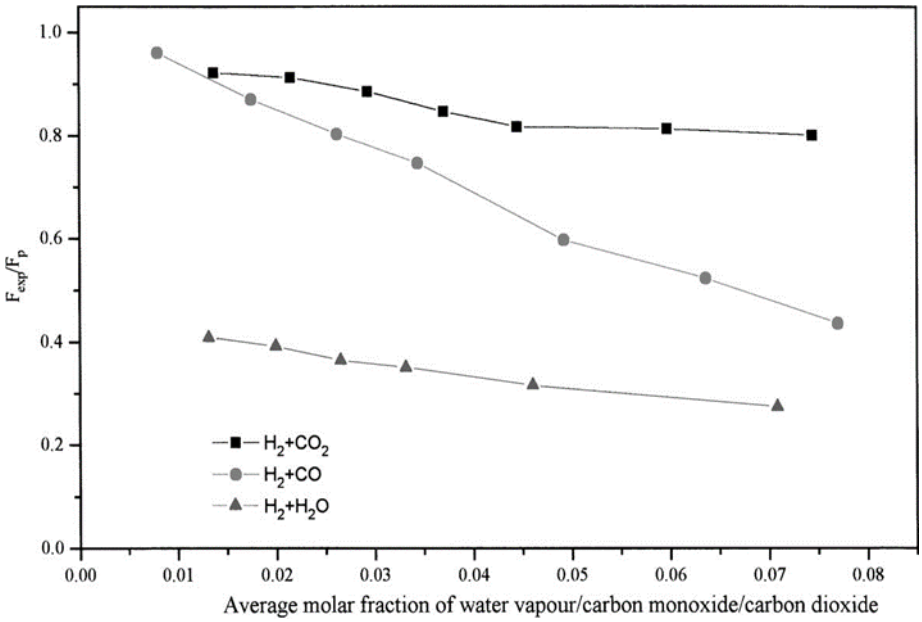

Fig 2.1 Comparison between effects of steam/ carbon monoxide/carbon dioxide on H_2 permeance (T=548K, ΔP=1bar) (Hou et al. 2002)

Temperature plays a positive role in maintaining the membrane performance, at temperature higher than 673K, for all the components, only minor inhibition influence is observed. Notice that the membrane being tested is Pd/Ag membrane with α-alumina supports.

To analyze the membrane behavior under actual coal derived syngas environment, Guazzone et al. (2013) prepared and characterized two pilot scale membranes with 200cm^2 surface areas and with the composition of Pd and Pd-Au respectively, using porous stainless steel as support. By testing for 200h and 473h respectively under the desulfurized syngas environment, both membranes show a relatively stable permeance which makes them a good candidate in industrial applications.

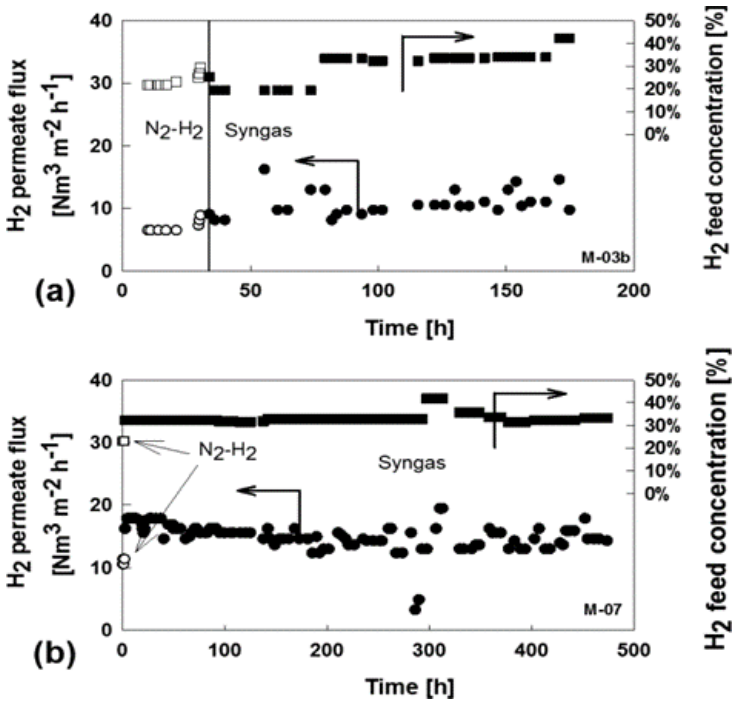

Fig 2.2 H_2 permeate flux as a function of time for (a) Pd membrane and (b) Pd-Au membrane.

As shown in Figure 2.2 (Mardilovich et al. 2015) during the test, Pd membrane shows a stable permeance of 10.7±3.1 N $m^3m^{-2}h^{-1}bar^{-0.5}$, and Pd-Au membrane shows a slight decrease of permeance from 17.2±1.8 to 14.2±2.4 N $m^3m^{-2}h^{-1}bar^{-0.5}$ due to the poisoning effect of syngas. Permeance recovers under pure H_2 atmosphere conditions. As shown in Figure 2.3 (Mardilovich et al. 2015) permeance of Pd membrane has a 78% recovery, while Pd-Au membrane gains a complete recovery.

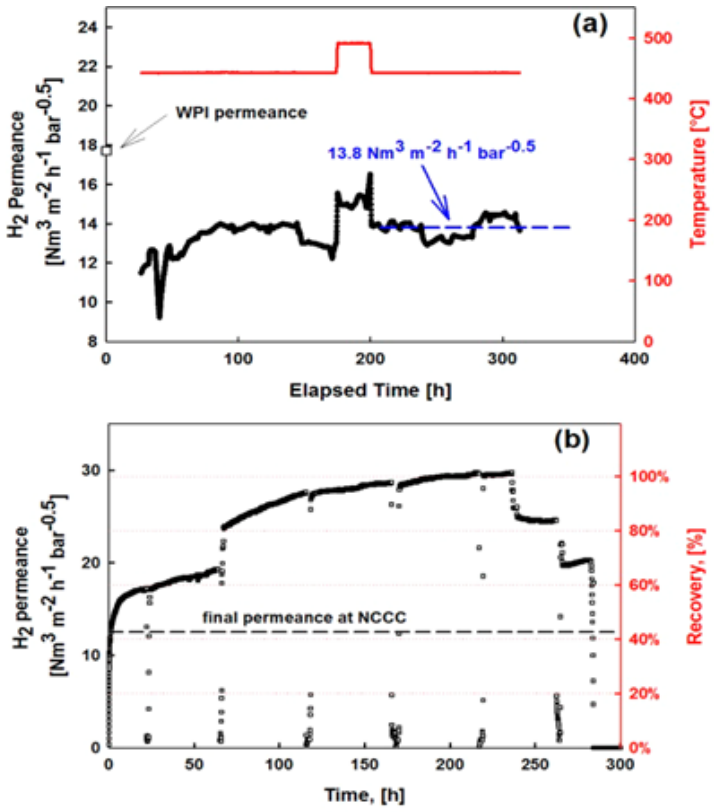

Fig 2.3 H_2 permeance as a function of time during a recovery test at WPI for (a) Pd membrane and (b) Pd-Au membrane.

Later, Mardilovich et al. (2015) prepared and tested thirteen membranes with also 200 cm^2 surface area, but with four types of compositions: Pd, Pd/Au, Pd/Pt and Pd/Au/Pt. Membranes are tested under desulfurized syngas environment for 200h, 470h, 350h and 700h respectively. The result shows that pure Pd membrane has the highest initial permeance among all the Pd alloys, and Pd-Pt shows the lowest permeance since Pt has the effect of blocking the Pd active site. However, under the syngas condition, Pd-Au shows the lowest permeance drop, while pure Pd has the highest. Also, Pd-Au membrane also shows the most stable characteristic, they can maintain >99% H_2 purity for the whole test.

2.2 Process intensification

2.2.1 Methane Steam reforming process

The diversified sources for hydrogen production have a great environmental impact. Methane steam reforming is a well-established method for hydrogen production (U.S. Office of Energy Efficiency & Renewable Energy. Available online 2016). The reaction is usually carried out under high temperature (700°C - 1000°C) for its endothermic property and a mild pressure (3-25 bar). Methane first reacts with steam to produce CO and H_2, followed by the water-gas-shift reaction, which converts CO to CO_2. The reaction products include CO and H_2 along with byproduct CO_2.

MSRI	$\mathrm{CH_4 + H_2O \leftrightarrow CO + 3H_2}$	$\Delta \mathrm{H_{298K}} = 206\ \mathrm{kJ/mol}$	(2-1)
WGS	$\mathrm{CO + H_2O \leftrightarrow CO_2 + H_2}$	$\Delta \mathrm{H_{298K}} = -41\ \mathrm{kJ/mol}$	(2-2)
MSRII	$\mathrm{CH_4 + 2H_2O \leftrightarrow CO_2 + 4H_2}$	$\Delta \mathrm{H_{298K}} = 165\ \mathrm{kJ/mol}$	(2-3)

In the reactions, methane steam reactions are highly endothermic while water-gas-shift reaction is exothermic. Traditionally, the reaction products go through pressure swing adsorption (PSA) process to produce pure hydrogen. Process intensification is a concept of combining the hydrogen separation unit with hydrogen production unit like ethanol steam reforming process (Mardilovich et al. 2015). By combining both units, one of the products hydrogen is continuously depleted from the reaction side, which is beneficial for the reaction equilibrium; in the meantime, pure hydrogen is collected from the other side of the membrane. Catalytic membrane reactor (CMR) can achieve process intensification by introducing a membrane tube inside a packed bed reactor. Specially, implementing palladium-alloy membranes to the catalytic membrane reactors has been studied due to their high hydrogen permeability and selectivity. Previously, Pd-alloy based catalytic membrane reactors were applied to the water-gas-shift reaction (Catalano et al. 2012) and methane steam reforming reactions (Patrascu et al. 2015). Furthermore, economical study of the application of catalytic membrane reactors shows a better performance under the restrictions and regulations of carbon dioxide emission (Ma et al. 2015). When a carbon capture and sequestration process is

introduced into the coal gasification process for hydrogen production, as much as 70% of greenhouse gas emission can be reduced. Studies of methane steam reforming in a catalytic membrane reactor are listed in Table 2-1.

Palladium membrane is able to operate under temperatures of 300-600 ^{o}C, which is in the temperature range of high-temperature water-gas-shift reaction 310-450 ^{o}C. High temperature water-gas-shift reaction has limited CO conversion as the reaction is exothermic, thus it is always followed by a low temperature water-gas-shift reaction. However catalytic membrane reactors can achieve a high CO conversion, so the low temperature water-gas-shift reaction is no longer needed. Furthermore, mild temperature can be used in CMRs in order to reduce coking effect as the process intensification can maintain a higher conversion. The experimental study presented in the table shows the advantage of process intensification, however few pilot scale study was published. Patrascu et al. (2015) reported the study of methane steam reforming in a large scale catalytic membrane reactor with a total membrane surface area of 175 cm^2. The reaction was operated at 525 ^{o}C and 10 bar, and was able to achieve 1.6 NL/min hydrogen permeance flux.

Table 2-1. Palladium-based catalytic membrane reactors used for Methane Steam Reforming and Water Gas Shift reactions

Membrane type	Thickness (um)	Membrane area (cm^2)	Reaction	Pressure (bar)	Steam/carbon ratio	Temperature (^oC)	Reference
Pd/Ag	50	5.3	MSR	1.22	3-9	300-500	(Gallucci et al. 2004)
Pd/Ag/PSS	10.3	10.7	MSR	1.36	3	400-550	(Shu et al. 1995)
Pd/PSS	20	60	MSR	9-20	3	400-500	(Lin et al. 2003)
Pd	4.5 - 22.5	6.3	MSR	1	3	500	(Kikuchi et al. 2000)
Pd	4-5	175	MSR	<10	2-4	525	(Patrascu et al. 2015)
Pd/Ag	200	46	MSR	1-4	2-5	300-400	(Vásquez Castillo et al. 2015)
Pd/Ag	1,000	18.5	MSR	6-10	2.9	500	(Jorgensen et al. 1995)
Pd–Ru/YSZ	5	13.28	MSR	35	3	580	(Abu El Hawa et al. 2015)
Pd	20	25	WGS	3	1-5	400	(Uemiya et al. 1991)
Pd	1.4	21.5	WGS	2	3	350	(Bi et al. 2009)
Pd- Pd/Ag	7 – 10.3	50	WGS	1-12	1.1-2.6	350-450	(Augustine et al. 2011)
Pd/Ag	25-40	15.7	WGS	1-4	7.4	200-300	(Mendes et al. 2010)
Pd	10	200	WGS	7-20	2.5-3.5	420-440	(Catalano et al. 2012)
Pd/Ag	2.2	6.8	WGS	26	5	400-450	(Peters et al. 2008)
Pd/Ag/ alumina	4.5	17-35	WGS	2	NA	400	(Fernandez et al. 2015)

2.2.2 Ethanol steam reforming process

As bio-ethanol is considered as a carbon neutral and renewable material, it is considered as one of the preferred resources for hydrogen production. In ethanol steam reforming reaction, high temperature ethanol vapor and steam react and generate hydrogen, carbon monoxide and carbon dioxide. Methane is one of the middle products, which is consumed by methane steam reforming. Typically the conversion of ethanol can reach close to 100% while the conversion of methane determines the hydrogen yield.

The kinetic properties of ESR for different catalysts have been studied throughout the literature and different mechanisms have been proposed (Murmura et al. 2015; Mas et al. 2008; Palma et al. 2012; Bshish et al. 2011; Peela et al 2011; Olafadehan et al. 2015; Patel et al. 2013; Du et al. 2011).

The overall desired reaction is:

Ethanol steam reforming:

$$C_2H_5OH + 3H_2O = 2CO_2 + 6H_2 \quad (2\text{-}4)$$

$$C_2H_5OH + H_2O = CH_4 + CO_2 + 2H_2 \quad (2\text{-}5)$$

Besides, many other possible reactions are included in the reaction scheme:

Ethanol dehydrogenation to acetaldehyde:

$$C_2H_5OH = CH_3CHO + H_2 \quad (2\text{-}6)$$

Acetaldehyde steam reforming:

$$CH_3CHO + H_2O = 2CO + 3H_2 \quad (2\text{-}7)$$

Decomposition of acetaldehyde to methane:

$$CH_3CHO = CH_4 + CO \quad (2\text{-}8)$$

Decomposition of ethanol to methane:

$$C_2H_5OH = CH_4 + CO + H_2 \quad (2\text{-}9)$$

Methane steam reforming:

$$CH_4 + H_2O = CO + 3H_2 \quad (2\text{-}10)$$

$$CH_4 + 2H_2O = CO_2 + 4H_2 \quad (2\text{-}11)$$

Decomposition of ethanol to acetone:

$$2C_2H_5OH = CH_3COCH_3 + CO + 3H_2 \quad (2\text{-}12)$$

Ethanol dehydration to ethylene:

$$C_2H_5OH = C_2H_4 + H_2O \quad (2\text{-}13)$$

Water gas shift:

$$CO + H_2O = CO_2 + H_2 \quad (2\text{-}14)$$

Ethanol cracking to methane and CO_2:

$$C_2H_5OH = 0.5CO_2 + 1.5CH_4 \quad (2\text{-}15)$$

Boudouard reaction:

$$2CO = CO_2 + C \quad (2\text{-}16)$$

The four main reactions which take place in an ethanol steam reforming process are follows: First ethanol decomposes into methane, carbon monoxide and hydrogen, followed by water gas shift (WGS) reaction where carbon monoxide is consumed by steam and produces more hydrogen. The ethanol-decomposition product methane is then converted to carbon monoxide and carbon dioxide by methane steam reforming (MSR) reaction.

ESR	$C_2H_5OH \leftrightarrow CH_4 + CO + H_2$	$\Delta H_{298K} = 49\ kJ/mol$	(2-17)
WGS	$CO + H_2O \leftrightarrow CO_2 + H_2$	$\Delta H_{298K} = -41\ kJ/mol$	(2-18)
MSR	$CH_4 + H_2O \leftrightarrow CO + 3H_2$	$\Delta H_{298K} = 206\ kJ/mol$	(2-19)
MSR	$CH_4 + 2H_2O \leftrightarrow CO_2 + 4H_2$	$\Delta H_{298K} = 165\ kJ/mol$	(2-20)

This process is traditionally carried out in packed bed reactors (Mathure et al. 2007; Zhai et al. 2010; Gallucci et al. 2010; Uriz et al. 2011; Aboudheir et al. 2006). Roldán et al. (2015) delivered a large-scale study of ethanol steam reforming in a conventional reactor. The reaction was operated under 450 °C and steam to carbon ratio of 1.5. The weight hourly space velocities used in the experiment were 1.0 h^{-1} and 2.0 h^{-1}. In this study, the ethanol conversion reached 99.7 wt%. In the traditional reactors for steam reforming process, the product will be sent to a hydrogen separation unit in order to produce high purity hydrogen. Traditional packed bed reactors have limited degrees of freedom for reactor design. One parameter that can be modified is particle diameter; however considering intra-particle diffusion and bed pressure drop, the particle diameter adjustment is restrained. Thus different reactor configurations were proposed, for example fluidized beds, micro-channels and catalytic membrane reactors which can achieve process intensification.

Some lab scale study of ethanol steam reforming with catalytic membrane reactors have been carried on and Table 1 summarizes and compares the different aspects of the studies.

Many aspects need to be studied in order to fully understand the behavior of CMRs and to achieve the best performance, for example space velocity, steam to ethanol ratio and sweep gas (Murmura et al. 2015; Tosti et al. 2008). For the system with sweep gas on permeance side, higher flow rate of sweep gas leads to a better membrane reactor performance, besides, increasing membrane permeance can also improve the hydrogen production rate (Chein et al. 2014). In the above studies in Table 2-2, Gallucci et al. (2010) carried out a simulation study of ethanol steam reforming process with Pd-Ag catalytic membrane reactor under different operating conditions. The study compared the performance of membrane reactors with traditional packed bed reactors, and showed the advantage of process intensification. The membrane reactor shows a higher ethanol conversion and a higher hydrogen selectivity as well while using Co-based catalyst kinetics in the simulations. ESR is a highly endothermic reaction which prefers high temperature, and the temperature control within the reactor is important (Sidhu et al. 2017). In this study (Gallucci et al. 2010), higher temperature is proved to be beneficial to the process intensification and leads to a higher ethanol conversion as membrane permeance is higher at higher temperature. As the driving force of membrane modules, higher

pressure is also preferred, as hydrogen flux through the membrane is higher under higher pressure. Furthermore, Murmura et al. (2015) studied ethanol steam reforming in a CMR with both experiment and a 1-D simulation. The three main reactions considered in the study were ethanol decomposition, water gas shift reaction and methane steam reforming reaction. Low steam to ethanol ratio is used in the study (S/E = 3), although higher steam to ethanol ratio is known to be beneficial for the process, by introducing a sweep gas on the permeate side, hydrogen partial pressure on the permeate side is lower, and the system was able to reach a complete ethanol conversion.

In addition, for membrane reactors, hydrogen carries part of the enthalpy across the membrane while permeating from the reaction side the permeate side of the reactor. Thus, as well as providing heat to this highly endothermic reaction, the heat source also has to compensate for the enthalpy that hydrogen carries away (Marigliano et al. 2001). In order to reduce the heat supply requirement, some studies proposed the idea of “heat-integrated” or “autothermal” reactor for both traditional packed bed reactors (Kolios et al. 2005) and membrane reactors (Chang et al. 2010). The idea is to combine both endothermic and exothermic reactions in the same unit in order to achieve a “homogenous reactor”. For packed bed reactors, two conjugate reactions are placed in parallel and separated by a wall (Murmura et al. 2016, Zanfir et al. 2011, Zhai et al. 2010), while for membrane reactors, two conjugate reactions are placed on each side of the membrane.

Table 2-2. Summary of previous experimental and simulation studies of ESR

Catalyst	T[K]	P [bar]	Steam to Ethanol ratio	Membrane surface area [$*10^{-4}$ m^2]	Ethanol Conversion [%]	H_2 Yield	Ref
$Pt/Ni\text{-}CeO_2$	613-753	6-10	3	17.6	100	0.3-4.8	(Tosti et al. 2008)
Co/Al_2O_3	673-873	1-8	1-11	-	95.3	-	(Murmura et al. 2015)
Ru/Al_2O_3	673-723	1.2-1.5	8.4-13	46.2	-	0.52-0.82	(Tosti et al. 2008)
$Pt_{0.5\%}/Al_2O_3$	623-723	1.1-2.0	8.4-13	46.2	-	0.2-0.6	(Papadias et al. 2010)
$NiO_{25\%}/SiO_2$	623-723	1.1-2.0	8.4-13	4.62	-	0.1-0.6	(Papadias et al. 2010)
$Rh/La\text{-}Al_2O_3$	873-1023	7-70	3-12	2.51	100	0.4-3.9	(Hedayati et al. 2016)
$Pd\text{-}Rh/CeO_2$	873-923	4-12	3.2-6	30.4	100	3.5	(Basile et al. 2011)
Co/Al_2O_3	673	3-8	3	24.2	100	-	(Mardilovich et al. 1998)

2.3 CFD simulation methods for membrane modules and membrane reactors

Simulation of membrane reactors is being widely used to study the phenomenon of concentration polarization in membrane reactors as well as to analyze the optimum operation conditions. The experimental study is able to analyze the quantitative parameters such as membrane permeance, reactant conversion, and product yield; however, it is not able to analyze the concentration profile visually, therefore it is almost impossible to analyze the concentration polarization effect through experimental method. However, numerical simulation of membrane reactors makes the concentration polarization phenomenon observable and further helps with understanding of the theoretical explanation behind the experimental result. In addition, numerical simulation can reduce the experiment number significantly, and provide constructive data for module scale up. Computational Fluid Dynamics (CFD) is an important method of numerical simulation.

The simulation of single tube membrane modules has been previously reported. For instance, Coroneo et al. (2009) developed a one-tube ceramic membrane model in a 3-D scheme with a fixed system temperature. A H_2 and nitrogen mixture was introduced to the system at retentate side and H_2 was depleted from the permeate side. The flux model was created using source and sink terms based on Sievert's law on each side of the membrane. Later, they developed a non-isothermal ceramic membrane 3-D model to evaluate the effect of temperature on permeance (Coroneo et al. 2009). In the model, a multicomponent feed was introduced to the system from the shell side, and pure H_2 was collected from tube side. Compared to the previous model, this model took the interaction between different gas components into consideration by defining the mass diffusion coefficient of each two components using Maxwell-Stefan formulation. Besides, the model not only considers inert species that have no influence on membrane permeance, it also considers the effect of CO, which has a poisoning effect on the Pd membrane. By introducing a correction term in the Arrhenius expression of membrane permeance, a promising simulation result is achieved. The correction of permeance term in Sieverts' law is expressed below:

$$Q_{Pd} = C(1 - \alpha(T)\frac{K_{CO}P_{ret}\emptyset_{CO,ret}}{1 + K_{CO}P_{ret}\emptyset_{CO,ret}})e^{-E/RT} \quad (2\text{-}21)$$

Where $\emptyset_{CO,ret}$ is the CO mole fraction on the retentate side, and K_{CO} and $\alpha(T)$ are experimentally-obtained parameters. A mesh with 734,000 cells was applied to the geometry, and at the boundary layer of each side of the membrane, a mesh refinement was implemented. Membrane was defined as a wall instead of a thin domain. To solve the Cartesian coordinate PDE set, a finite volume method was used through Fluent 6.3. The feed stream and retentate outlet stream was designed at the side of the reactor, and thus it is necessary to develop a 3-D model, since the behavior of the flow is not symmetric. It was found that the permeate flow rate increases when temperature increases. For system with pure H_2 as feed, temperature has a much more significant influence on the permeate flow rate compared with the system using binary composition feed. Mass transfer resistance consists of two parts: membrane resistance and concentration polarization, which does not apply for pure H_2. Thus, when temperature increases, membrane resistance decreases, however, temperature does not have any influence on the concentration polarization phenomenon. Since in binary system the main mass transfer resistance is concentration polarization instead of membrane resistance, temperature only has a minor influence on the permeate flow.

To further reduce the mass transfer resistance, recently, Coroneo et al. (2010) developed a model for the analysis of a 3-membrane module containing baffles. They showed that adding baffles divides the module in sections preventing the overall dilution of the retentate and increasing the driving force.

Applying the numerical method previously developed by Coroneo et al (2009), the same group developed a 3-D model for discussing the influence of baffles. Both a one tube lab scale system and a three tube pilot scale system have been simulated and verified by experiments.

Richardson et al. (2003) developed a numerical model using the finite element method for the study of concentration profile of a 2-D rectangular domain with a curved porous wall as one of

the boundaries. Continuity equation and Navier-Stokes equation need to be solved in the model. The boundary condition is defined by Fick's Law:

$$q_b = K(c_b - c_{out}) \tag{2-22}$$

Richardson utilized the method of decoupled algorithm, which means solve the flow equation and mass transfer equation separately. Using the up to date result as the initial value for next computation can reduce the calculating time as well as computer memory significantly. A convergence tolerance of 10^{-3} is used to determine the convergence. The method is proved to be precise for a maximum derivation of 0.6% from the standard error of 0.004%, which is determined by the difference between the inlet and outlet flow rate while no permeation boundary condition is set in the system.

Commercial packages that are often used include COMSOL Multiphysics, Fluent, OpenFOAM etc. Voller et al (2009) developed a two dimensional CFD model with COMSOL Multiphysics to simulate the process of water gas shift reaction and reforming reaction with membrane reactor. The heat, mass and momentum transfer is highly coupled in the simulation. Membrane permeance is function of temperature, and according to Sieverts' law, H_2 flux across the membrane is a function of membrane permeance and H_2 partial pressure difference between the permeate side and retentate side of the membrane reactor, which is directly related to the H_2 concentration. Reaction rate and equilibrium of WGS reaction and CH_4 steam reforming reaction is a function of temperature as well as the composition of the system. The heat generation from reaction is introduced as a heat source in the model, which depends on the reaction rate. In addition, gas density, which plays an important role in heat, mass, and momentum transport, is a function of temperature as well. The result was compared with a 1-D model from Matthias et al. (2009), and proved much more accurate, since the 1-D model used the assumption that both reactions reach equilibrium as soon as the reaction starts. However, although this assumption is valid for WGS reaction, CH_4 reforming reaction cannot reach thermodynamics equilibrium instantaneously.

Another 2-D simulation with COMSOL was carried out by Chen et al. (2012) with the geometry shown below, which coupled mass and momentum transfer and assumed the system isothermal.

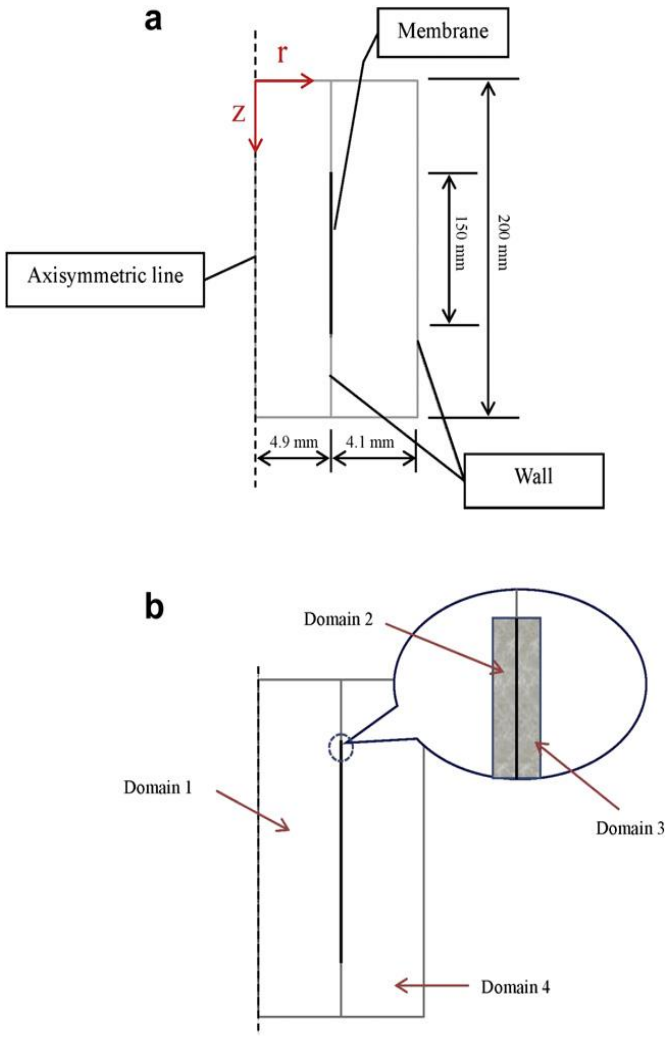

Fig 2.4 Schematics of (a) physical size of membrane tube and (b) computational domains

Gas mixture was introduced to the system. H_2 flux was represented by a sink and source term on each side of the membrane, and defined on domain 2&3, which has a thickness of 10μm. Parameters such as feed flow rate, flow pattern and sweep gas are being studied. Counter current flow pattern and adding sweep gas flow rate are proved to have a positive effect on diminishing concentration polarization. However, on the other hand, higher feed flow rate can

also reduce H_2 recovery, since more H_2 is flowing out of the system without being collected. In a later study from Chen et al. (2013), using the same numerical method, they proved the benefit of introducing baffles to the system for reducing concentration polarization phenomenon.

3. Development of a multi-tube membrane module for H_2 separation from syngas

-- Published as "Performance of a pilot-scale multitube membrane module under coal-derived syngas for hydrogen production and separation." Journal of Membrane Science 523 (2017): 515-523 3.1

3.1 Experimental study: Pilot scale multi-tube membrane module

3.1.1 Membrane Preparation and Module Design:

The Pd membranes developed at Worcester Polytechnic Institute (WPI) and previously reported in the literature were scaled up and replicated in order to synthesize eight new membranes. (Mardilovich et al. 2015; Ma et al. 2000; Ma et al. 2007; Ma et al. 2008; Chen 2010; Guazzone et al. 2013; Mardilovich et al. 1998). Eight porous stainless steel (PSS) tubes purchased from Mott Metallurgical Corp. were used for the synthesis of the membranes. Each porous tube had a surface area of 150 cm^2 and dimensions of 15 in. in length and 0.5 in. OD. Each porous support had a Media Grade of 0.5 µm and was welded to a capped end on one side and to a stainless steel tube on the other. All supports were cleaned in an ultrasonic bath utilizing propanol followed by an oxidation step at 600 ^oC for 12 hours in air. The pre-oxidized supports were subject to grading using two types of slurries composed of pre-activated alumina particles. The first grading step consisted of coarse particles with sizes in the range of 1-3 µm; while fine grading introduced particles of 0.6 µm. The grading layers were glued with palladium as previously described (Ma et al. 2007; Ma et al 2008). The membranes were then activated and electroless plated to create a dense Pd layer of the graded supports; for further reference on this procedure please refer to the pertinent literature (Ma et al. 2007, Ma et al. 2008). Afterwards, a gold layer was deposited on top of the palladium in order to improve the stability and recoverability of the membranes, as reported by Chen et al (2010). An additional layer of Pd was finally plated on top of Au to create a multilayered composite membrane. The thickness of the Pd and Au layers was estimated through gravimetric measurements and each step of the synthesis was characterized by a He leak test. Figure 3.1 shows the different thickness the seven membranes. On average the membranes had a thickness layer of 5.4 µm Pd, 0.4 µm Au and 1.6 µm Pd, with an intermediate grading layer of 2.5 µm. Notice that the replicability of

synthesizing these membranes is effectively demonstrated, having a standard deviation in the Pd layer thickness of 0.9 µm or about 10%.

Figure 3.2 shows the average He leak at each step of the synthesis. As purchased, each support had a He flux of 200 L/min at one bar ΔP and it was reduced to a cumulative (all seven membranes) He flux of < 0.01cm^3/min. The supports showed half the He flux after oxidation and further reduction to 56 cm^3/min after grading. Grading is a critical step in the formation of a defect-free Pd membrane since it reduces the uneven pore size distribution of the support and smooths its surface, allowing the formation of an even Pd thickness after plating (Ma et al. 2007; Ma et al. 2007). The total permeable surface area of the seven membranes is 1050 cm^2. The additional synthesized membrane was tested at WPI under controlled conditions with pure H_2 for comparison purposes. Moreover, it is important to mention that the membranes were synthesized layer-by-layer, creating well defined Pd and Au layers. Nonetheless, as shown in previous studies (Mardilovich et al. 2015; Chen et al. 2010), alloying occurs in-situ when the temperature is increased under the operating conditions considered in this work.

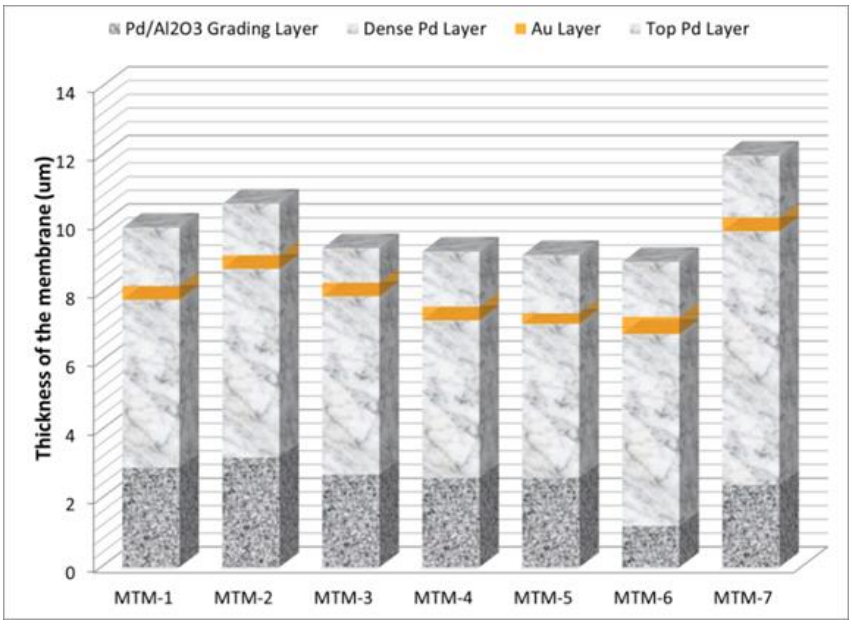

Fig 3.1 Composition of the multilayered composite membranes used in the present study.

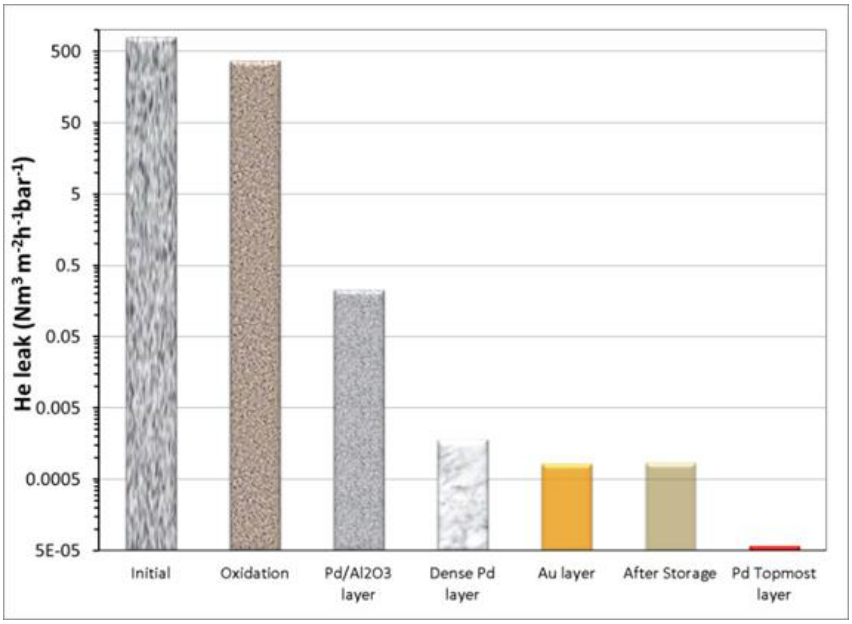

Fig 3.2 Average He leak through the Pd/Au/Pd membranes throughout each synthesis step.

The multi-tube membrane module was designed to hold seven Pd/Au/Pd membranes. The module had one membrane located at the center of the module and six equally spaced membranes surrounding it. The surrounding membranes were kept at 1.31 in. from the central membrane and were distributed in a hexagonal arrangement; the membrane module was designed to have a length of 38 in., as shown in Figure 3.3a. The axial positions of the membranes varied in order to allow Swagelok connections within the confinement of the 4.5 in. OD shell of the module. For instance, the connection of the central membrane was at a longer position than the surrounding ones; while the position of the remaining connections was alternated between shorter and medium lengths, as shown in Figure 3.3b. A holder was placed on the tip of the membranes to maintain the configuration of the membranes and potentially act as a baffle for better mixing of the gases. The multi-tube membrane module had a shell-and-tube configuration and was sealed utilizing an assembly consisting of flanges, studs and clamps (Grazyloc 4 in.) which can be seen in Figure 3.4.

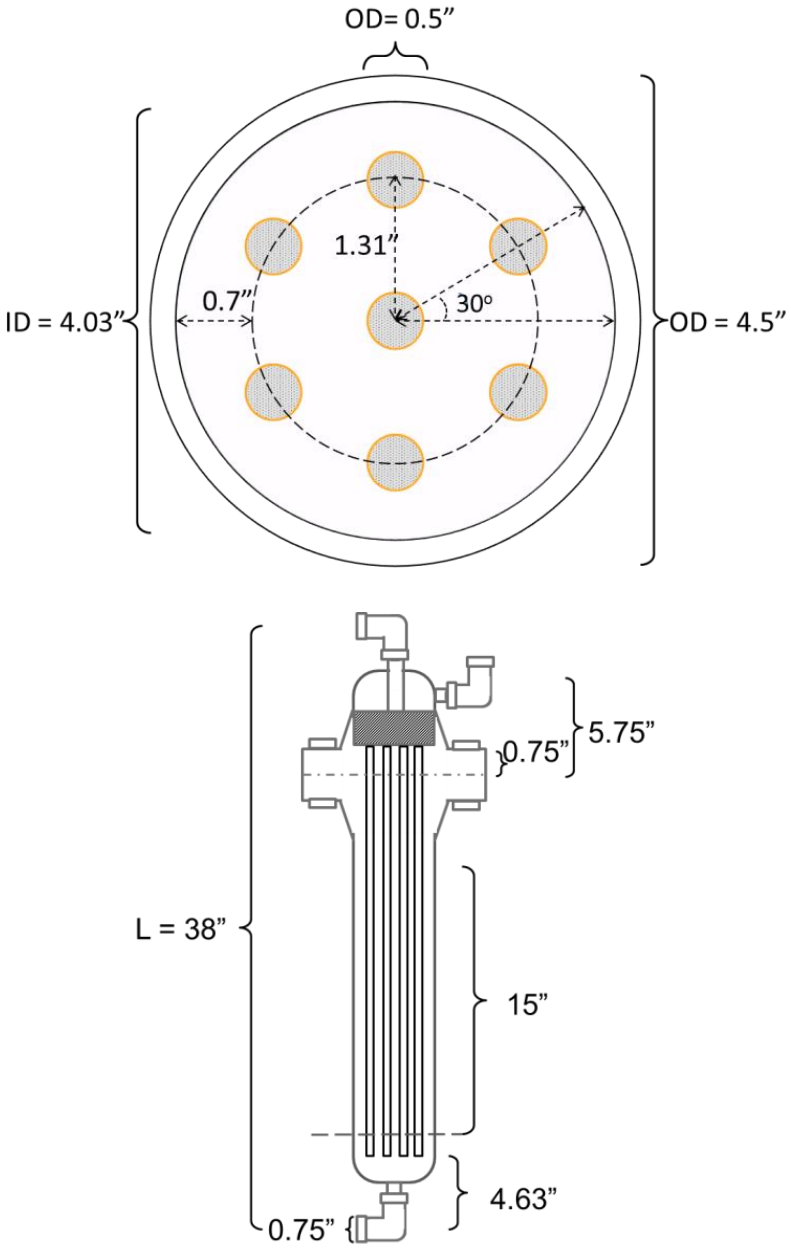

Fig 3.3 Schematic of the multi-tube membrane module design

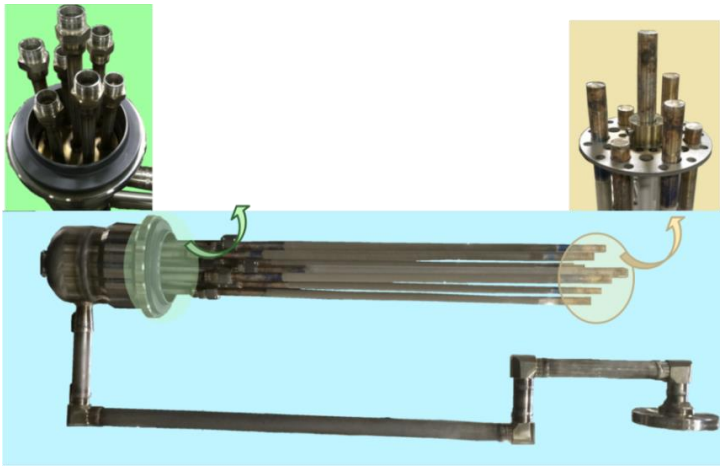

Fig 3.4 photograph depicting the membranes' arrangement.

3.1.2 Field Tests of the Multi-tube Membrane Module

The multi-tube membrane module containing seven Pd/Au/Pd membranes was installed in the WPI-MTR skid at the National Carbon Capture Center in Wilsonville, Al. (Guazzone et al. 2012) and it is shown in Figure 3.5. The module was purged with pure N_2 and its operating pressure was increased to > 12 bar and the temperature was increased to 450^{o}C. It is important to mention that the module showed no leak while testing the module seal. After reaching the operating temperature, a mixture of 35:65 H_2/N_2 was fed to the system, followed by the actual coal derived syngas.

Syngas was produced by an air blown transport integrated gasification (TRIG™) system that used powder river basin (PRB) coal. The raw syngas was treated to reduce particulates to 0.1 ppv, CO to < 1% and H_2S to < 1ppm, followed by H_2 enrichment of 30–40% to increase the H_2 partial pressure in the module and thus improve the driving force for permeation. The feed had an average composition of H_2: 43%, N_2: 50%, CO < 5%, CO_2: 1.5%, CH_4: 0.5% (mole fraction). The composition of the feed, permeate and retentate was monitored by a gas chromatograph (model Siemens Maxum II, columns: HysepN and HA-MS for H_2, N_2, CO, and CH_4; HysepN and HysepQ for CO_2 and H_2S; detector was a TCD), while the flow rates were measured periodically using a rotameter. Notice that the syngas at 160-180^{o}C was additionally heated through a pipe-

coil that surrounds the module as shown in Figure 3.5. For further information about the configuration of the rig and the gasifier, please refer to (Mardilovich et al. 2015; Guazzone et al. 2012; Guazzone et al. 2013).

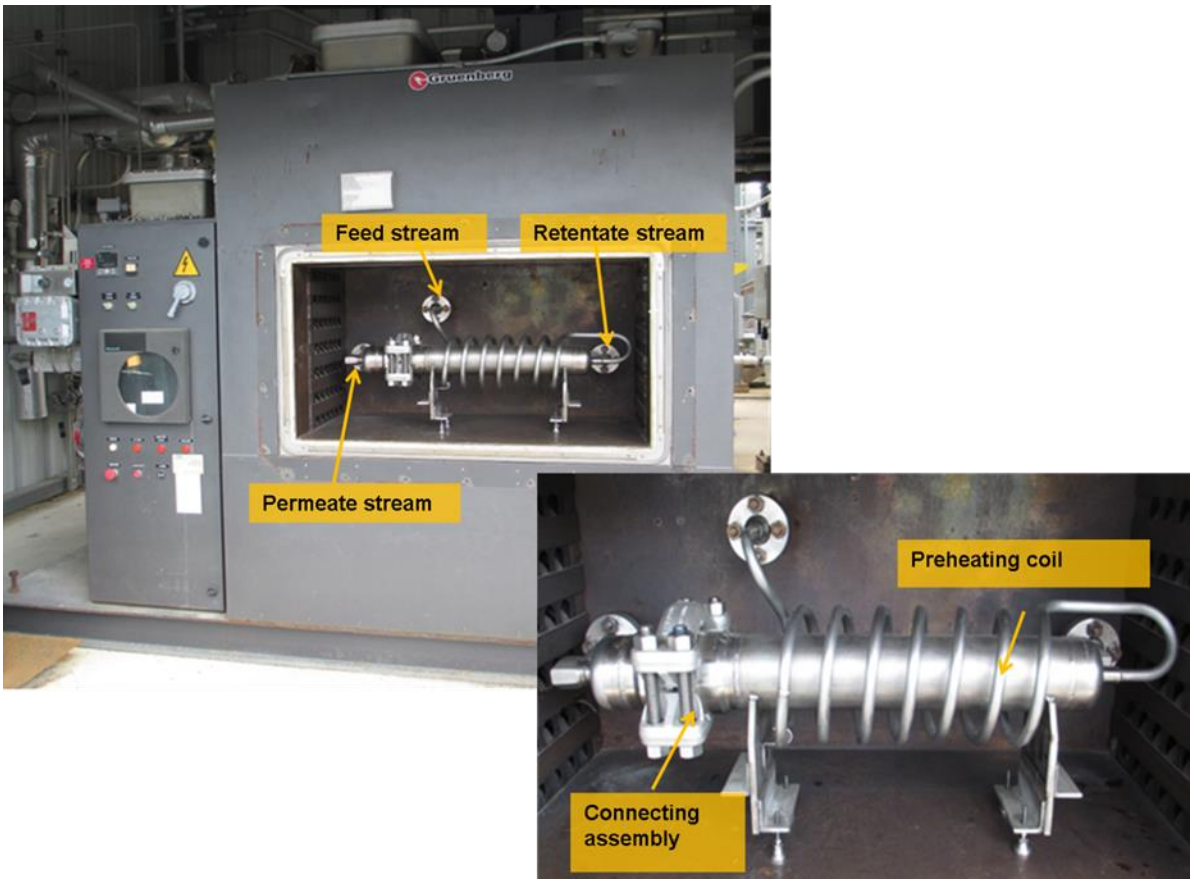

Fig 3.5 Photograph of the setup for testing the multi-tube membrane module at NCCC (Notice that the door of the oven was removed to facilitate display).

3.2 Test Results:

Approximately 10 lb/h of syngas with a variable composition was fed to the module as shown in Fig 3.7. The membranes were stored for 6 months at 40 ^{o}C under air after Au deposition. Figure 3.6 showed how the He leak changes after this period. For some of the membranes, He leakage increases while the others decrease. It is suspected that all the membranes have a higher leakage; the ones that present lower leakage are mainly the result from the moisture blocking the defects on the membranes surface. Due to the change in He leak, before the module was assembled with 7 of the 8 membrane tubes and send to NCCC, a topmost layer is formed on top of the membrane surface.

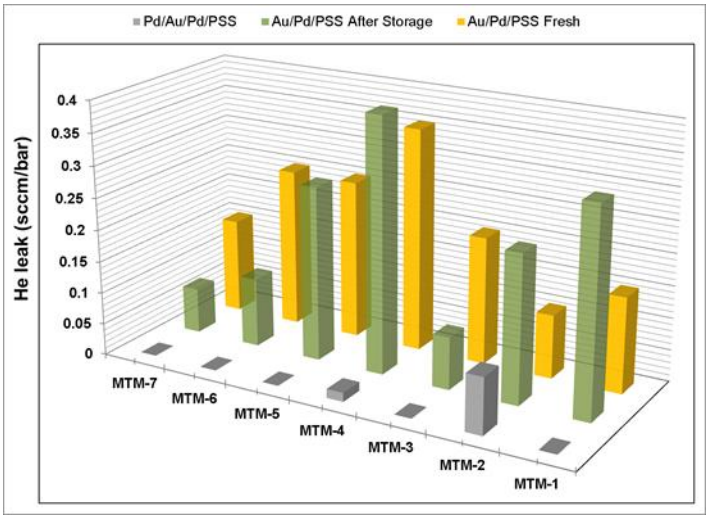

Fig 3.6 He leak of each membrane as fresh Pd/Au, after storage and final leak.

The initial evaluation of the performance of the membrane module was based on its H_2 permeance ($\overline{P}_{H2}$), produced H_2 purity and H_2 recovery (R) as defined in Equations 3-1 to 3-3.

$$\overline{P}_{H2} = \frac{F_{H2,perm}^{out}}{A\left(\sqrt{p_{H2}^{ave}} - \sqrt{p_{H2}^{perm}}\right)} \tag{3-1}$$

$$\text{Purity} = \frac{F_{H2,perm}^{out}}{\sum F_{i,perm}^{out}} \cdot 100 \tag{3-2}$$

$$R = \frac{F_{H2}^{in} - F_{H2}^{out}}{F_{H2}^{in}} \cdot 100 \quad (3\text{-}3)$$

Here $F_{H2,feed}$ and $F_{H2,perm}^{out}$ are the H_2 flow rates for the feed and the permeate outlet streams, respectively. A is the permeable surface area of the membranes, p_{H2}^{ave} and p_{H2}^{perm} are the H_2 partial pressures inside the module shell and in the permeate side, respectively. Given the number of data points, p_{H2}^{ave} was approximated as the average of the H_2 partial pressure of the feed ($p_{H2,feed}$) and the retentate ($p_{H2,ret}$).

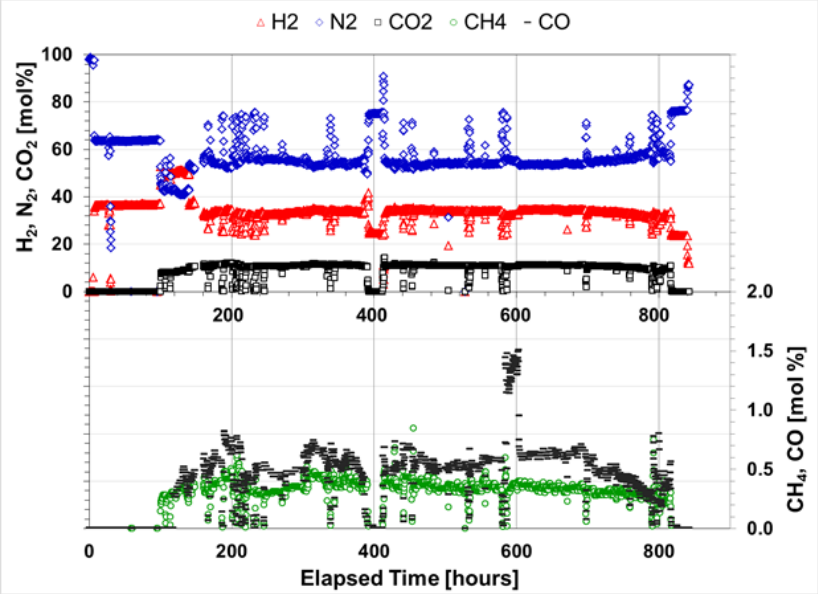

Fig 3.7 Composition of the gas mixture fed to the module as a function of time.

The H_2 permeance and purity of the module are displayed as a function of time as shown in Figure 3.8. At first, the membrane module showed a permeance in the range of 7-10 $Nm^3m^{-2}h^{-1}bar^{-0.5}$ when tested under H_2/N_2 mixture as depicted in Figure 3.8 in solid black data points. When syngas was fed into the module, a slight oscillation in permeance was observed during the first 100 h, followed by a steady performance. Notice that the average permeance under H_2/N_2 mixture and syngas were found to be of 8.8 and 8.2 $Nm^3m^{-2}h^{-1}bar^{-0.5}$, respectively indicating a 6% reduction in permeance under syngas conditions. The maximum flux achieved

by these membranes was 6 lb/day of H_2. It is important to mention that the module displayed constant properties (Figure 3.8) even though the continuous changes in the feed stream were present.

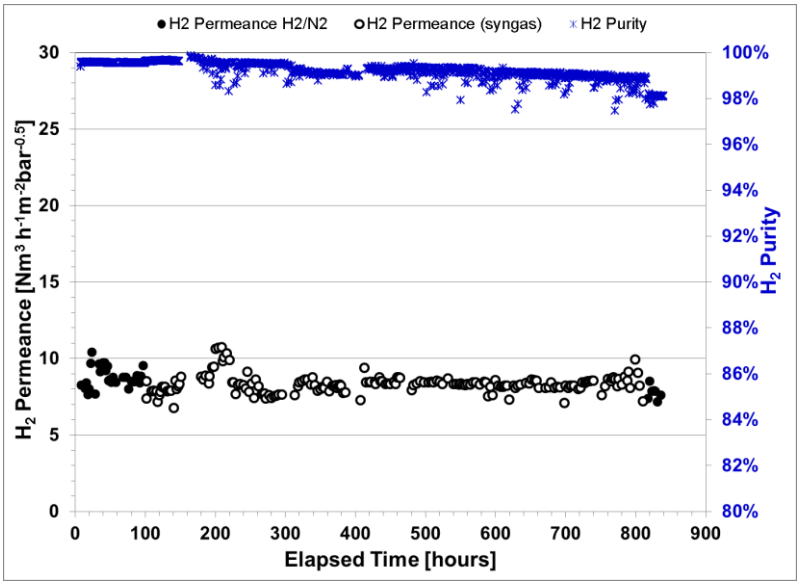

Fig 3.8 H_2 permeance and purity profiles of the multi-tube membrane module at NCCC.

The additional synthesized membrane tube (MTM-8) with the same dimensions and characteristics was tested at Worcester Polytechnic Institute under pure H_2. The H_2 permeance test at 350 and 450°C can be seen in Figure 3.9, which are 75 and 80 $Nm^3m^{-2}h^{-1}bar^{-0.5}$, respectively. In terms of flux the membrane showed a maximum productivity of 1.03 lb/day at a pressure difference of 0.35 bar. Moreover, a hypothetical multitube model composed of pure free-standing Pd membranes with a thickness of 7.4 µm, and tested under pure H_2 at 450°C was calculated to have a theoretical H_2 permeance of 63 $Nm^3m^{-2}h^{-1}bar^{-0.5}$. In addition, the single tube membranes previously tested under similar syngas conditions at NCCC, showed H_2 permeances between 5 - 15 $Nm^3m^{-2}h^{-1}bar^{-0.5}$ and under pure H_2 at WPI permeances between 10 - 29 $Nm^3m^{-2}h^{-1}bar^{-0.5}$. The reduction of the cumulative H_2 flux across this multitube membrane is attributed to i) the fast depletion of H_2 along the membrane module. ii) The mass transfer resistance caused by the boundary layer formed at the surface of the membrane. iii)

The permeance inhibition caused by CO, CO_2 and steam (Boon et al. 2015); and finally iv) the potential sulfur content on the feed lines of the system at NCCC as previously reported (Guazzone et al. 2013). At these operating conditions, the module presented a depletion of H_2 along the membrane module hindering the actual value of the permeance. For instance, the feed stream presented an average H_2 partial pressure of 4.3 bar and it was reduced to 2.5 bar at the retentate outlet or by a factor of about 1.7. This reduction in driving force is not linear, as assumed in the present estimation of the permeance shown in 3.8. Furthermore, radial mass transfer limitations cause concentration polarization which occurs when H_2 diffusion is slower than the permeation rate. Indeed, the presence of a H_2 depleted boundary layer can significantly reduce the displayed H_2 flux across the membranes (He et al. 1999).

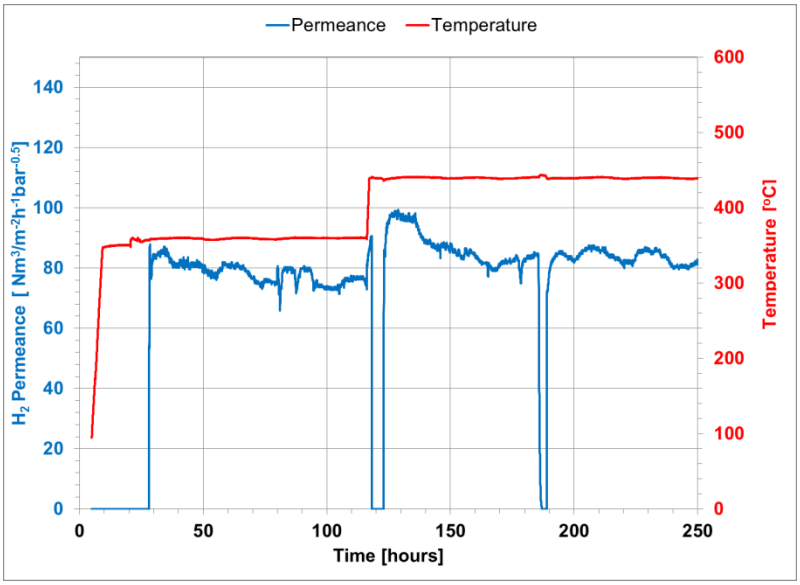

Fig 3.9. H_2 permeance of membrane MTM-8 at WPI.

A refined mathematical analysis was performed in order to approximate more accurately the permeance of this module. By neglecting the presence of uneven radial mass distribution and mass transfer resistances, but including the nonlinearity of the H_2 partial pressure within the module, the permeance of the membrane module was estimated by solving the differential equation shown in Eq. 3-4. F_{H2} is the local H_2 flow rate across the membrane module, *A* the total surface area, and p_{H2} is the local H_2 partial pressure, which is defined as the product of

the total operating pressure and the local H_2 mole fraction in the retentate (Eq. 3-5). The initial conditions of this ODE were specified as the given average experimental values such as feed gas composition and flow rate.

The permeance was adjusted accordingly in order to match the displayed H_2 recovery, retentate composition and total H_2 flow rate at the outlet of the permeate stream. For instance, the experimental permeance is 8 $Nm^3m^{-2}h^{-1}bar^{-0.5}$, and therefore a permeance vector ranging from <7-15> $Nm^3m^{-2}h^{-1}bar^{-0.5}$ is guessed. Each permeance value is used as input in the developed simulation model. The model is then evaluated based on the obtained H_2 flux on the permeate, the H_2 recovery and the molar fraction at the retentate. The output values are then compared to the experimental results in order to compute the error within the experimental estimation and a 1D model. The sum of all errors in the 3 parametric outputs are added and the minimum value is chosen as the real permeance as shown in Figure 3.11.

Figures 3.12 show the performance of the simulation model compared to the obtained experimental value for the 3 parametric outputs. Figure 3.12 a) shows the H_2 mole fraction at the outlet of the retentate matching the obtained experimental value of 0.22. Figure 3.12 b) shows that the H_2 permeate flux of the simulation is 15 L/min compared to the average experimental value of 17 L/min. The H_2 recovery displayed by the model was of 0.48 which is higher than the experimental value of 0.37. It is important to mention that experimentally, the results showed various outputs rather than a consistent single value; this is caused mainly due to the presence of systematic errors. Therefore the simulation model was compared with the experimental average values and the deviation in Figure 3.12 a-c) is valid.

$$\frac{dF_{H2}}{dA} = \overline{P}_{H2} \cdot \left(\sqrt{p_{H2}} - \sqrt{p_{H2}^{perm}} \right) \tag{3-4}$$

$$p_{H2} = p_{total} \frac{F_{H2,ret}}{\sum F_{i,ret}} \tag{3-5}$$

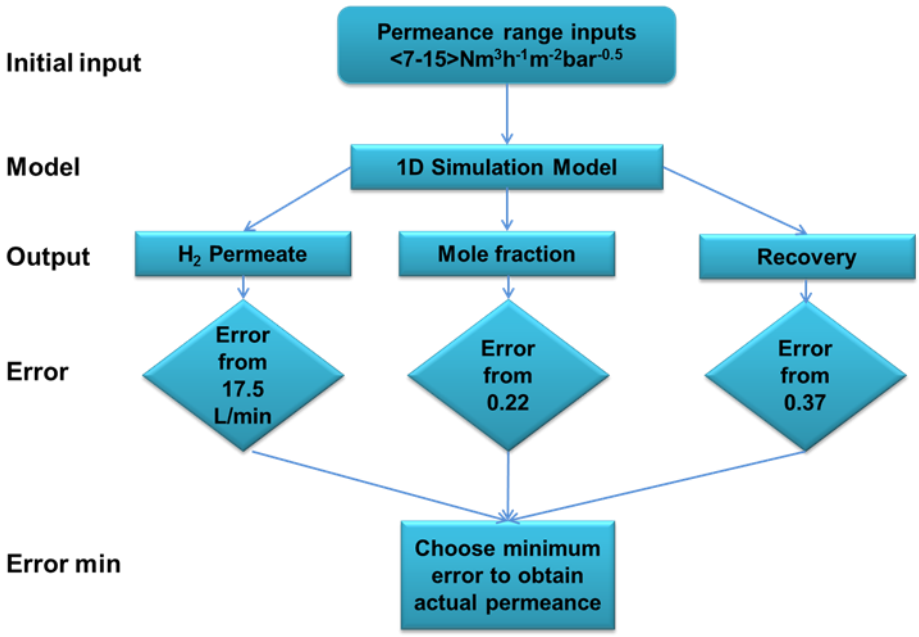

Fig 3.10. Flow diagram used to find the permeance of the actual permeance of the module

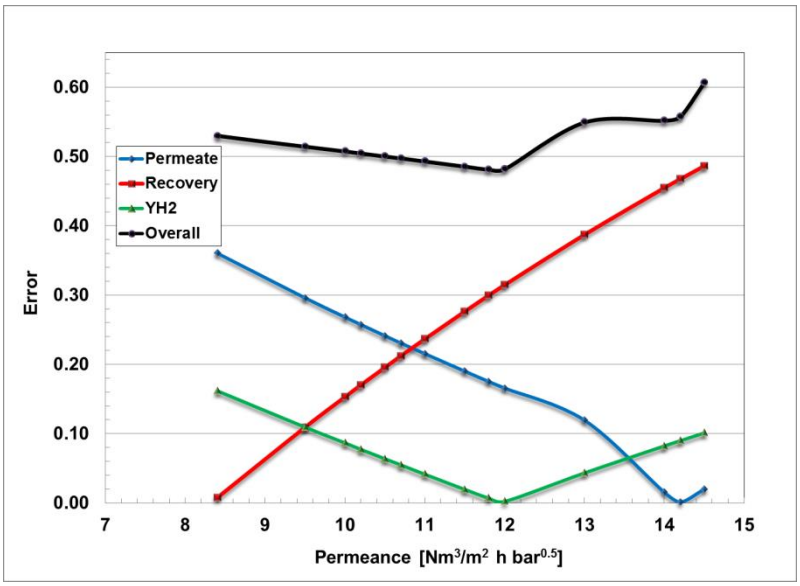

Fig 3.11 Computation of the errors in the permeate flux, recovery, mole fraction in the retentate under different permeance values.

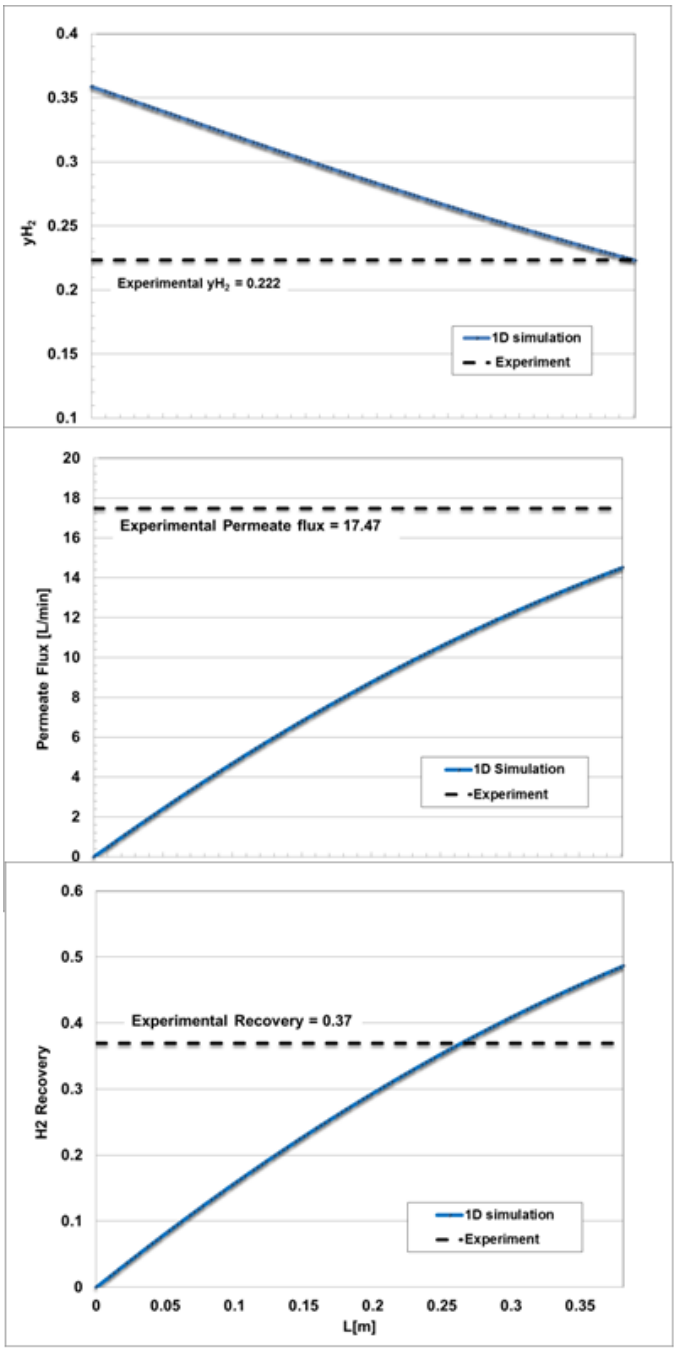

Fig 3.12 Performance of the CFD model at the optimized permeance for a) mole fraction at the retentate, b) the permeate flux and c) H_2 recovery

Notice that given the complexity of this calculation, the permeance estimate was shown only for the average properties rather than for every single point through time as the data shown in Figure 3.8. The H_2 permeance of the membrane module was estimated to be 16.2 $Nm^3m^{-2}h^-$

[1]$bar^{-0.5}$, which is considered to be a more accurate value than that obtained using Eq. 3.16, because p_{H2} on the retentate side was allowed to vary nonlinearly, as shown in Figure 3.13

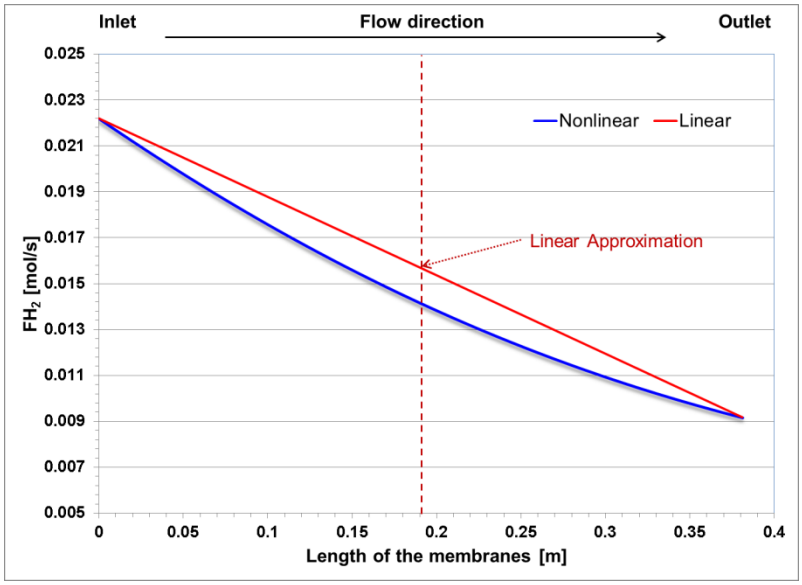

Fig 1.13 Axial distribution of the retentate H_2 flow rate, showing the difference between the linear and refined mathematical approximation

The presence of CO is well known to affect the permeance of Pd membranes (J. Boon 2015). Competitive absorption of CO within the active sites available reduces the potential solution of more H_2 molecules and consequently inhibits their performance under ideal conditions. It is important to mention that other contaminants present in syngas such as sulfur have been shown to reduce the permeance of Pd membranes. Mardilovich et al. (2015); Guazzone et al. (2013) showed in single tube Pd and Pd-Alloy membranes that even traces of sulfur can significantly reduce the H_2 permeance; nevertheless, the presence of the Au aids in the recovery of the lost permeance by exposing the membranes to pure H_2 at 450^{o}C. Other contaminants such as Na, Mg, O, S, Hg and C were previously found on the surface of the Pd membranes tested under coal derived syngas (Guazzone et al. 2013).

The H_2 purity produced by these membranes began at 99.5% under H_2/N_2 and underwent a sudden increase to 99.63% when syngas was fed and up to 99.87% after being tested for 67

hours in syngas conditions. Afterwards, the purity of the module decreased steadily reaching a minimum purity of 98.84% after 670 hours under syngas conditions. Notice that at the end of the test, the H_2 purity was of 98.13% under a H_2/N_2 mixture. It is important to mention that the lifetime of these membranes is significantly improved compared to pure Pd membranes, whose life time is estimated to be 200 h under industrial settings (Mardilovich et al. 2015; Ryi et al. 2014). Additionally, the single tube membrane tests previously reported (Mardilovich et al. 2015) showed Pd/Au composite membranes displaying H_2 purities in the range of 99.95-99.8% with a lifetime of 535 hours for a Pd/Au/Pt membrane. Furthermore, the H_2 purity profiles achieved by this technology throughout the testing time clearly outperform the ones exhibited by conventional technologies such as cryogenic distillation (Coroneo et al. 2009; Adhikari et al. 2006). Additionally, assuming that the purity of the permeated H_2 decreases linearly with time, as shown by Figure 3.8, it is expected that this module will produce H_2 with a purity of 91% after a year of continuous operation. Furthermore, once the defects of the membranes become significant, they can be regenerated by surface cleaning and Pd replating, reducing the leak of the membranes and extending their total lifetime (Ma et al. 2007).

H_2 recovery achieved under the aforementioned conditions as a function of time is shown in Figure 3.14. Notice that when the membrane module was under H_2/N_2 at the beginning of the test, the average recovery was estimated to be 52%. Under syngas conditions, the average H_2 recovery increased to 64%. This effect can be explained by analyzing the H_2 flow rate of the feed stream. As mentioned before, 10 lb/h of gas was fed into the module, but the different compositions between the H_2/N_2 mixture and syngas caused changes in the molar flow of H_2. For instance, 10 lb/h of gas feed is equivalent to 88 mol/h of H_2 fed for a (35/65) H_2/N_2 mixture, but it is 79 mol/h of H_2 fed for syngas enriched to 35%; there is a 10% difference in H_2 molar flow rate between the H_2/N_2 mixture and syngas. Furthermore, the space velocity of the gases is different for H_2/N_2 and for syngas. It is estimated that 5.5 m^3/h of H_2/N_2 was fed into the system at standard conditions, while syngas had a volumetric flow rate of 4.9 m^3/h.

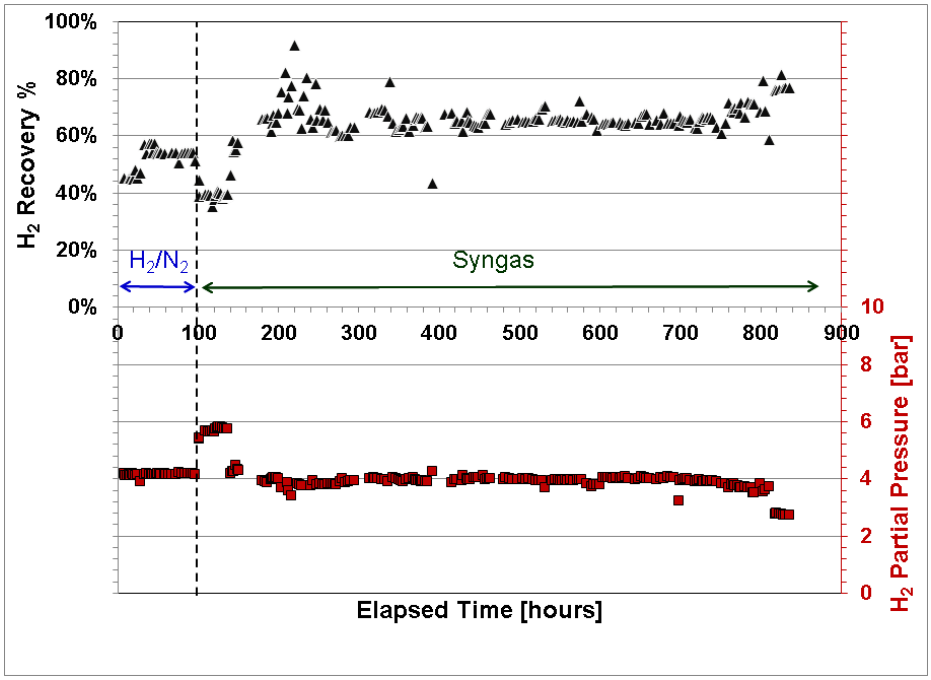

Fig 3.14. Hydrogen recovery and H_2 partial pressure of the multitube membrane module tested at NCCC.

Indeed, having a higher feed flow rate directly affects the recovery achieved (Fig 3.15) by the module since higher membrane surface area is needed to accomplish the transport of all H_2 molecules fed, even though the H_2 partial pressure is similar. Higher feed flow rate utilizes the available surface area of the membranes better, even though recovery is reduced. In other words, obtaining a low H_2 recovery directly implies that the membranes were occupied evenly and that the displayed permeance is closer to the permeance under pure H_2. High recoveries, such as those presented in this work, do not show the maximum H_2 flux that the module can achieve, since it is hindered by H_2 depletion within the unit. Fig 3.12 shows the module's H_2 recovery as a function of the H_2 feed flow rate. An exponential decay is observed and a plateau can be predicted at a recovery of ~40%.

Notice that the maximum theoretical H_2 recovery achievable by the module is < 90%, which can be improved by reducing the permeate H_2 partial pressure with the presence of sweep gas in the permeate side and/or by increasing the retentate pressure. Additionally, it is expected that

the presence of baffles could improve mixing and avoid mass transfer resistances, improving further the H_2 recovery of the module (Coroneo et al. 2009).

The successful results obtained from the 7-membrane module tests reported here demonstrate that the good performance previously found (Mardilovich et al. 2015; Guazzone et al. 2013) for a single membrane tube can be scaled up. These results are promising for the future development of palladium composite membrane modules with more tubes and hence greater permeation area.

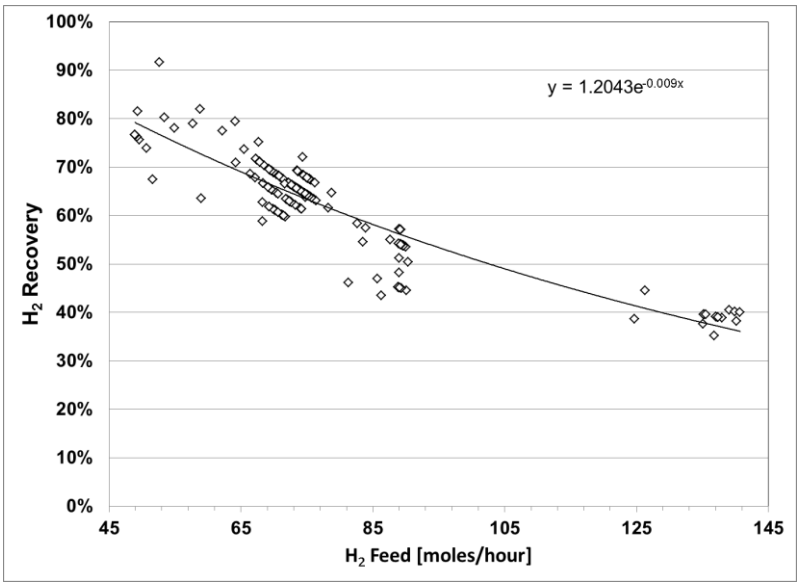

Fig 3.12. Hydrogen recovery as a function of the feed H_2 flow rate.

3.3 Computational methods:

3.3.1 Isothermal study of the multi-tube membrane module

CFD simulation analysis is a powerful tool for the study of mass transfer phenomena (Coroneo et al. 2009). Furthermore, simulation analysis provides important information for the module behavior under different operating conditions and different module configurations (Ma et al. 2017; Ma et al. 2016; Castro-Dominguez et al. 2016; Coroneo et al. 2009).

Representative sketch of the actual multi-tube membrane module with the demonstration of the flow direction is shown in Figure 3.16.

An impermeable tube cap is present at the tip for each membrane tube.

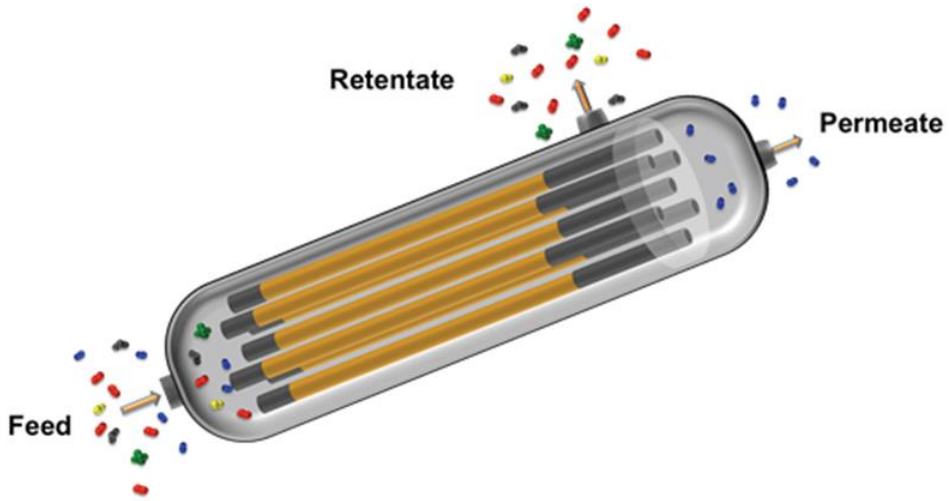

Fig 3.16 Representative sketch of the actual multi-tube membrane module

A nonporous tube is attached to the other side of the membranes. The feed stream is located in front of the membrane caps and its pipe diameter is smaller than the shell or module diameter as shown in Fig. 3.16. The permeated H_2 gas is collected from inside the membrane tubes. The gas that remained in the module, also called retentate, exits the module continuously containing H_2 depleted syngas. H_2 enriched syngas is fed at the shell side with a pressure of 12.6 bar. Pure H_2 is recovered at the tube side exposed to atmospheric pressure. Table 3-1 contains a list of the parameters used in this simulation. The model shows clearly the behavior of the system under different operation conditions.

Table 3-1. Operational settings for the module

Shell Pressure/atm	12.6
Tube Pressure/atm	1
H_2 Permeance / mol $m^{-2}s^{-1}Pa^{-0.5}$	8.2x10-4
Reynolds number	1-300
Initial gas composition /mole %	
H_2	34
N_2	55
CO	<1
CO_2	10
H_2O	~0

The geometry in Fig 3.16 was simplified by neglecting any physics occurring at end of the membranes as shown in Fig 3.17 and Fig 3.18 (geometry in Comsol). The inlet stream diameter was specified to be smaller than the module.

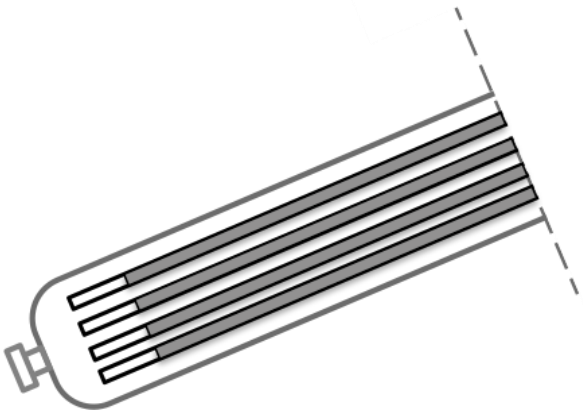

Fig 3.17 Simplified geometry of the multi-tube membrane module

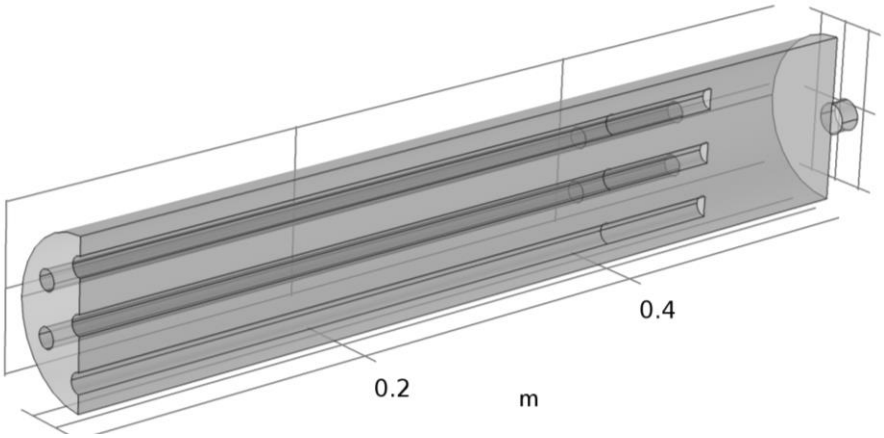

Fig 3.18 Simplified geometry of the multi-tube membrane module

The inlet was specified to be a normal inlet flow. The outlet had a pressure of 12.6 bar with no viscous stress. The species transport had the initial mole fractions shown in Table 3-1. A fine mesh was defined as shown in Fig 3.19 containing 3,181,368 degrees of freedom. A direct solver with two segregated groups was adopted for the calculation. A super computer with 130 GB RAM memory was used in this work. Only the shell side flow pattern was studied as no sweep gas was introduced to the tube side and the pressure was controlled at 101.3 kPa.

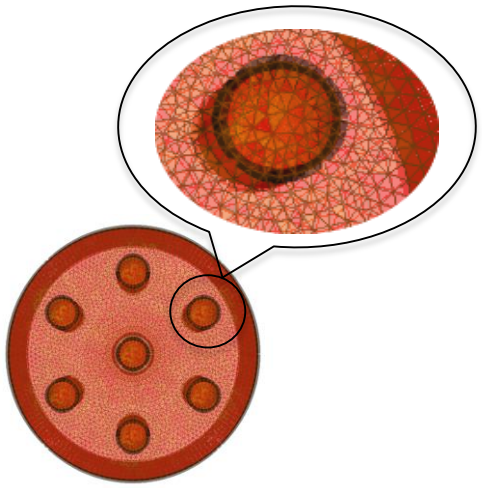

Fig 3.19 Cross-sectional view of developed mesh.

In order to study the tube-to-tube difference for H_2 removal rate, an asymmetrical model, which is much closer to the reality, was developed (Fig 3.20). The module shell has an inner diameter of 10.23 cm and a length of 96.52 cm excluding the inlet and outlets; the membrane tubes have an outer diameter of 1.27 cm and length of 38.1 cm. Each membrane tube has a surface area of 150 cm^2. The distance between the center tube and each outer layer tube is 3.33 cm. The operating conditions in the simulation were the same as in the NCCC testing rig. Compared with the simplified geometry, the new geometry includes the second half of the membrane support, the manifold that collects H_2 from the seven tubes, and both retentate outlet and permeate outlet.

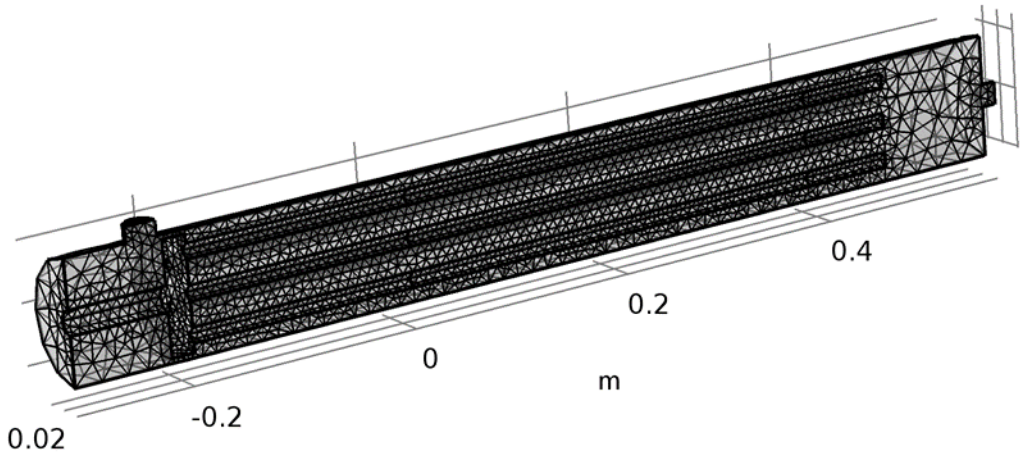

Fig 3.20 Asymmetrical geometry of the membrane module

The geometry mesh has 505218 elements with 4776265 degrees of freedom; mesh is refined at the membrane boundaries and the shell side inlet and outlet, while the module bulk volume has a coarser mesh in order to save computation time. The simulation result reached mesh independence at current mesh quality. A segregated solver with two segregated groups are used for the simulation.

Assumptions of the simulation model include:

1) The system operates under laminar flow conditions.
2) Membrane has infinite selectivity and H_2 is the only species permeating through the membrane.

3) The system is isothermal, temperature has a homogenous distribution inside the module. Also since membrane permeance is a temperature-related property, all the membrane tubes are assumed to have the same permeability regardless of the position inside the module.

The Navier-Stokes equations and the mass balance equation were coupled and solved using Comsol Multiphysics 5.3:

$$\rho\nabla(u) = 0 \tag{3-6}$$

$$\rho(u \cdot \nabla)u = \nabla \cdot [-pI + \mu(\nabla u + (\nabla u)^{T})] + F \tag{3-7}$$

$$\nabla \cdot j_i + \rho(u \cdot \nabla)\omega_i = R_i \tag{3-8}$$

In which μ is the viscosity of the mixture:

$$\mu = \sum_{i=1}^{N} \frac{x_i \mu_i}{\sum_{j=1}^{n} x_j \phi_{ij}} \tag{3-9}$$

ϕ_{ij} is the binary factor:

$$\phi_{ij} = \frac{1}{2\sqrt{2}}(1 + \frac{M_i}{M_j})^{-0.5}\left[1 + \left(\frac{\mu_i}{\mu_j}\right)^{0.5}\left(\frac{M_j}{M_i}\right)^{0.25}\right]^2 \tag{3-10}$$

ω_i is the mass fraction of each species, ρ is the density of the gas mixture, which is computed by ideal gas law:

$$\rho = \frac{pM_n}{RT} \tag{3-11}$$

In which M_n is the gas mixture molar mass:

$$M_n = \left(\sum_i \frac{\omega_i}{M_i}\right)^{-1} \tag{3-12}$$

Fick's law is used to describe the diffusion of each species:

$$j_i = -(\rho D_i \nabla \omega_i + \rho \omega_i D_i \frac{\nabla M_n}{M_n}) \quad (3\text{-}13)$$

In which the diffusion coefficient is calculated by:

$$D_i = \frac{1 - \omega_i}{\sum_{k \neq i} \frac{x_k}{D_{ik}}} \quad (3\text{-}14)$$

At the membrane boundary, the H_2 flux is governed by Sieverts' Law:

$$-n \cdot N_{H_2} = \overline{P}_{H_2} \left[\sqrt{p_{H_2}^{shell}} - \sqrt{p_{H_2}^{tube}} \right] \quad (3\text{-}15)$$

In which $\overline{P}_{H_2}$ is the H_2 permeance of the membrane, and $p_{H_2}^{shell}$ and $p_{H_2}^{tube}$ are the H_2 partial pressure on shell and tube side, respectively. Hydrogen permeance used in the model is from the NCCC test, which is 8.2 $Nm^3m^{-2}h^{-1}bar^{-0.5}$ under actual coal-derived syngas.

Additionally, the H_2 recovery was analyzed and defined as the percentage extracted from the module through the tubes:

$$R_{H_2}(\%) = \frac{F_{H_2}^{in} - F_{H_2}^{out}}{F_{H_2}^{in}} \cdot 100 \quad (3\text{-}16)$$

Where $F_{H_2}^{out}$ and $F_{H_2}^{in}$ are the amount of H_2 at the outlet and the feed of the module, respectively. The usage of the membrane $\varphi(\%)$ was studied as well and defined as:

$$\varphi(\%) = \frac{\gamma}{\gamma_{max}} \cdot 100 \quad (3\text{-}17)$$

Where γ is the amount of H_2 removed at any given Re, and γ_{max} the maximum theoretical H_2 flux across the membrane.

In order to measure the influence of the concentration polarization on the membrane module performance, Mori et al (2007) carried out an experimental study. By demonstrating the influence of different operating conditions on H_2 production rate, the effect of the reactor configuration on the concentration polarization was analyzed. However, for the reason that concentration polarization may not be the only aspect that influences the H_2 production, a more direct and quantitative method to demonstrate the concentration polarization effect is desired. The concentration polarization coefficient (CPC) is usually used to define the difference between the ideal permeation driving force to the driving force in reality (Caravella et al. 2009). It is difficult to measure this effect experimentally, thus, a simulation method is necessary.

$$\begin{aligned} \mathrm{CPC} &= 1 - \frac{[\text{Driving Force}]_{\text{Mem}-\text{Mem}}}{[\text{Driving Force}]_{\text{Bulk}-\text{Bulk}}} = 1 - \frac{\text{Actual H2 flux}}{Q_{H_2} \cdot \Delta\sqrt{P_{H_2}}|\text{bulk}} \\ &= 1 - \frac{\Delta\sqrt{P_{H_2}}\big|^{\text{Membrane}}}{\Delta\sqrt{P_{H_2}}\big|^{\text{Bulk}}} \end{aligned} \tag{3-18}$$

In which P_{H_2} is the H_2 partial pressure at the retentate.

Instead of the CPC profile along the entire membrane length, the average CPC (CPC_{avg}) (Ahmad et al. 2005) defined in Eq. 3-19 is more often used to indicate the concentration polarization effect of the entire membrane module.

$$\mathrm{CPC}_{\mathrm{avg}} = \frac{1}{L}\int_0^L \mathrm{CPC}(z)\,dz \tag{3-19}$$

Membrane modules have the highest CPC value towards the end of the module; however, as the H_2 flux is smaller at this area, the contribution of this area to $\mathrm{CPC}_{\mathrm{avg}}$ is less significant. The above expression equally considered each area's contribution to the overall concentration polarization effect, thus it overestimated the polarization effect in the module. Caravella et al (2016) introduced the Effective Average CPC (EAC) with the expression below, which is a more accurate way to measure the average polarization effect.

$$\mathrm{EAC} = 1 - \frac{\text{Permeation rate with polarization}}{\text{permeation rate without polarization}}$$

$$= 1 - \frac{\int_0^{\mathrm{L}} \mathrm{Flux(z)dz}}{\int_0^{\mathrm{L}} \frac{\mathrm{Flux(z)}}{1 - \mathrm{CPC(z)}}\,\mathrm{dz}} \tag{3-20}$$

$$= \frac{\text{Actual H2 permeation rate}}{\iint_{\mathrm{S}} \mathrm{Q_{H_2}} \cdot \Delta\sqrt{\mathrm{P_{H_2}}}\big|\mathrm{bulk}\,\mathrm{dA}}$$

Geometries with one and two baffles were developed referencing the geometry of a shell and tube heat exchanger (Fig 3.21). Single segmental baffles were added to the module, aiming to create more recirculation that can reportedly decrease the boundary layer thickness and thus reduce the concentration polarization effect. Baffle thickness was designed to be 0.254 cm; with a 37.5% horizontal baffle cut in order to avoid the formation of eddies. For the two-baffle model, the two baffles divided the membrane length into three equal-length sections which makes the space between the two baffles to be 0.127 m. The same governing equations were solved using previous described method.

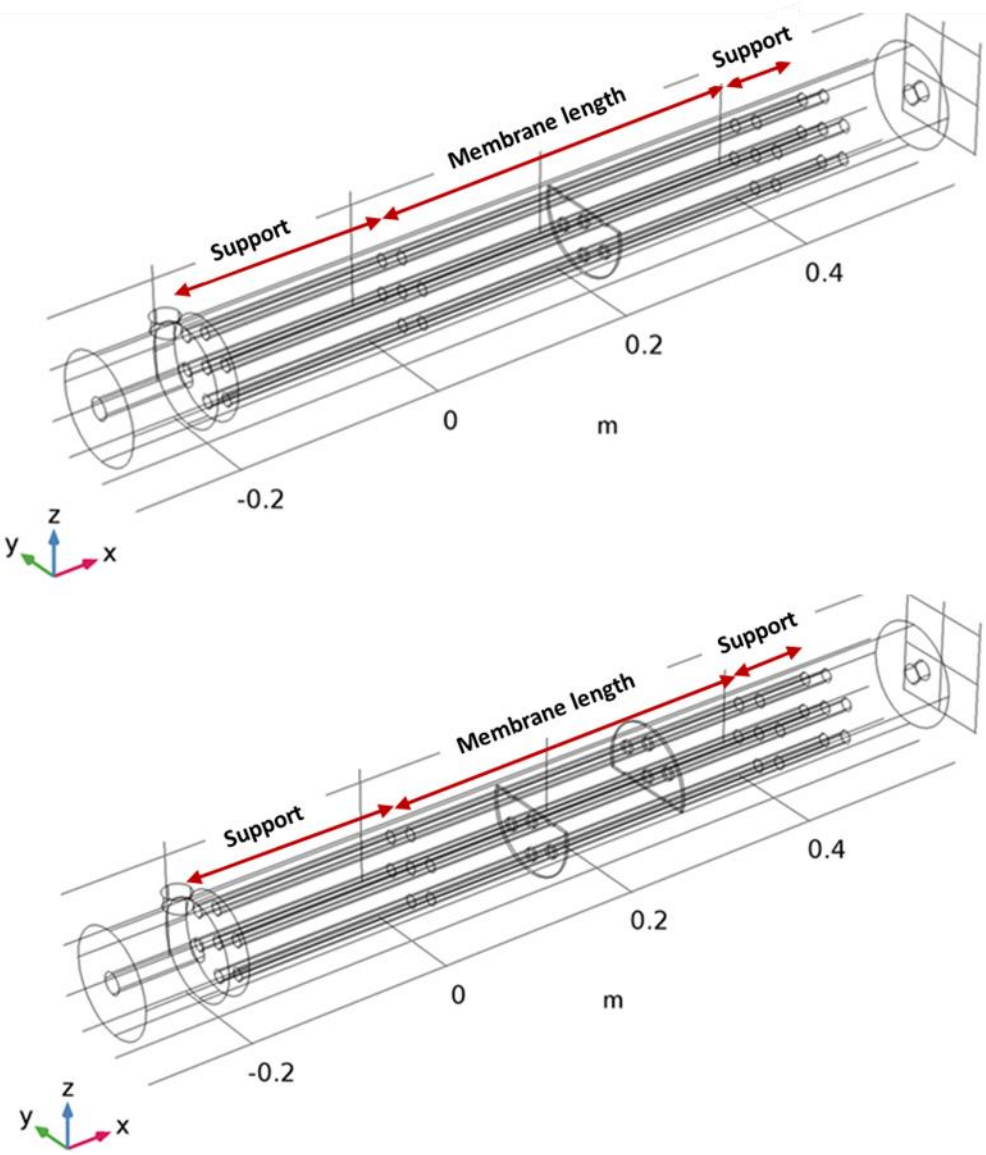

Fig 3.21 Module configuration with baffles

Given the amount of syngas produced by coal combustion, studies of larger scale modules are desired in the industry. In order to increase the module capacity and provide technical data for commercialization, a larger scale module with 2850 cm^2 membrane surface area was studied. Higher membrane surface area is achieved by adding one more layer of membrane tubes in the shell (Fig 3.22), each membrane tube has the same dimension as described before. The module shell now has an inner diameter of 16.90 cm, while the module length is kept the same. Compared with increasing the length of the membrane tubes in order to increase the

membrane surface area, adding more tubes can achieve the same goal while maintaining a high membrane surface to module volume ratio, which is economically preferred. When scaling up the module through adding more membrane tubes, the performance of the extra tubes are of special interest as it is economically desirable for the outer layer tubes to have similar H_2 flux rate compared to the tubes at the center. Thus, H_2 flux through each membrane tube and mass transfer limitations were studied for the scaled up module. The simulation method, temperature and pressure used in the simulation are the same as previously for the 7-tube case, while different flow rates were studied.

Fig 3.22 Further scaled-up geometry of the membrane module

3.3.2 Non-isothermal model

To study the temperature distribution of the module, heat transfer property was added to the model to further simulate a non-isothermal system. Simplified geometry is used in this case. In isothermal model discussed above, it was assumed that inlet feed temperature is the same as shell temperature. However, in reality, due to the limitation of pre-heat length, feed temperature is always lower than what we expect. This caused a temperature distribution along the reactor. As previously studied by Mardilovich et al. (1998), H_2 flux is positively

influenced by temperature as shown in Figure 3.23 after high temperature treatment for 5hours. Notice that in the study, temperature higher than 500°C was not taken into consideration, this is because at higher temperature, intermetallic diffusion takes place in the membrane and H_2 permeation is restrained.

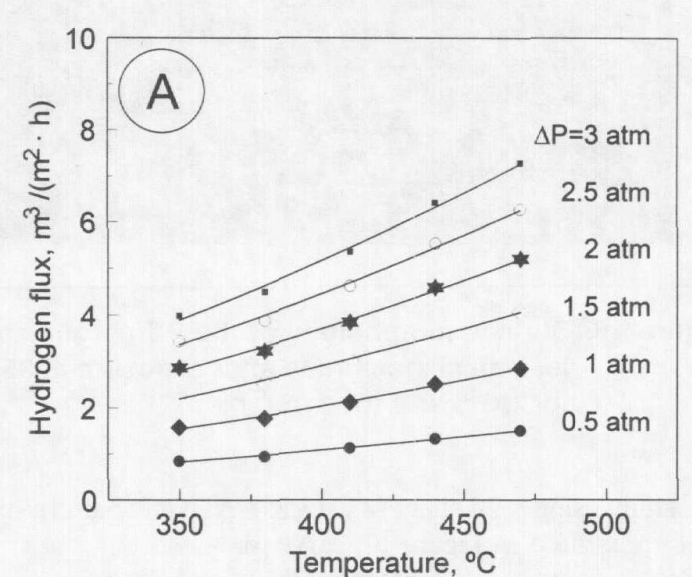

Fig 3.23 Influence of temperature on H_2 flux under different ΔP (Mardilovich et al. 1998)

Furthermore, membrane permeability Q is influenced by temperature by the expression 3-21 presented by Koc et.al (R. Koc 2014):

$$\mathrm{Q} = \mathrm{Q_0 e^{-E_p/(R\cdot T)}} = 6322.7\mathrm{e}^{(-\frac{15630}{\mathrm{R\cdot T}})} \qquad (3\text{-}21)$$

Where $\mathrm{E_p}$ is activation energy [J], $\mathrm{Q_0}$ is permeability constant $[\mathrm{m^3 \mu m/(m^2 h atm^{0.5})}]$.

Thus, it is important to include the energy transport to the previous isothermal model.

In COMSOL Multiphysics 5.0, physics “Non-isothermal Flow” and “Transport of Diluted Species” are used to develop the non-isothermal model. A same geometry is used as shown below.

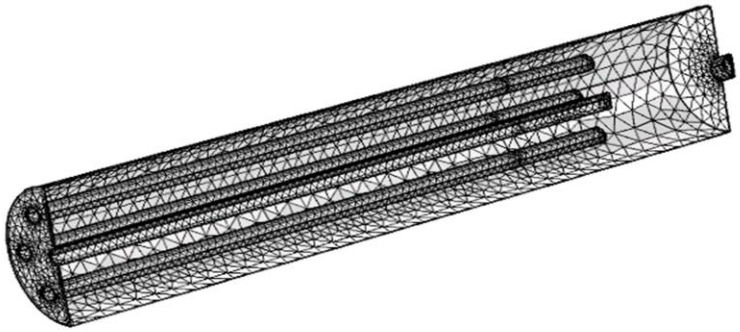

Fig 3.24 Geometry of the model and mesh

Equation of motion and continuity equation is used in this model as well, but differently, continuity equation was expressed on a mole concentration base instead of mass fraction as shown in Eq3-22

$$\nabla \cdot (-D_i \nabla c_i) + u \cdot \nabla c_i = R_i \tag{3-22}$$

Besides, in physics "Non-isothermal Flow" conservation of energy is introduced as:

$$\rho C_p u \cdot \nabla T = \nabla \cdot (k \nabla T) + Q \tag{3-23}$$

Considering the effect of temperature to membrane permeance, Sievert's law now has the expression of:

$$J_{H_2} = \frac{Q_0}{\delta} \exp\left(\frac{-E_Q}{RT}\right)\left(P_{H_{2,ret}}^{0.5} - P_{H_{2,per}}^{0.5}\right) \tag{3-24}$$

"Normal" mesh was applied to the model, with 1,980,170 degrees of freedom.

3.4 Simulation Results Analysis:

3.4.1 Symmetrical isothermal model:

Through a computation fluid dynamics (CFD) model, a compelling visualization of the mass transport phenomena occurring inside the membrane module was generated. The CFD model generated data at different permeances, predicting the performance of the actual system as shown in Table 3-2. Key parameters (permeation rate, H_2 content at the retentate and recovery) were most accurately projected by the model, assuming a permeance of 16 $Nm^3h^{-1}m^{-2}bar^{-0.5}$; it is important to highlight that this value is close to the 16.2 obtained earlier. The results presented in this work have an error of 2%, which could be further reduced by refining further the numerical mesh, as depicted in Fig 3.25. Certainly, although Fig does not show mesh-independent; given the purpose of this discussion and the lack of computational power, the analysis of the results with this accuracy is certainly justified.

Table 3-2: Comparison of CFD data with experimental data.

	Experimental	Simulation Permeance=14 $Nm^3h^{-1}m^{-2}bar^{-0.5}$	Simulation Permeance=16 $Nm^3h^{-1}m^{-2}bar^{-0.5}$	Simulation Permeance=18 $Nm^3h^{-1}m^{-2}bar^{-0.5}$
Permeate flow rate (L/min)	17.47	17.77	18.99	20.04
Retentate H_2 Percentage (%)	22.35	23.30	22.34	21.50
Recovery (%)	37	35.37	38.06	40.39

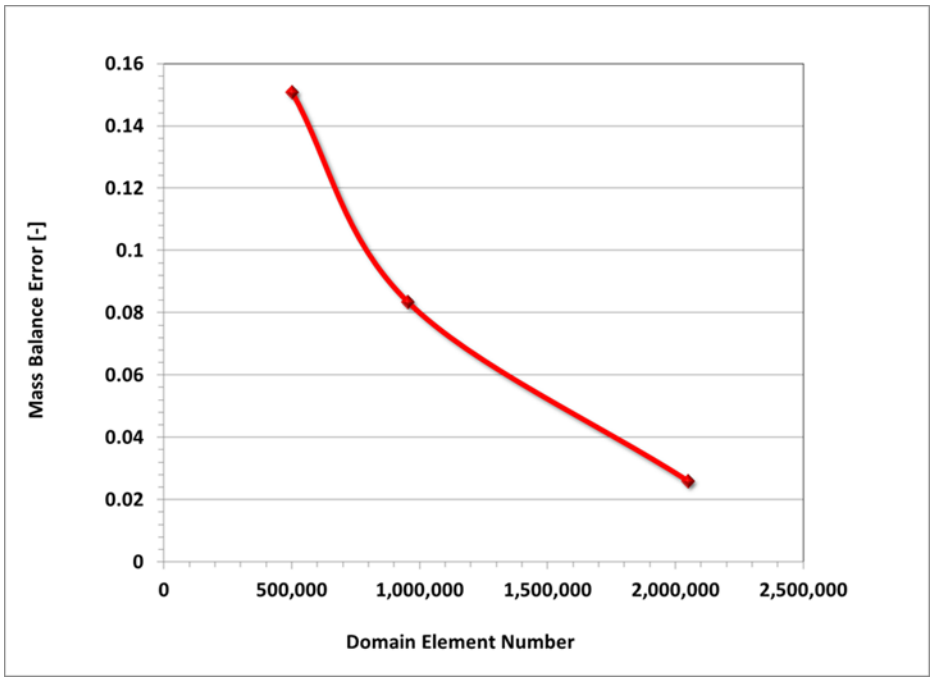

Fig 3.25 Mass balance error at different mesh refinements.

The CFD model generated representative H_2 concentration profiles inside the multitube membrane model as shown in Fig 3.26. Syngas is fed on the right side of the picture and exits the multitube module on the left side of the picture. The axial H_2 concentration profile (Fig 3.26 a) shows syngas with a high H_2 concentration on at the entrance (red) which gradually reduces when approaching the exit of the module. The radial H_2 concentration profile (Fig 3.26 b) changed axially. For instance, close to the syngas feed side, an even radial H_2 distribution is depicted (red); nonetheless, downstream, radial distribution gradients become more apparent. In particular, a H_2 depleted region (blue) adjacent to the membrane surfaces is clearly observed, while an increased H_2 concentration appears between the membrane tubes. These radial concentration differences cause the aforementioned concentration polarization effect.

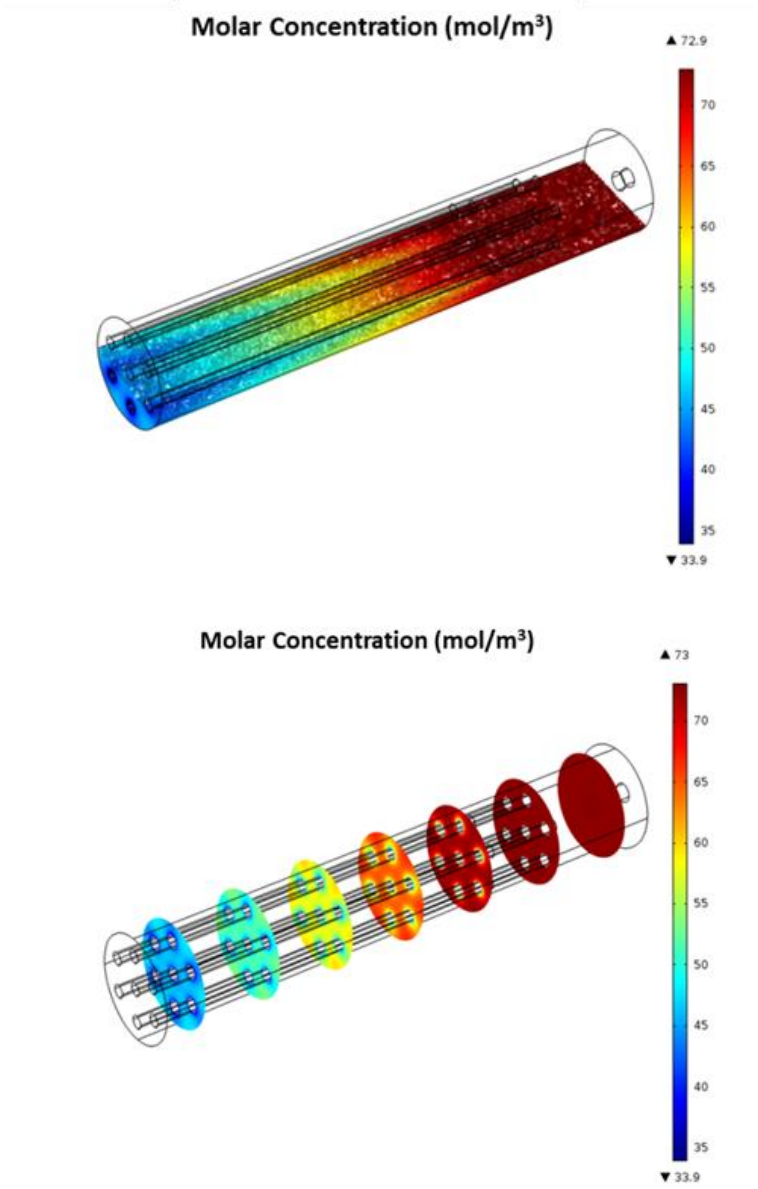

Fig 3.26 a) Axial and b) radial H_2 concentration profile inside the retentate of the multitube membrane module.

Based on the visualization presented in Fig 3.26, it is possible to infer that multitube membrane systems differ with single tube systems in two main aspects: i) multitube modules have higher membrane surface area to volume ratio and ii) not all membranes operate evenly. High surface area to volume ratio is beneficial in terms of productivity, as these architectures can generate higher amounts of H_2 than single tube modules, notably shown in hollow fiber membrane units

(Ismail et al. 2015). Nonetheless, increasing the membrane surface area in a constraint volume raises issues of cleaning, design and operation.

The behavior of the module was tested under different Reynolds numbers since advection forces affect the mass transport properties of the system. Different inlet velocities were used to modify the Re of the fluid flow. The velocity profiles, shown in Fig 3.27, depict that the velocity of the gas decreases after the expansion between the inlet and the membrane module. Velocity increases when the gases encounter the membranes; this is due to the reduction of available cross-sectional area.

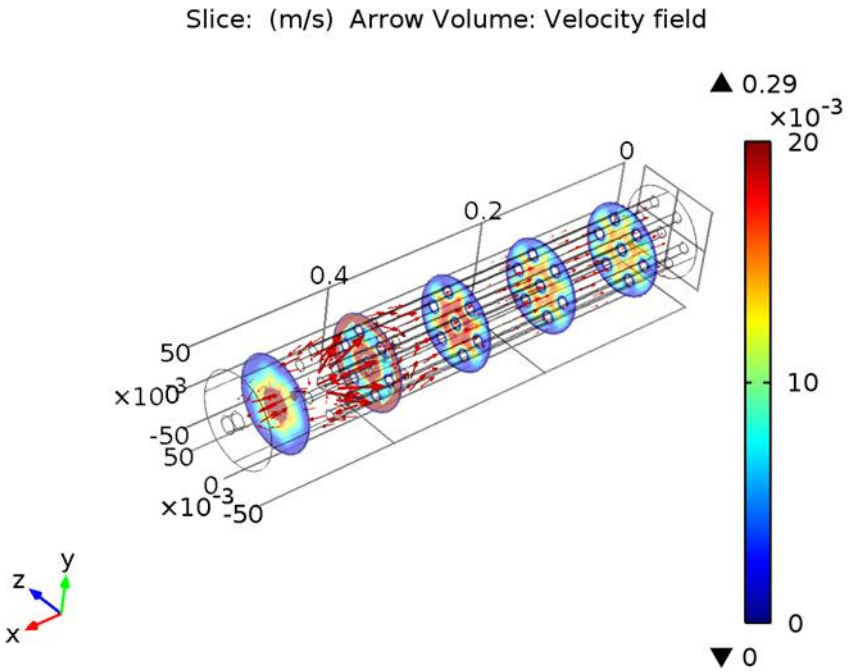

Fig 3.27 Velocity profile of syngas inside the membrane module at moderate Re numbers.

As shown in Fig 3.28 and Fig 3.29, different Re numbers displayed different H_2 mole fraction profiles within the membrane module. For instance, at low Re numbers, H_2 is totally removed from the module (Fig 3.28a). H_2 has enough time to diffuse radially towards the surface of the membranes, before it is ejected out of the module. The H_2 recovery at this point is at its maximum point, but the membrane usage capacity is not exploited.

As the Re numbers increase, H_2 molecules do not reach the surface of the membranes as fast as before. This allows for the membranes to be used further down axially (Fig 3.28 b). This continues up to the point where H_2 is unable to diffuse totally towards the adjacent membrane. At this point recovery starts to decrease. High Re numbers supply enough syngas, allowing the membrane to be more uniformly used axially (Fig 3.19c). However, recovery is significantly reduced.

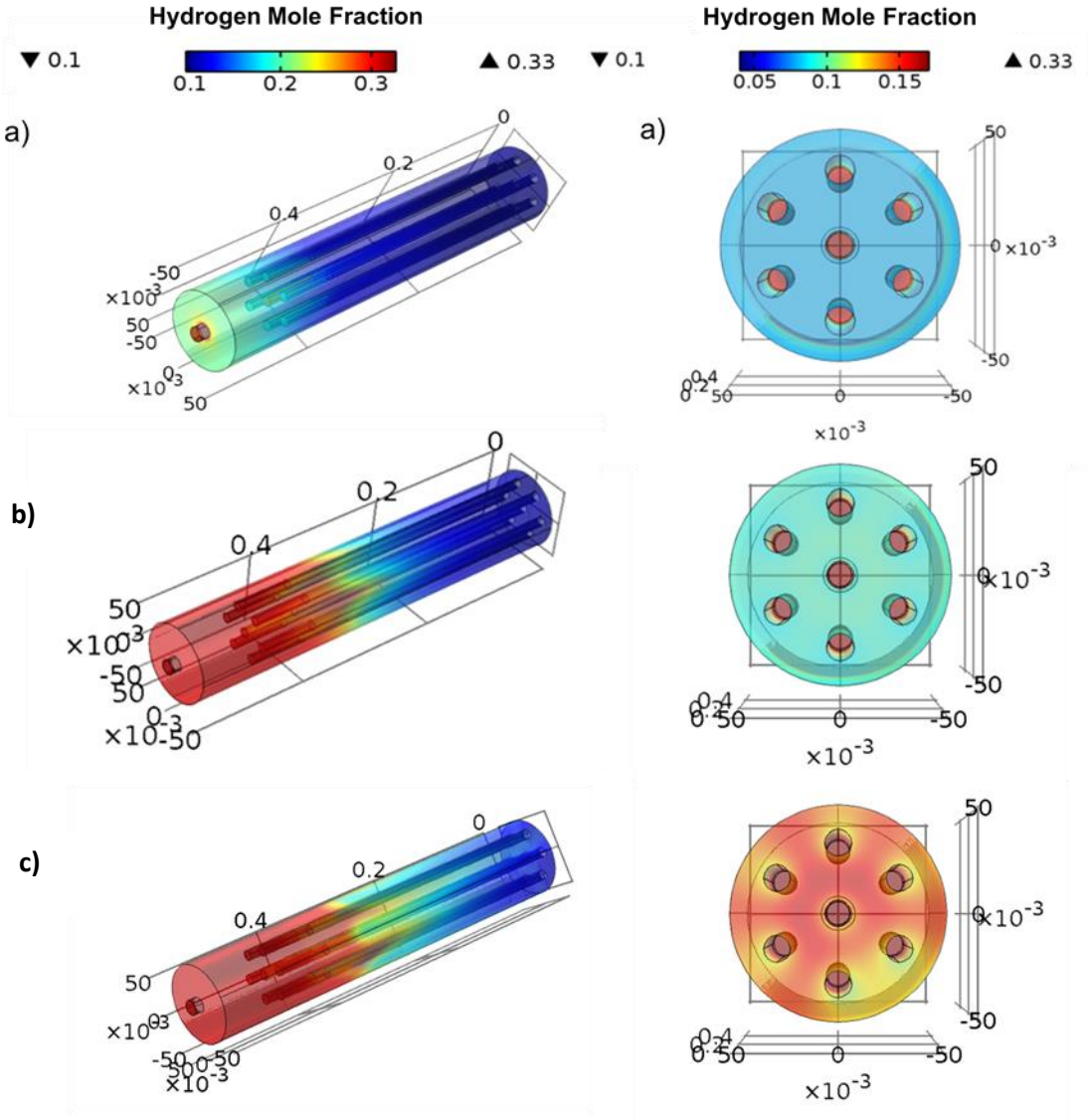

Fig 3.28 Cross-sectional view of the H_2 mole fraction distribution at different Re numbers: a) Low Re number, b) Medium Re, c) High Re

The module shows the formation of a H_2 depleted boundary layer adjacent to the surface of the membrane which is often called concentration polarization (Fig. 3.26). This phenomenon is caused by the slow diffusion of H_2 molecules in the radial direction. Concentration polarization decreases the efficiency of the membrane since the driving force is dictated by the H_2 partial pressure difference between the H_2 molecules located next to the membranes surfaces at the retentate and the tube sides. At the tube side, it was assumed to be uniform since pure H_2 is present. However, at the retentate it changes according to the flow, gas composition and rate of removal. The behavior of concentration polarization can be clearly seen where the bulk syngas located far from the surface of the membrane. The boundary layer of depleted H_2 becomes thicker as the flow moves along the axial direction. At high Re numbers, the boundary layer becomes thinner. This caused by the constant H_2 supply by the advective flow. Therefore, high Re numbers increase the efficiency of the membranes; nonetheless, the H_2 recovery of the process reduces. For the effective utilization of membrane technology, an optimization between recovery and membrane utilization needs to be performed. Fig 3.29 shows the Re number where the recovery and membrane utilization intersect, suggesting an optimal point for operating the module.

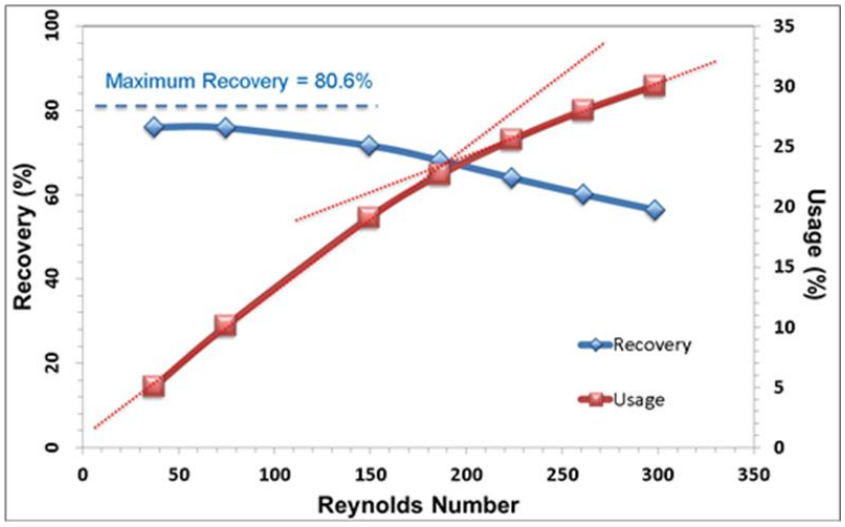

Fig 3.29 Recovery of H_2 and membrane utilization as a function of different Re numbers

The maximum theoretical recovery based on the operating conditions was estimated to be 80.6%, which corresponds to a membrane usage of <5%. At the optimum point, the recovery reaches ~65%, but the usage of the membranes dramatically increased to 25%. After the optimum point, the effect of higher Re numbers keeps improving the usage of the membranes, but to a lower extent. The recovery of H_2 keeps deteriorating after reaching the optimized condition.

3.4.2 Symmetrical non-isothermal model:

Applying the non-isothermal model, the influence of Reynolds number to H_2 recovery as well as concentration polarization shows similar behavior with isothermal model. To further analyze the influence of temperature to the system, H_2 recovery was studied under different feed temperature condition at a fixed feed flow rate.

As shown in Fig 3.30 and Fig 3.31, as feed temperature increases lower H_2 concentration appears at retentate side, which suggested a more significant depletion of H_2 and thus a higher recovery. This is caused by the positive influence of temperature to membrane permeability. Notice that among the two main reasons for mass transfer resistance: resistance of membrane and concentration polarization; temperature can only reduce the one caused by membrane by enhance the permeability, but it does not have any influence on concentration polarization.

Another factor that is influenced by temperature is gas density, which has the expression of:

$$\rho = \frac{p}{RT}\left(\sum_i x_i \cdot M_i\right) \qquad (3\text{-}25)$$

Considering the temperature gradient along the membrane, gas density also changes along the membrane, which makes non-isothermal model more accurate than the previous developed model.

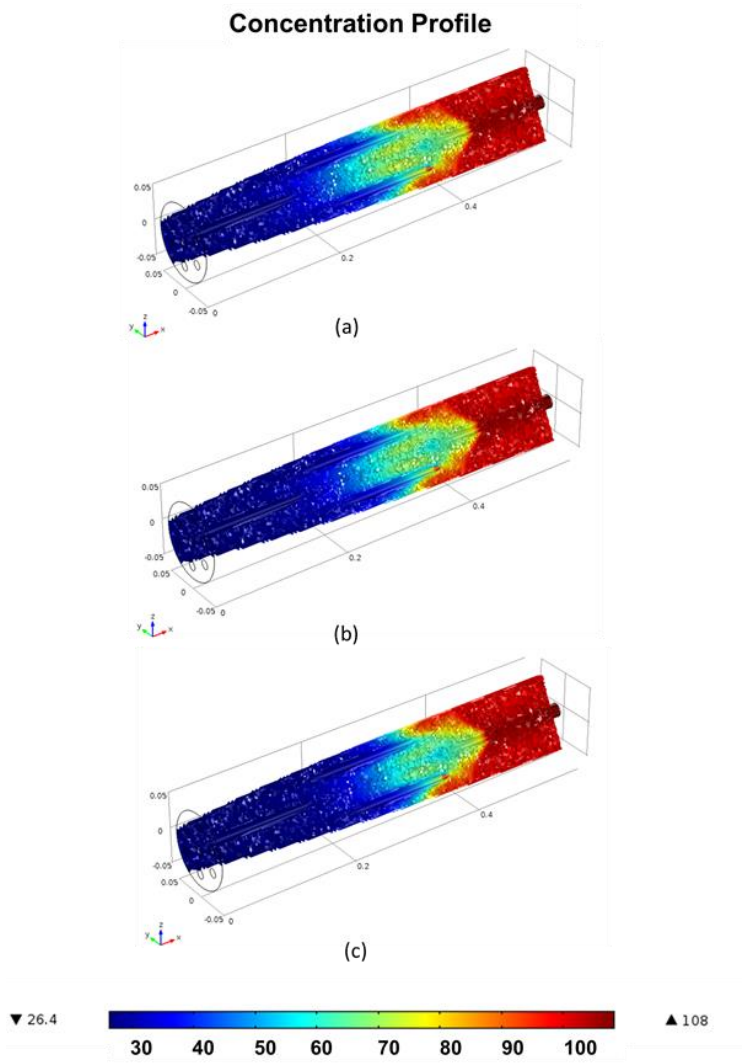

Fig 3.30 Concentration distribution of H_2 at a feed flow rate of 15 ft^3/h with inlet temperature of (a) 523K (b) 600K (c) 723K

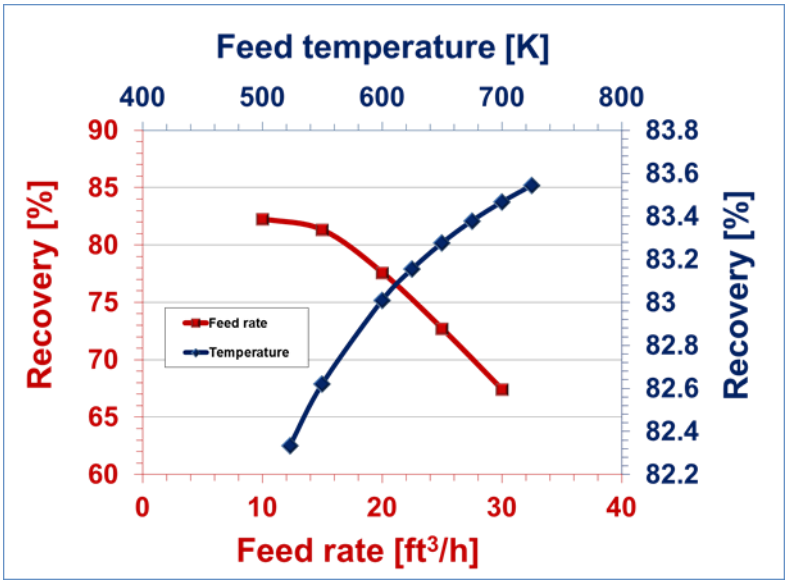

Fig 3.31 Recovery of H_2 as a function of the feed flow rate and feed temperature

3.4.3 Asymmetrical isothermal model:

3.4.3.1 Comparison of the module with and without manifold

Compared with the single-tube membrane module, multitube modules have higher membrane surface area. Due to the different positions of each tube in the module, it is important for us to know whether all the membrane surface area is used equitably. Thus, the H_2 permeation rate of each membrane tube was studied. In the asymmetrical module the retentate outlet is positioned perpendicular to the direction of flow, leading to an uneven distribution of H_2 flux across each membrane tube. This effect can be attenuated by the presence of a manifold. To comparatively evaluate the effect of the manifold, two models (with and without manifold) were developed and studied under the same operating conditions. The gas flow is more symmetrical for the geometry with manifold (Fig 3.32). As a result, the H_2 flux through each outer membrane tube is more evenly distributed (Fig 3.33), which means the membrane area is more efficiently utilized. Since the behavior of the central tube is not influenced by the

manifold, it is not included in figure 3.33. As a result, the geometry with the manifold is used for the simulations. The refined mesh at the membrane tubes is shown in Figure 3.33 as well.

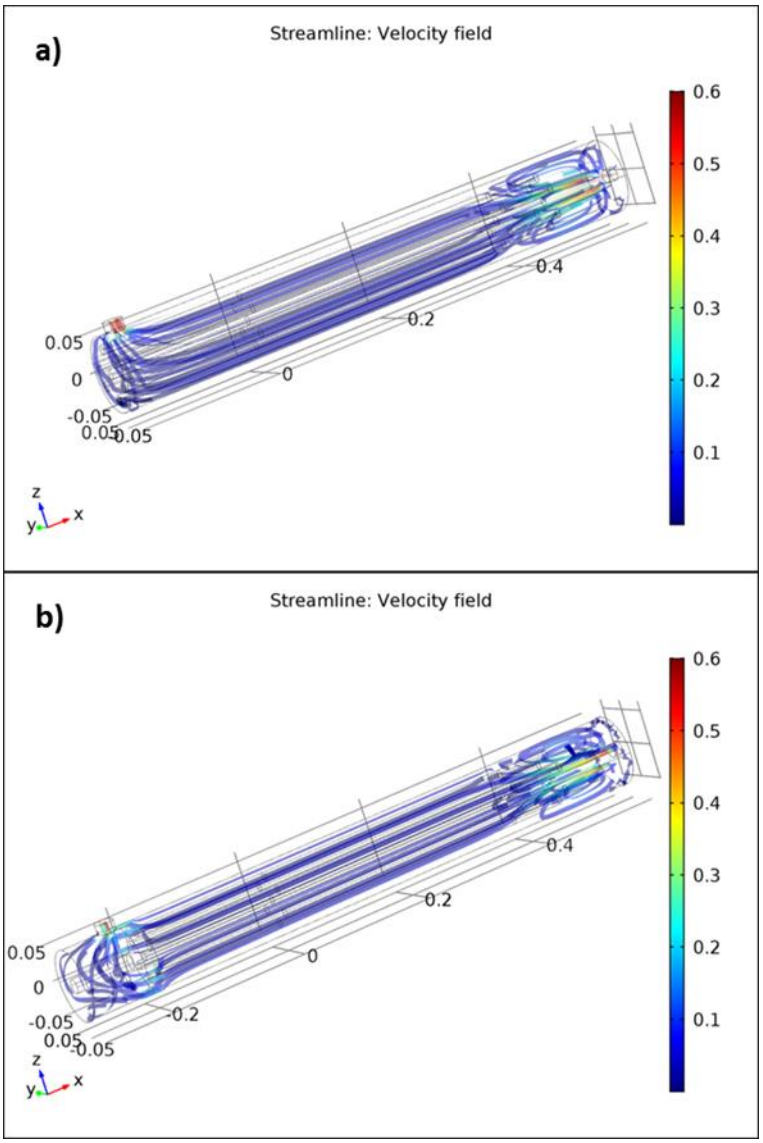

Fig 3.32 Velocity field of the model with different geometry at Q_{in}/A_{mem} = 10.25 $m^3/(h*m_{mem}^2)$

a) Velocity field of the model without manifold b) Velocity field of the model with manifold

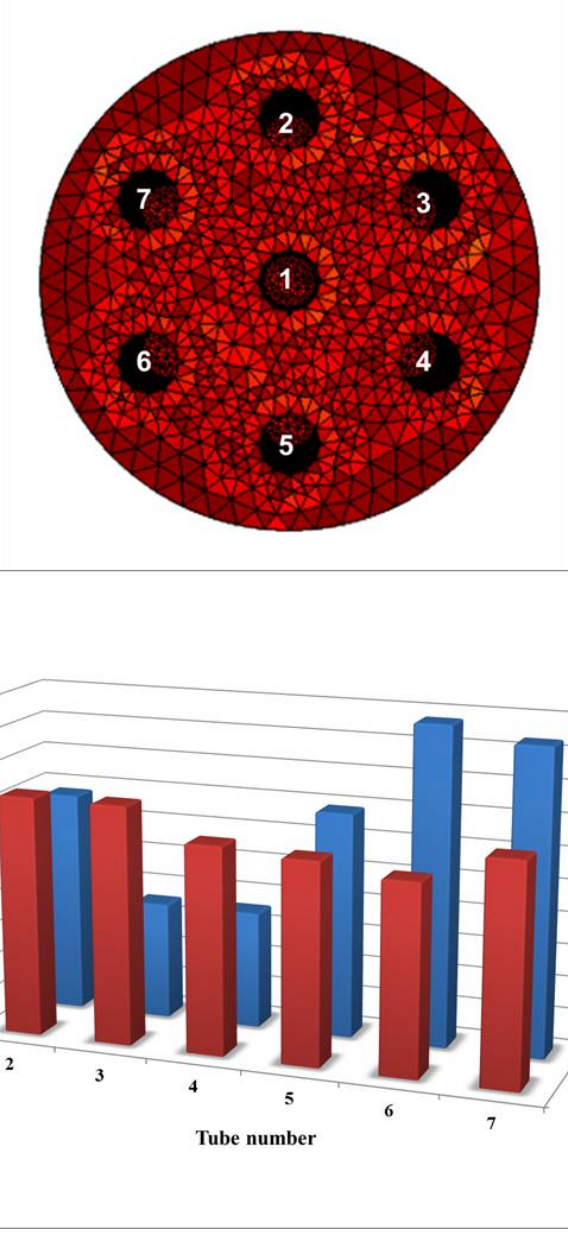

Fig 3.33 Hydrogen flux through each outer membrane tube at Qin/A_{mem} =10.25 m^3/ (h*m_{mem}^2)

For the geometry with manifold, the H_2 flux distribution through all seven membrane tubes is plotted. Membrane tubes are numbered as below in Figure 3.34. The y-axis shows the percentage of H_2 mass flux of each membrane tube from the total amount of collected pure H_2, while the x-axis is the tube number. The operating flow rate per unit membrane area used in the simulation is the experimental value (10.25 m^3/ (h*m_{mem}^2)). The central tube shows slightly

higher H_2 flux compared to tubes on the outer ring because of the more continuous H_2 supply. For the outer layer membranes, the H_2 flux also has a slight variation, as the model is asymmetric. Despite minor differences, the H_2 flux of the tubes are all in a close range, which shows an even distribution of the seven tubes.

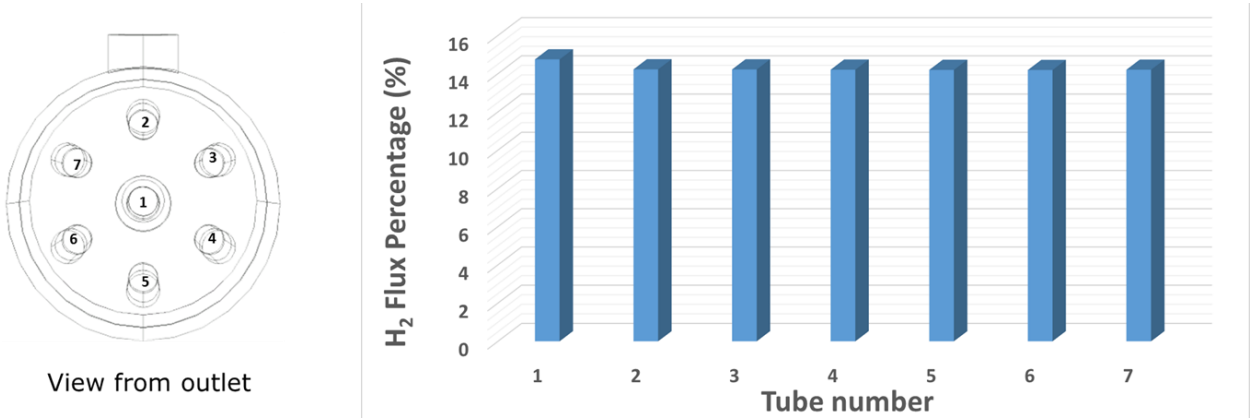

Fig 3.34 Tube-to-tube variation on H_2 mass flux for the 7-tube module at Qin/A_{mem} =10.25 $m^3/(h*m_{mem}^2)$

3.4.4.2 Performance of the seven-tube module

For the process of H_2 permeating through the membrane, two kinds of mass transfer resistances should be considered: i) the resistance caused by the membrane and ii) the resistance from the boundary layer formed by the impermeable species (concentration polarization effect). As H_2 adjacent to the membrane surface is depleted, H_2 from the bulk has to travel through the impermeable gas boundary layer in order to reach the membrane surface. The concentration polarization effect can be seen from the cross-sectional view of the module (Fig 3.35.); the boundary layer with low H_2 concentration can be seen adjacent to the membrane surface.

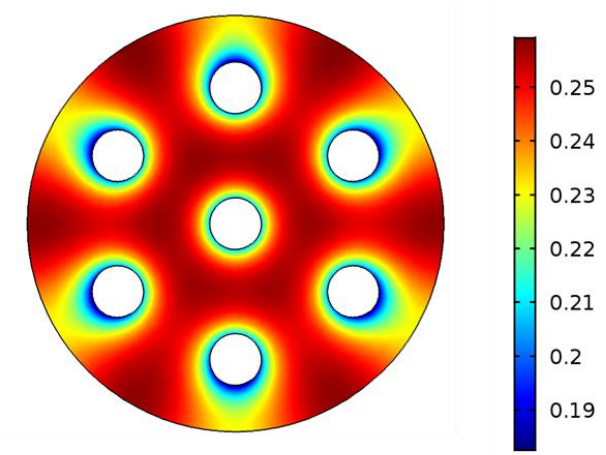

Fig 3.35 Cross-sectional view of the H_2 mole fraction of the membrane module

$Qin/A_{mem} = 8.09\ m^3/(h*m_{mem}^2)$

The previously defined concentration polarization coefficient (CPC) and effective average CPC (EAC) were used to describe the concentration polarization effect of the module quantitatively. Both parameters are in the range of 0 to 1, 0 means that the concentration polarization effect is negligible in the module while 1 means it is extremely severe. When calculating the bulk H_2 partial pressure, the maximum attainable H_2 partial pressure of the cross section at each membrane length was used (Caravella et al. 2016). Different feed inflow rates per unit membrane area in the range of 1.35 $m^3/(h*m_{mem}^2)$ to 13.48 $m^3/(h*m_{mem}^2)$ were studied (Fig 10.).

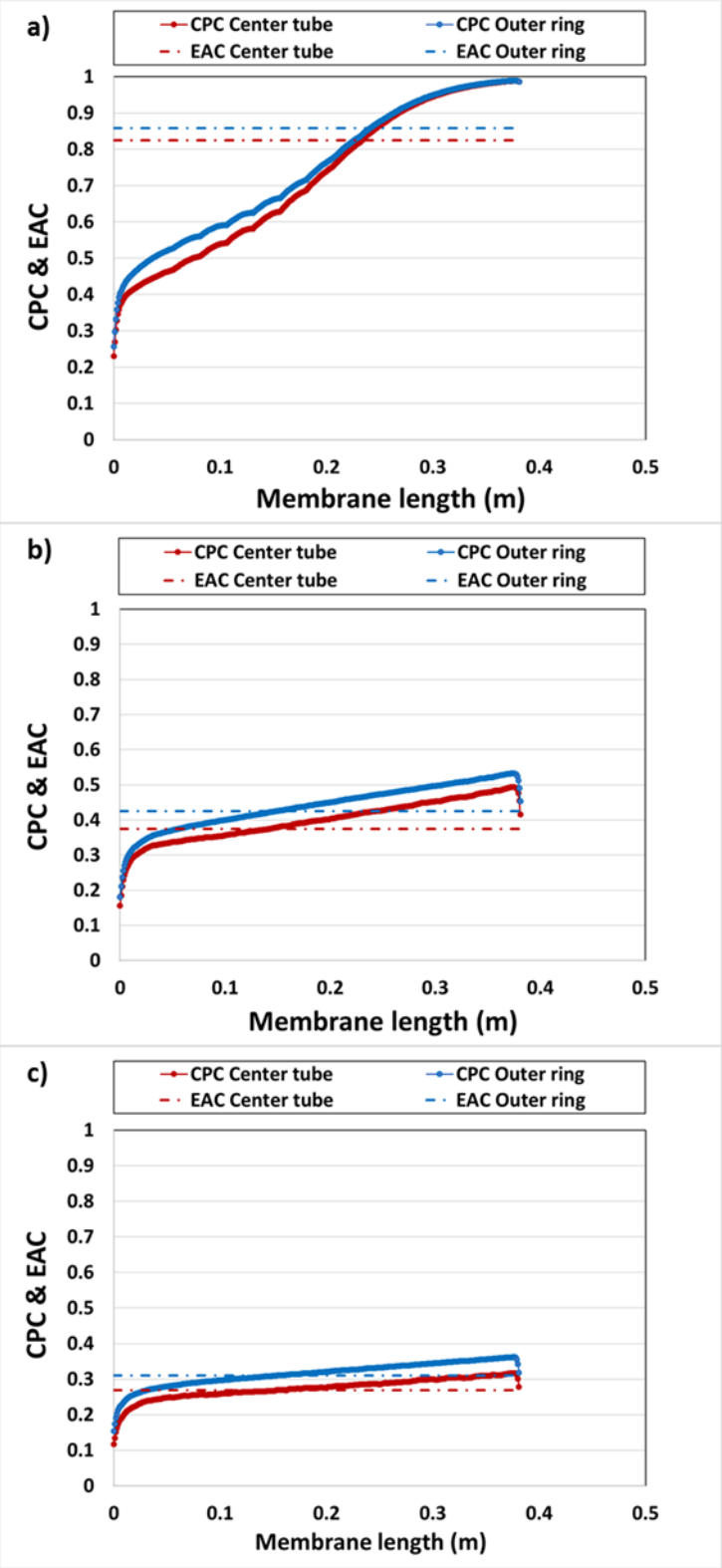

Fig 3.36 Concentration polarization effect of the seven-tube module.

a) Qin/A = 1.35 m^3/ (h*m_{mem}^2), b) Qin/A = 5.39 m^3/ (h*m_{mem}^2), c) Qin/A = 13.48 m^3/ (h*m_{mem}^2)

At the membrane inlet, H_2-enriched syngas encounters the membrane at ideal conditions (no concentration polarization). Nonetheless, radial mass transfer limitations immediately generate concentration polarization at the surface of the membrane. This effect is quite strong at the front end of the membrane, since this section has the highest partial pressure difference. Further along the membrane module, concentration polarization increases steadily with a smaller increase rate. Towards the outlet of the module, the H_2 permeation driving force approaches zero as the retentate side and the permeate side reach equilibrium, resulting in the boundary layer resistance being more dominant compared to the membrane resistance. Finally, at the end of the membrane, a sudden drop in polarization is observed, which could be the result of gas recirculating before entering the manifold. The central tube has a thinner boundary layer and the concentration polarization effect is less severe compared with the outer ring tubes.

At higher convective flow, the boundary layer becomes thinner, which leads to a less severe concentration polarization effect. However, reducing the concentration polarization effect by increasing the flow rate would lead to lower H_2 recovery (Fig 3.36.).

$$\text{Recovery}(\%) = \frac{\mathrm{F}_{\mathrm{H_2}}^{\mathrm{in}} - \mathrm{F}_{\mathrm{H_2}}^{\mathrm{out}}}{\mathrm{F}_{\mathrm{H_2}}^{\mathrm{in}}} \cdot 100 \tag{3-26}$$

$$\text{Usage}(\%) = \frac{\gamma}{\gamma_{\max}} \cdot 100 \tag{3-27}$$

In which, $\mathrm{F}_{\mathrm{H_2}}^{\mathrm{in}}$ and $\mathrm{F}_{\mathrm{H_2}}^{\mathrm{out}}$ represent the amount of H_2 at the inlet and outlet of the module retentate side. γ is the amount of H_2 permeated through the membrane in reality and $\gamma_{\max}$ is the maximum amount of H_2 that can be permeated by the membrane surface area theoretically.

As the flow rate increases, more H_2 is introduced into the module. However, H_2 molecules have less time to diffuse and contact with the membrane surface, thus a smaller percentage of H_2 is collected on the tube side, which leads to a lower H_2 recovery. On the other hand, at lower flow

rates, most of the H_2 is depleted from the shell side soon after being introduced to the module and part of the membrane surface area is wasted, leading to low membrane usage. At higher flow rates, the axial usage of the membranes improves.

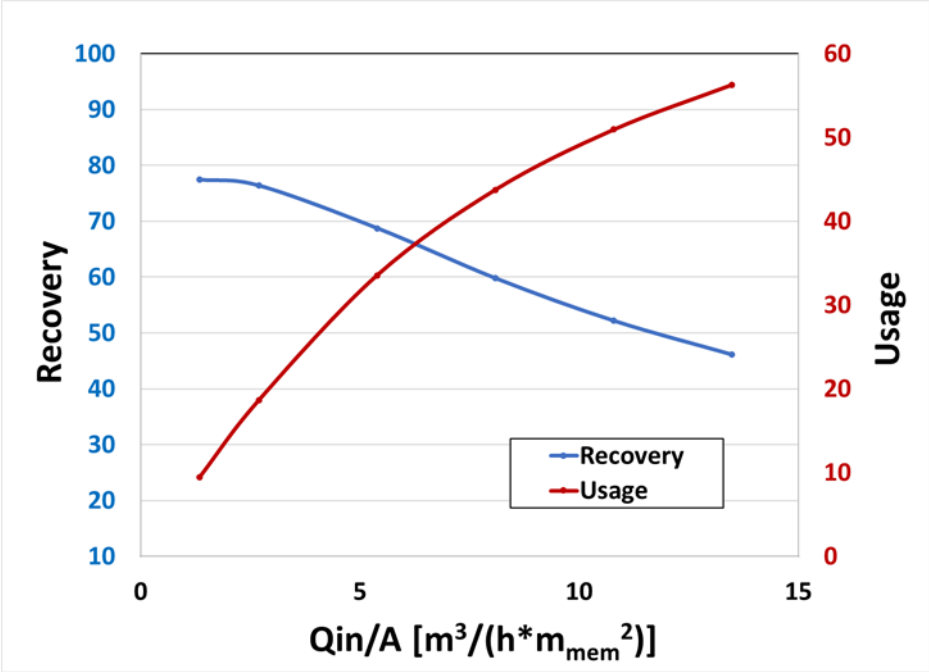

Fig 3.36 Hydrogen recovery and membrane usage of the 7- tube membrane module

With the idea of introducing recirculation into the module, baffles were introduced into the module in order to create recirculation. Modules with one and two baffles were studied under the inflow rate per unit membrane area of 1.35 $m^3/(h*m_{mem}^2)$ (Fig 3.37.).

The concentration polarization profile has the same increasing trend toward the end of the module. When the first baffle was added, the EAC values of the central tube and the outer ring tubes dropped 22% and 10% respectively; this effect is very significant, especially for the central tube. When the second baffle was added, the EAC of the central tube and the outer ring tubes dropped another 4% and 15%. The effect is slightly less significant compared to when the first baffle was added, and the effect is mainly on the outer ring tubes. However, in the 7-tube module, the outer ring membrane tubes permeate most of the H_2; therefore adding the second baffle is still worthwhile, which is in agreement with Coroneo et al. (2010). Notice that in real

industrial applications the module is usually operated under a higher flow rate in order to achieve a reasonable hydrogen recovery, which can result in an even lower polarization effect.

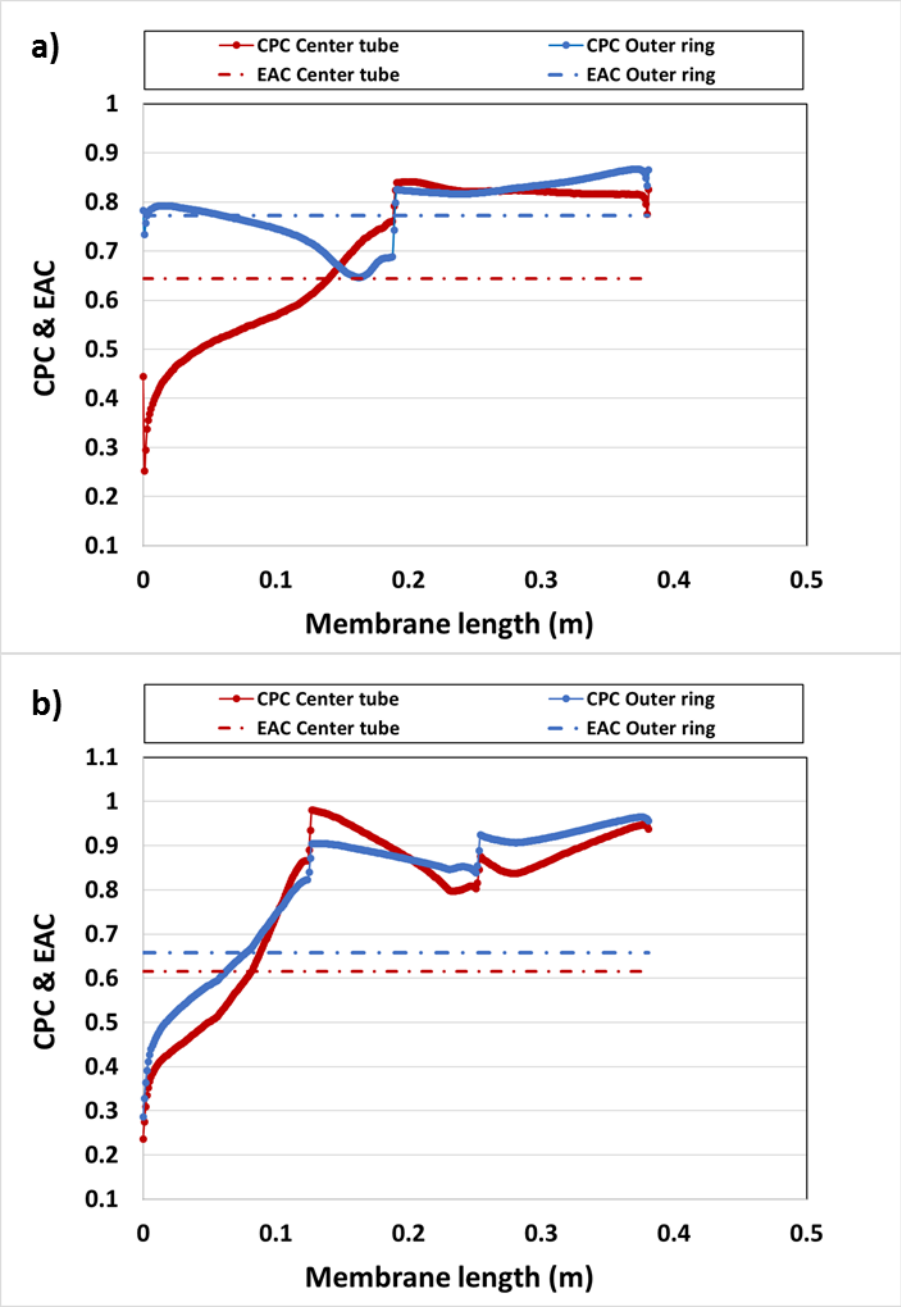

Fig 3.37 Concentration polarization effect of the seven-tube module with baffles

a) One baffle b) Two baffles

Furthermore, while adding baffles can reduce the concentration polarization effect, H_2 recovery is not sacrificed (Table 3-3). Thus, compared with increasing the flow rate, adding baffles to the module is more efficient for reducing mass transfer limitations.

Table 3-3. Hydrogen recovery and membrane usage of modules with different baffle numbers

Baffle number	Hydrogen recovery (%)	Membrane usage (%)
0	76.9	9.3
1	77.6	9.4
2	77.6	9.4

3.4.4.3 Module Scale-up

The concentration polarization effect for the 19-tube module can be seen in Fig 3.38. For the 7-tube module the previously defined parameters CPC and EAC considered the maximum value of the cross-section at each reactor length as the H_2 gas bulk value. However, for the 19-tube module, the H_2 bulk concentration for the outer circle is much lower than the bulk concentration for the central tubes. Thus, using the maximum H_2 partial pressure at each cross section for the bulk H_2 partial pressure would overestimate the EAC of the outer layer membranes. To accurately calculate the EAC value of the membrane tubes on the outer layer, the H_2 mole fraction radial distribution on the shell side for each cross section is plotted (Fig 3.39). The local maximum H_2 partial pressures around each tube is used to calculate the EAC. A detailed explanation can be found in the supplementary material. The concentration polarization effect of the three tube layers is studied by calculating the EAC using the updated local bulk H_2 partial pressure values (Fig 3.40).

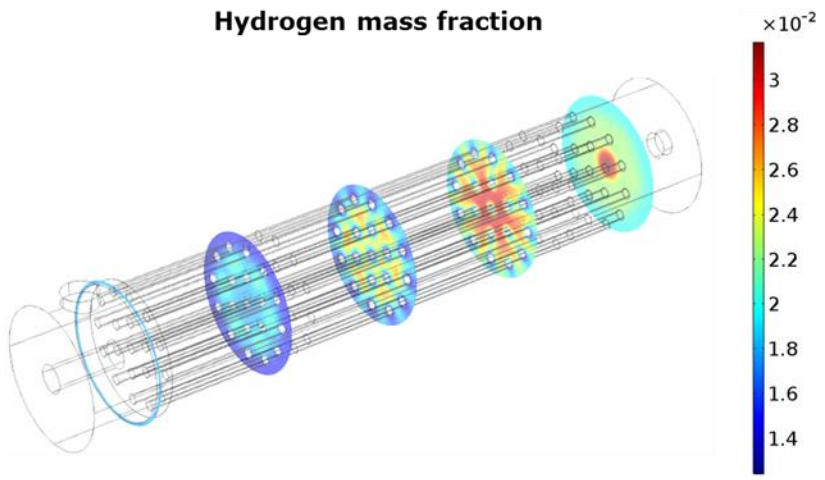

Fig 3.38 Hydrogen mass fraction distribution at Qin / A_{mem}=1.99 m^3/ (h*m_{mem}^2)

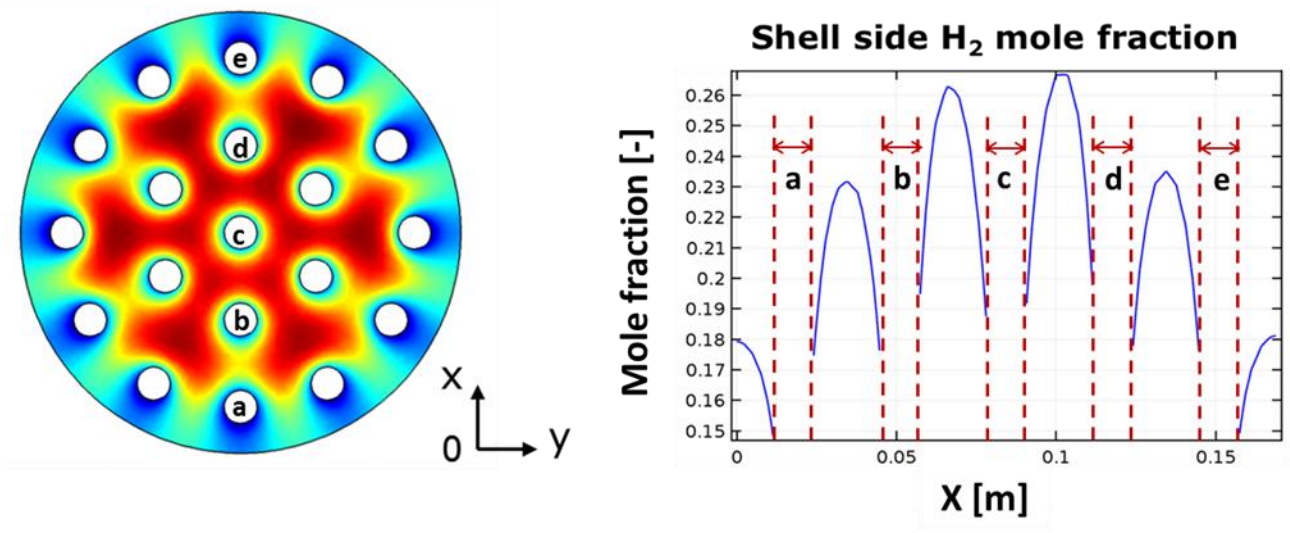

Fig 3.39 Radial distribution of H_2 mole fraction on the shell side

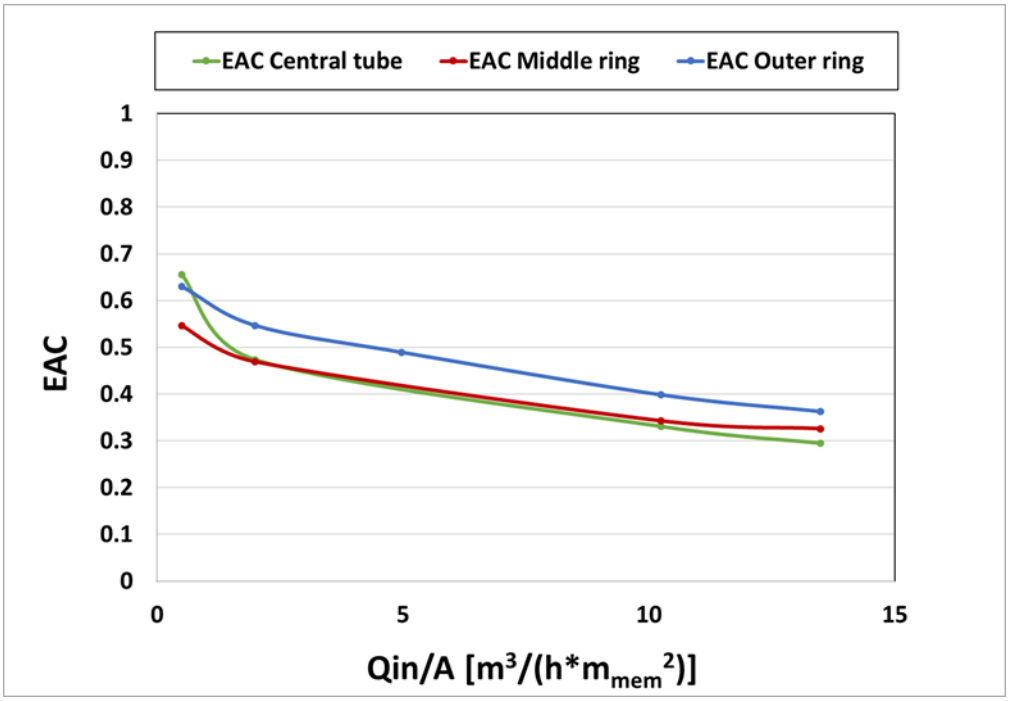

Fig 3.40 EAC profile under different feed inflow rate per unit membrane area

Similar to the seven-tube module, the concentration polarization effect of the inner tubes is less severe than the outer tubes for the majority of the module. The EAC values of the scaled-up module are slightly higher compared with the seven-tube case. The concentration polarization effect is less severe under higher feed flow rate as the boundary layer is thinner.

Hydrogen recovery and membrane usage were further analyzed as shown in Fig 3.42, where the scaled-up module appears to maintain promising H_2 recovery at low flow rate conditions. At high flow rates, the H_2 recovery is lower while membrane usage is higher.

Using the maximum H_2 partial pressure of the cross section can overestimate the concentration polarization effect for the outer layer membrane tubes since the bulk H_2 concentration of the outer layer tubes is lower than the bulk H_2 concentration of central tubes. EAC values with the two kinds of definitions are plotted in order to show the difference (Fig 3.41).

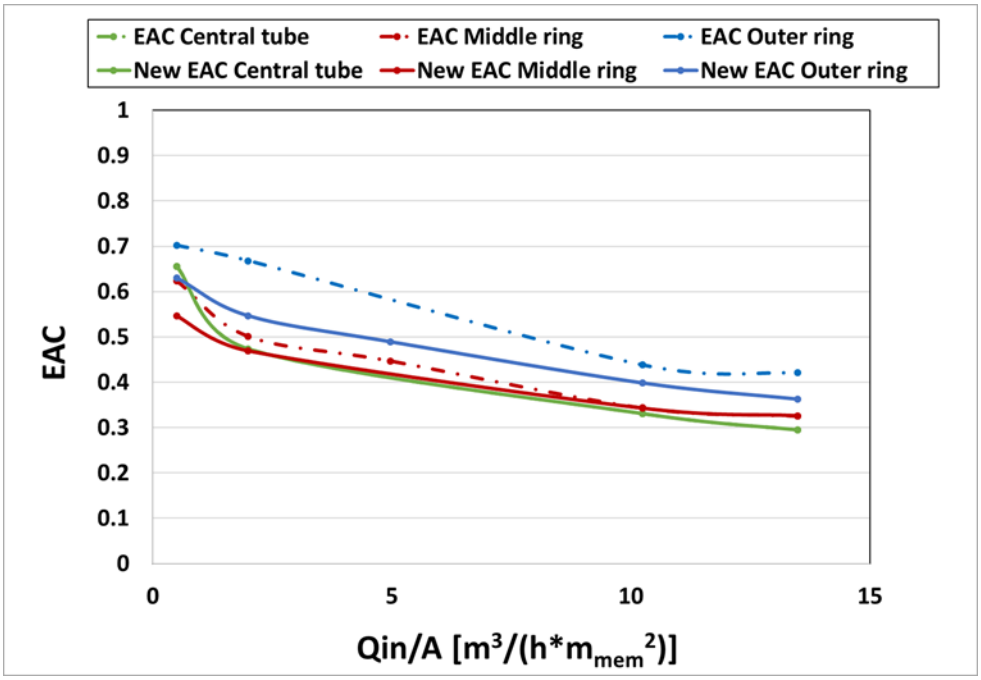

Fig 3.41 EAC plot of the 19-tube module using Maximum H_2 partial pressure of the cross section and Local maximum H_2 partial pressure around the tubes (New EAC plots)

The updated plot shows the same EAC profile for the central tube, a slightly lower profile for the middle ring tubes and a much lower profile for the outer ring, since the maximum bulk H_2 concentration decreases towards the reactor shell radially. For the seven-tube model, it is not necessary to use the local maximum H_2 partial pressure as the outer layer tubes and the central tube share the same maximum H_2 concentration. The difference is lower at a higher flow rate per unit membrane area, which can be explained by the H_2 mole fraction plot at different flow rates (Fig 3.39). At higher flow rate, more radial convection is introduced to the module by recirculation, and the H_2 radial concentration distribution is more even.

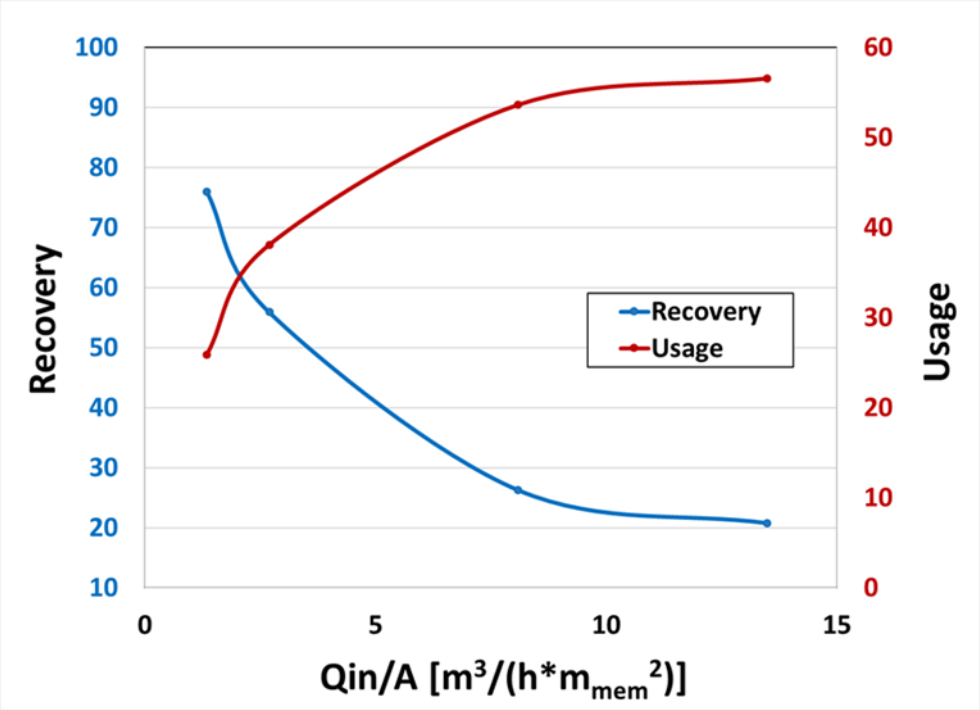

Fig 3.42 Hydrogen recovery and membrane usage of the module under different flow rate (19-tube)

The amount of H_2 permeated by each tube was also studied and is displayed in Fig 3.43. The flow rate per unit membrane area used in this model is again the same as the experimental test at NCCC (10.25 m^3/ ($h*m_{mem}^2$).

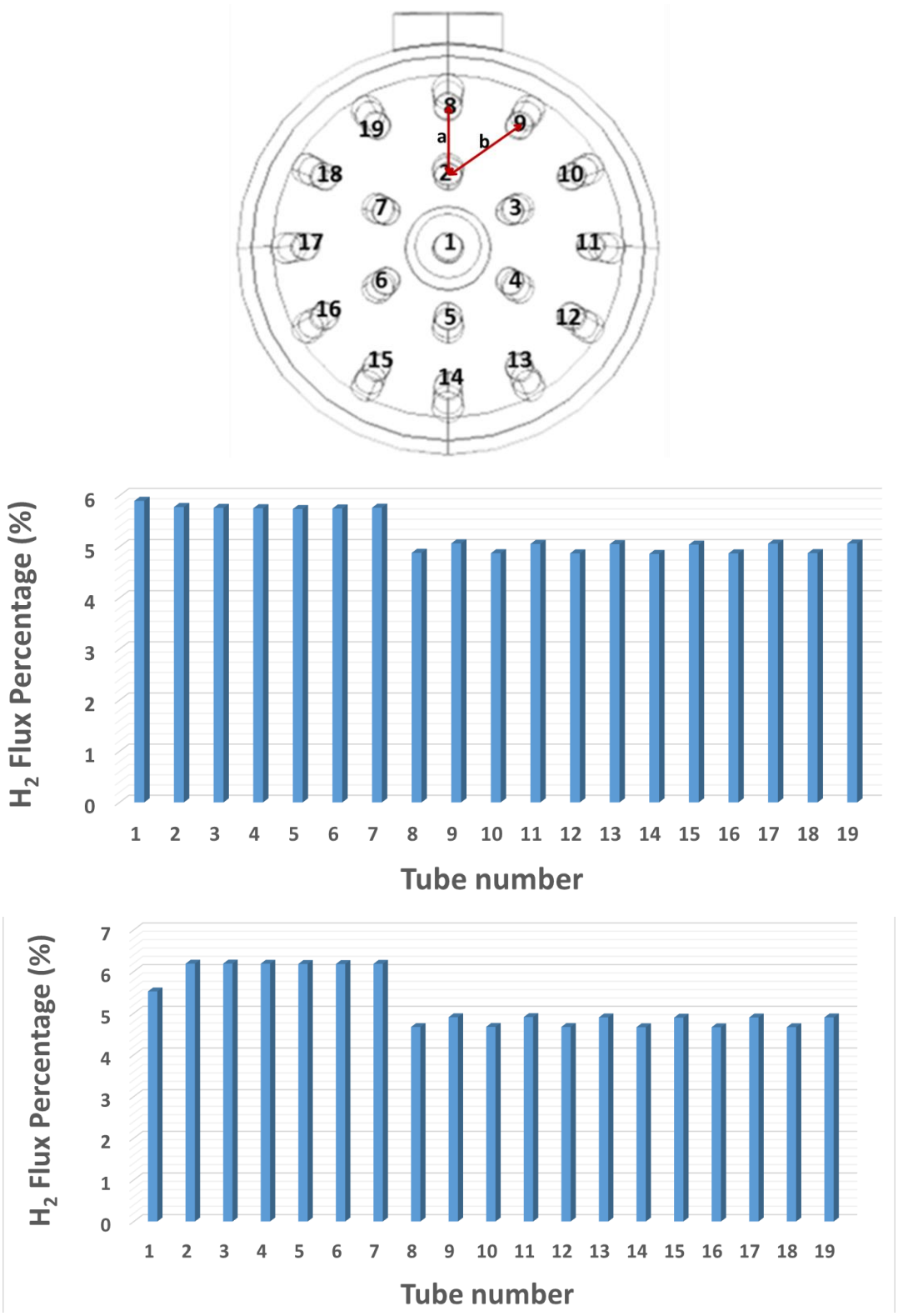

Fig 3.43 Tube-to-tube variation of H_2 mass flux a) 10.25 $m^3/ (h*m_{mem}^2)$, b) 3.78 $m^3/ (h*m_{mem}^2)$

The result showed a similar trend as for the 7-tube module; the inner tubes have higher hydrogen flux while the outer ring tubes have lower H_2 flux. However, compared to the 7-tube module, the differences between different tube-rings are higher as the H_2 concentration is higher for the inner tubes region than for the outer rings (Fig 3.44). This effect is less significant at higher flow rate (Fig 3.43b), as the H_2 concentration is more evenly distributed at such a condition (Fig 3.44). As the flow was introduced to the module, it came across the membrane tubes and generated recirculation inside the module, while the flow rate increased, the recirculation was more noticeable, thus the concentration distribution was more homogenous.

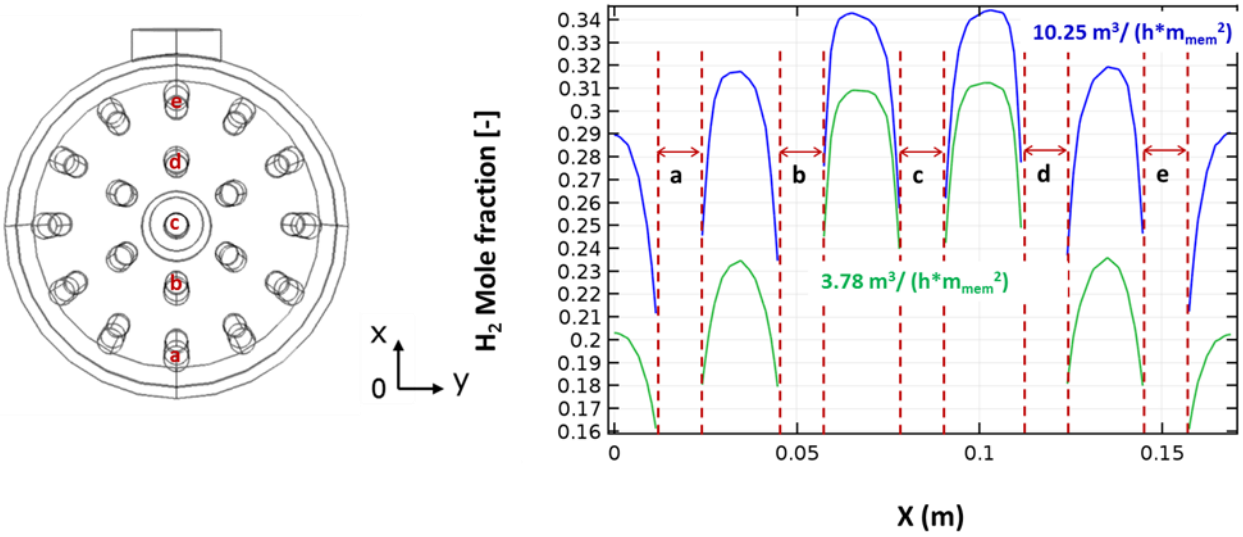

Fig 3.44 Radial distribution of H_2 mole fraction on the shell side

10.25 $m^3/(h*m_{mem}^2)$, 3.78 $m^3/(h*m_{mem}^2)$

The H_2 flux on the outer ring (tubes 8-19 in Fig.3.43) also shows a pattern; even number tubes have lower H_2 flux than odd number tubes. This is the result of even number tubes having more direct competition with middle layer tubes as they are in-line, while the odd number tubes are relatively far from the middle ring tubes in-line with the gap between them. For example in Figure 3.43, the distance between tube 8 and tube 2 is a = 0.0333 m while the distance between tube 9 and tube 2 is b = 0.04124m. The cross section plot on the left in Fig 3.39 can also explain this phenomenon: the H_2 bulk concentration is higher adjacent to the odd number

tubes. Considering the overall effect of flow rate on the concentration polarization along with H_2 recovery and tube-to-tube variation on H_2 flux, the scaled-up module is slightly less promising comparing with the 7-tube module. However, at higher flow rate per unit membrane area, the concentration polarization effect is reduced and the H_2 flux through each membrane tube is more evenly distributed.

3.5 Conclusions

A multitube membrane module with seven membrane tubes and a total membrane surface area of $1050\ cm^2$ was tested in actual coal derived syngas at NCCC, demonstrating the high robustness and excellent physical integrity of composite membranes. The membranes were synthesized over pretreated porous stainless steel supports to form composite asymmetric Pd/Au/Pd layers. The replicability of this technology was demonstrated by the synthesis of membranes with similar thickness and deviating by only 1%. Furthermore, the multitube membrane module was tested for 842.25 hours at 450°C producing a 6 lb/day of high H_2 purity in the range of 99.87-98% throughout the test. The H_2 permeance of the membrane was very stable showing values of 8.8 and 8.2 $Nm^3m^{-2}h^{-1}bar^{-0.5}$ under H_2/N_2 mixture and syngas, respectively. Furthermore, by taking into consideration the nonlinearity of the Sieverts' law, a more realistic average permeance of 16.2 $Nm^3m^{-2}h^{-1}bar^{-0.5}$ was obtained. The H_2 recovery of the module was between 52 - 64% and was a function of the volumetric feed flow rate of the gases. Furthermore, it is clear that the membranes developed displayed a reliable performance under adverse industrial conditions such as those presented in this work including medium-high temperatures, high contaminant concentrations and fluctuations in operating parameters. It can be therefore concluded that this technology could be scaled up and seriously considered as a viable option in industrial applications. Furthermore, in order to study the mass transfer limitations and the performance of each membrane tube, a 3-dimensional asymmetrical CFD simulation was developed, improving on the previously developed symmetrical model. The concentration polarization effect was studied using the defined factors CPC (Concentration polarization coefficient) and EAC (Effective average CPC). Feed flow rates per unit membrane

area in the range of 1.35 - 13.48 $m^3/(h*m_{mem}^2)$, were studied, to demonstrate the disruption of the concentration polarization effect with convective forces (high flow rates). However, increasing the flow rate resulted in a reduction of the H_2 recovery; since H_2 has less time to diffuse through the gas bulk and also has less contact time with the membrane surface. Another way to decrease the concentration polarization effect is to change the module configuration by adding baffles. The simulations were carried out with 1-baffle and 2-baffle configurations under the condition 1.35 $m^3/(h*m_{mem}^2)$ (gas flow rate per unit membrane area). The models displayed a reduction in concentration polarization when baffles are added, caused by adding radial convection (gas recirculation). Compared with increasing the flow rate, adding baffles can decrease the concentration polarization effect while maintaining the H_2 recovery, which is more efficient. The tube-to-tube H_2 flux variation study shows an even H_2 flux distribution despite the minor variations. The module was scaled up to a 19-tube module by adding an outer ring of 12 membrane tubes. The concentration polarization effect was slightly more severe compared with the seven-tube module, but can be reduced by increasing flow rate. The tube-to-tube performance variation was more unbalanced for the 19-tube module under the experimental operating condition and the difference is more significant under lower flow rate conditions. Large-scale membrane reactors require special considerations for optimum operation. Specifically, radial mass transfer limitations and the tube-to-tube variation must be thoroughly analyzed, as they are the major issue with large-scale membrane module design.

4. Ethanol steam reforming in catalytic membrane reactors

------ Published as "Experimental and simulation studies of the production of renewable hydrogen through ethanol steam reforming in a large-scale catalytic membrane reactor." Chemical Engineering Journal 303 (2016): 302-313 and "CFD study of heat and mass transfer in ethanol steam reforming in a catalytic membrane reactor." International Journal of Hydrogen Energy 43(2017):7662-7674

4.1 Materials and experimental methods

A palladium membrane with a surface area of 150 cm^2 was manufactured using a porous stainless steel (PSS) support from Mott Metallurgical Corp. The porous support has a length of 0.381 m and an outer diameter of 0.0127m, with a porous media grade of $5*10^{-7}$ m. The membrane synthesis process is carried out using the previous developed method (Ma et al. 2007, Ma et al. 2000, Ma et al. 2008, Ma et al. 2007, Mardilovich et al. 1998). The support was first cleaned in an ultrasonic bath using isopropanol, followed by the oxidation process for 12 hours under 600 ^oC in air. The support is then graded with two kinds of pre-activated Pd-Al particles with 2 wt% from Johnson Matthey (UK). The first kind is the coarse particles with an average size of 1-3 μm, the second type is the fine particles with the size of 0.6 μm. Then the grading layer is cemented through electroless plating of palladium. Afterwards, the membrane was activated using $SnCl_2$ and $PdCl_2$, and then a layer of Pd is plated. In addition, gold was subsequently deposited on the membrane surface through electroplating. Palladium-gold alloy is proved to be the most stable alloy for membranes. The Tamman temperature of gold (395 ^oC) is much lower than the Tamman temperature of palladium (641 ^oC), while operating at the temperature in between two Tamman temperatures, which usually is the case, gold would have a higher molecular mobility compare to palladium. Gold would cross the boundary of the two metals and diffuse into Pd layer, while palladium remains relatively stable. This would allow gold to behave like a patching paste for the voids and defects on palladium layer (Mardilovich et al. 2015). Besides, adding gold was also found to be beneficial to the membrane permeance and the membrane lifetime while the membrane is poisoned by H_2S or other contaminants (Chen et al. 2010, Guazzone et al. 2013). The total surface area of the membrane is 150 cm^2 and

the thickness of the palladium layer was measured by gravimetric measurement; the feasibility at each plating step was measured by Helium leak test (Fig.4.1).

The membrane was used in the reaction while the thickness was at 13 µm, when the helium leakage reached the lowest. At this point, the membrane has a permeance of 80 $Nm^3m^{-2}h^{-1}bar^{-0.5}$ at 450 ^oC. During the operation, the membrane displayed a helium leakage increase thus it was re-plated with Pd and Au and reached a thickness of 20 µm with a composition of Pd 6.9 µm/Au 0.2 µm/Pd 6.7 µm/Au 0.1 µm. In order to prevent the catalyst from contacting with the membrane surface, a protective double-screened cage was designed for the catalysts (Fig 4.2). The catalysts were loaded in between the two screens and the cage guaranteed that the membrane is in close contact with the catalysts and the reaction area. Catalysts used in the reaction are nickel-based catalyst (HiFUEL R110, from Alfa Aesar). Before loading into the cage, the 220g catalysts were crushed and sieved (16/+40 mesh). The outer diameter of the reactor shell is 0.0286m and the length is 0.4064m. The reaction takes place on the shell side and pure hydrogen is collected from the tube side. The reactor is then installed into a well-insulated oven in order to provide heat for this endothermic reaction. Thermal couples are placed on the shell in order to provide the accurate shell temperature for simulation studies as the set oven temperature is not necessarily the same as the shell temperature. Ethanol and steam with different steam to ethanol ratio was fed into the system after going through a pre-heat which brings the temperature up to the shell temperature.

During the reaction, carbon deposition can occur and block the active sites on the catalyst surface. However, it was reported that under low temperature (350-500 ^oC) and the presence of H_2 the carbon deposition could be diminished (Beurden et al 2004). Before starting the hydrogen permeation test, helium was fed to the system to ensure that there is no air or moisture in the reactor, Sweep has was introduced into the permeate side the reactor with a flow rate of 65 ml/min in order to reduce the hydrogen partial pressure on the permeate side.

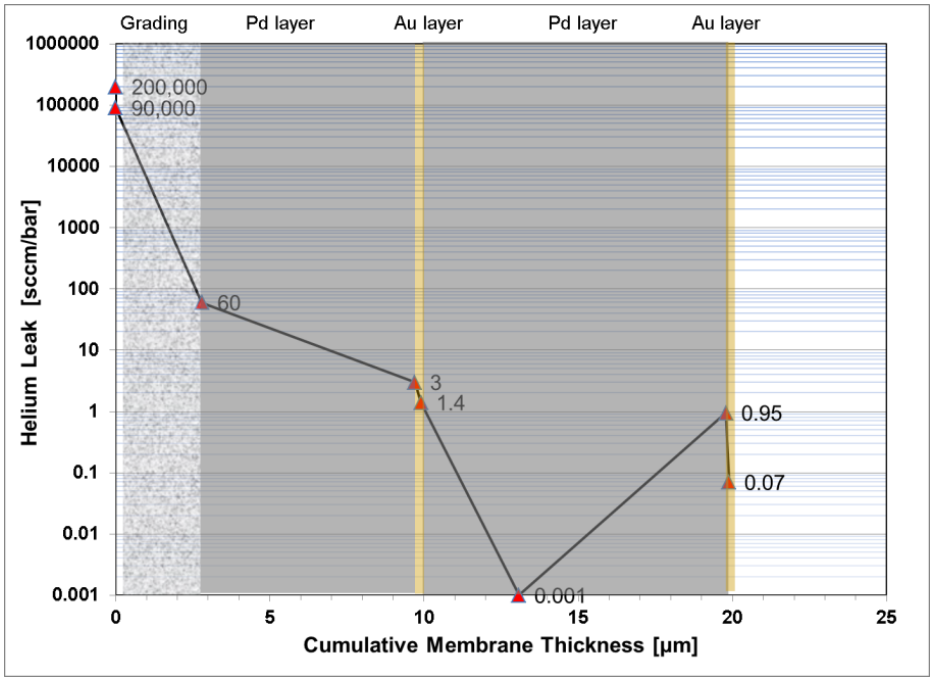

Fig 4.1 Helium leak tests as a function of the different synthesized layers

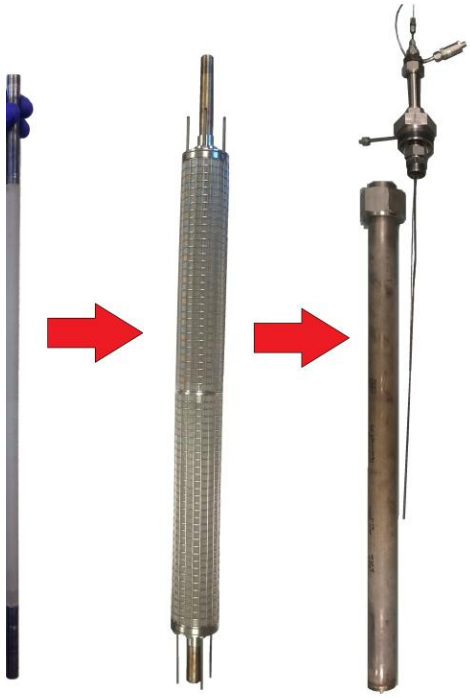

Fig 4.2 Picture of the membrane, membrane-cage assembly and shell of the CMR module

4.2 Simulation methods

Ethanol steam reforming is a highly endothermic reversible process which prefers high temperature, low pressure and low space velocities. The kinetics of this process has been widely studied and different mechanisms are reported by literature (Murmura et al. 2015; Mas et al. 2008; Palma et al. 2012; Bshish et al. 2011; Peela et al. 2011; Olafadehan et al. 2015; Patel et al. 2013; Du et al. 2011). However, the four reactions are considered the most representative reactions (Sun et al. 2005):

ESR	$C_2H_5OH \leftrightarrow CH_4 + CO + H_2$	$\Delta H_{298K} = 49\ kJ/mol$	(4-1)
WGS	$CO + H_2O \leftrightarrow CO_2 + H_2$	$\Delta H_{298K} = -41\ kJ/mol$	(4-2)
MSR	$CH_4 + H_2O \leftrightarrow CO + 3H_2$	$\Delta H_{298K} = 206\ kJ/mol$	(4-3)
MSR	$CH_4 + 2H_2O \leftrightarrow CO_2 + 4H_2$	$\Delta H_{298K} = 165\ kJ/mol$	(4-4)

The kinetics reported by Sun et al. (2005) and Xu et al. (1989) (Table 4-1) are considered for the simulations. Before starting the experiment and the CFD simulation, a 1-D simulation with Polymath was carried on which served two purposes: 1) to help understand the operating conditions range in the experiment, 2) to verify the accuracy of the kinetics before implementing to the CFD simulation. The 1-D code can be found in the supplementary material. The kinetics were applied in the 1-D simulations of ethanol steam reforming in traditional packed bed reactors and the results are compared with the experimental results that were reported in the literatures (Patel et al. 2013; de-Souza et al. 2013). The kinetics showed a >99% accuracy for the simulation of ethanol steam reforming reactions.

Table 4-1. Summary of the kinetic expressions used in the simulation framework

$r_1 = k_1 P X_e$	$[\text{mol } g_{cat}^{-1} s^{-1}]$	(4-5)
$r_2 = (k_2 P / X_h den^2)[X_{co} X_w - X_{CO_2} X_h / K_2]$	$[\text{mol } g_{cat}^{-1} s^{-1}]$	(4-6)
$r_3 = (k_3 / X_h^{2.5} den^2 \sqrt{P})[X_M X_W - X_{CO} X_h^3 P^2 / K_3]$	$[\text{mol } g_{cat}^{-1} s^{-1}]$	(4-7)
$r_4 = (k_4 / X_h^{3.5} den^2 \sqrt{P})[X_M X_W^2 - X_{CO_2} X_h^4 P^2 / K_4]$	$[\text{mol } g_{cat}^{-1} s^{-1}]$	(4-8)
$k_1 = (4.55 \times 10^{-5}/T)\exp(-2030/T)$	$[\text{mol } Pa^{-1} g_{cat}^{-1} s^{-1}]$	(4-9)
$k_2 = 5.43 \times 10^{-3}\exp(-8074.33/T)$	$[\text{mol } Pa^{-1} g_{cat}^{-1} s^{-1}]$	(4-10)
$k_3 = 3.711 \times 10^{14}\exp(-28879/T)$	$[\text{mol } Pa^{0.5} g_{cat}^{-1} s^{-1}]$	(4-11)
$k_4 = 8.960 \times 10^{13}\exp(-29336.1/T)$	$[\text{mol } Pa^{0.5} g_{cat}^{-1} s^{-1}]$	(4-12)
$K_2 = \exp(4400/T - 4.036)$		(4-13)
$K_3 = 1 \times 10^{10}\exp(-26830/T + 30.114)$	$[Pa^2]$	(4-14)
$K_4 = K_2 K_3$	$[Pa^2]$	(4-15)
$den = 1 + P(K_{CO} X_{CO} + K_h X_h + K_M X_M) + K_W X_W / X_h$		(4-16)
$K_{CO} = 8.230 \times 10^{-10}\exp(8497.71/T)$	$[Pa^{-1}]$	(4-17)
$K_M = 6.640 \times 10^{-9}\exp(4604.28/T)$	$[Pa^{-1}]$	(4-18)
$K_h = 6.120 \times 10^{-14}\exp(9971.13/T)$	$[Pa^{-1}]$	(4-19)
$K_W = 1.770 \times 10^{5}\exp(-10666.35/T)$	$[Pa^{-1}]$	(4-20)
$R_{C\_CO} = (r_1 - r_2 + r_3) \cdot W_{cat} \cdot M_{CO} / V_r$	$[kg(m^3 \cdot s)^{-1}]$	(4-21)
$R_{C\_CO2} = (r_2 + r_4) \cdot W_{cat} \cdot M_{CO2} / V_r$	$[kg/(m^3 \cdot s)^{-1}]$	(4-22)
$R_{C\_H2} = (r_1 + r_2 + 3 \cdot r_3 + 4 \cdot r_4) \cdot W_{cat} \cdot M_{H2} / V_r$	$[kg/(m^3 \cdot s)^{-1}]$	(4-23)
$R_{C\_H2O} = (-r_2 - r_3 - 2 \cdot r_4) \cdot W_{cat} \cdot M_{H2O} / V_r$	$[kg/(m^3 \cdot s)^{-1}]$	(4-24)
$R_{C\_CH4} = (r_1 - r_3 - r_4) \cdot W_{cat} \cdot M_{CH4} / V_r$	$[kg/(m^3 \cdot s)^{-1}]$	(4-25)
$R_{C\_C2H5OH} = -r_1 \cdot W_{cat} \cdot M_{C2H5OH} / V_r$	$[kg/(m^3 \cdot s)^{-1}]$	(4-26)

4.2.1 1-D Simulation

At first, a 1-d model was developed utilizing Polymath with the purpose of understanding the operating conditions needed in the experimental rig. The kinetic expressions for a Ni-based catalyst proposed by Sun et al. (2005) and Xu et al (1989) were utilized and are presented in Table 3. It is important to mention that these kinetic parameters were used to simulate ESR in conventional reactors; and the results were compared with experimental results presented in the literature (Patel et al. 2013; de-Souza et al. 2013). The kinetics showed a >99% (Fig 4.3) accuracy in predicting different convergences and yields. Yield is defined as:

$$Y_{H2} = \frac{F_{H_2}}{F_{e0}} \tag{4-27}$$

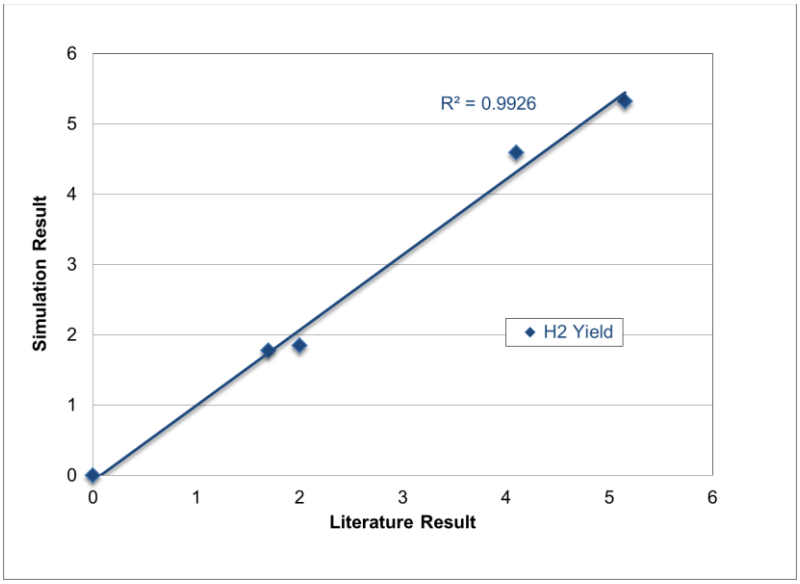

Fig 4.3 1-D reaction kinetics validation with literature.

The H_2 flux across the membrane was simulated according to Sieverts' law and utilizing the experimental value of the permeance ($\overline{P_{H_2}}$) as shown in Eq. 4-28, where $P_{H_2}^{shell}$ and $P_{H_2}^{tube}$ represent the H_2 partial pressure on the shell and inside the tube, respectively. On the retentate side (reaction zone) a negative H_2 flux through the membrane boundary was defined

as a function of applying Sieverts' law. On the permeate side of the membrane boundary, the same expression, but positive, was defined to simulate the H_2 concentration profile.

$$-\mathrm{n}\cdot \mathrm{N_i} = \overline{\mathrm{P_{H_2}}}\left[\sqrt{\mathrm{P_{H_2}^{shell}}} - \sqrt{\mathrm{P_{H_2}^{tube}}}\right] \quad (4\text{-}28)$$

4.2.2 2-D iso-thermal CFD simulation

First, a 2-D iso-thermal CFD simulation was carried out in Comsol Multiphysics with the previous validated kinetics. The simplified 2-D geometry used in the simulation is shown in Figure 4.4. The assumptions of the simulation included:

1) The cage designed to separate the catalysts and the membrane surface is not considered in the simulation. It is assumed that the cage does not introduce any disturbance to the flow.
2) The system is isothermal and under laminar flow.
3) The 2-D simplified geometry with both shell side and tube side is applied in the simulation.

Due to the present of the sweep gas on the permeate side, hydrogen partial pressure is lower on the tube side, and it varies with the sweep gas flow rate.

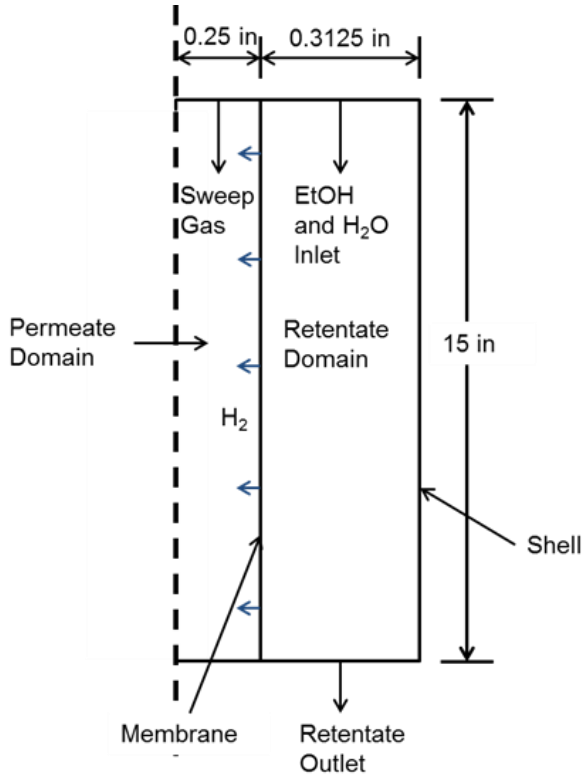

Fig 4.4 Geometry used in the 2-D CFD simulation model

In Comsol, the physics "Reacting flow in porous media (Concentrated Species)" is used for the retentate side considering the effect of the catalyst bed, for the permeate side, "Transport of concentrated species" and "Laminar flow" were coupled. The effectiveness factor η is calculated to be 1, thus in this case the reaction is reaction rate limited (Fogler et al. 2005).

For retentate side, equation of motion and continuity equations are solved within the geometry mesh which contains 93,152 domain elements.

$$(\rho/\varepsilon_P)\big((u\cdot\nabla)u/\varepsilon_P\big) = \nabla\cdot\left[-pI + \mu/\varepsilon_P\big(\nabla u + (\nabla u)^T\big) - (2\mu/3\varepsilon_p)(\nabla\cdot u)I\right] - (\mu k^{-1} + \beta_F|u|)u + F \quad (4\text{-}29)$$

$$\nabla\cdot(\rho u) = 0 \quad (4\text{-}30)$$

$$\nabla\cdot j_i + \rho(u\cdot\nabla)w_i = R_i \quad (4\text{-}31)$$

In which ε_P is the catalyst bed porosity, β_F is the Forchheimer coefficient.

For permeate side:

$$\rho(u \cdot \nabla)u = \nabla \cdot [-pI + \mu(\nabla u + (\nabla u)^{T}) - (2/3)\mu(\nabla \cdot u)I] + F \quad (4\text{-}32)$$

$$\nabla \cdot (\rho u) = 0 \quad (4\text{-}33)$$

$$\nabla \cdot j_i + \rho(u \cdot \nabla)w_i = 0 \quad (4\text{-}34)$$

For the boundary condition at the membrane, Sieverts' law is used to describe the hydrogen flux through the membrane:

$$-n \cdot N_i = \overline{P_{H_2}}[\sqrt{P_{H_2}^{shell}} - \sqrt{P_{H_2}^{tube}}] \quad (4\text{-}35)$$

The membrane permeance $\overline{P_{H_2}}$ is from the experimental value. $P_{H_2}^{shell}$ and $P_{H_2}^{tube}$ represent hydrogen partial pressure on shell side and tube side of the membrane. For the retentate side, a negative hydrogen flux is defined using Sieverts' law while for the permeate side, a positive hydrogen flux is defined using the same expression.

In the simulation, density of the gas mixture is a function of the composition, which changes while the reaction and separation take place. Furthermore, the diffusion coefficient($\mathfrak{D}_m$) is calculated using the following equation:

$$\mathfrak{D}_m = 0.0018583\sqrt{T^3(1/M_A + 1/M_B)}(1/p\sigma_{AB}^2\Omega_{\mathfrak{D},AB}) \quad (4\text{-}36)$$

Where σ_{AB} was from the Lennard-Jones parameters, T is the temperature of the gases; p is the pressure in the module and $\Omega_{\mathfrak{D},AB}$ is the collision integral (Bird et al. 2007). Considering the effect of the catalyst bed, longitudinal and transverse dispersion coefficient ($\mathfrak{D}_L$ and $\mathfrak{D}_T$) are calculated with Eq 4-39 & 4-41 (Delgado 2006).

$$Pe_m = Re \cdot Sc \quad (4\text{-}37)$$

$$1/Pe_L = 1/(\tau \cdot Pe_m) + 1/2 \quad (4\text{-}38)$$

$$\mathfrak{D}_L = ud/Pe_L \tag{4-39}$$

$$1/Pe_T = 1/(\tau \cdot Pe_m) + 1/12 \tag{4-40}$$

$$\mathfrak{D}_T = ud/Pe_T \tag{4-41}$$

Where Pe_L and Pe_T are the longitudinal and transverse Péclet numbers, τ is tortuosity and d is the catalyst average particle diameter.

4.2.3 2-D non-isothermal CFD simulation

For the non-isothermal simulation, the same 2-D symmetrical geometry and kinetics expressions were used. However, in the non-isothermal simulation, temperature is defined as a variable and coupled with energy balance equations. Furthermore, the membrane permeance is also defined as a function of temperature. The simulation was carried out in the finite element software Comsol Multiphysics as well. After the boundary mesh refinement, the model has 235813 elements. Effectiveness factor η is calculated to be 1 using the Thiele modulus for a spherical catalyst pellet, the reactions are surface-reaction limited and the diffusion within the pellet can be neglected in the simulation. Assumptions in the simulation includes:

1) The effect of the cage is neglected assuming it does not change the flow pattern in the module.
2) Carbon deposition has minor effect on hydrogen permeance of the membrane and can be neglected.

The simulation calculated the momentum, heat and mass transfer balance for both side of the module:

Continuity (Both sides):

$$\nabla \cdot (\rho \underline{v}) = 0 \tag{4-42}$$

Equation of motion:

1. Retentate side (porous media reacting flow):

$$(\rho/\varepsilon_P)\left((\underline{v}\cdot\nabla)\underline{v}/\varepsilon_P\right)=\nabla\cdot\left[-p\mathbf{I}+\mu/\varepsilon_P\left(\nabla\underline{v}+(\nabla\underline{v})^T\right)-(2\mu/3\varepsilon_p)(\nabla\cdot\underline{v})\mathbf{I}\right]-\left(\mu k^{-1}+\beta_F|\underline{v}|\right)\underline{v}+\underline{F} \quad (4\text{-}43)$$

$$k=\frac{d^2\varepsilon_p^3}{150(1-\varepsilon_p)^2} \quad (4\text{-}44)$$

$$\beta_F=\frac{C_f\cdot\rho}{2} \quad (4\text{-}45)$$

$$C_f=\frac{3.5(1-\varepsilon_p)}{d\cdot\varepsilon_p^3} \quad (4\text{-}46)$$

Where k is the packed bed permeability which is calculated to be 9.26×10^{-10} m^2, and β_F is the Forchheimer coefficient which is calculated to be 89233.4 kgm^{-4}, in which C_f is the inertia coefficient (Aboelsoud et al. 2013).

2. Permeate side (laminar Flow):

$$\rho(\underline{v}\cdot\nabla)\underline{v}=\nabla\cdot\left[-p\mathbf{I}+\mu\left(\nabla\underline{v}+(\nabla\underline{v})^T\right)-(2/3)\mu(\nabla\cdot\underline{v})\mathbf{I}\right]+\underline{F} \quad (4\text{-}47)$$

Mass balance:

1) Retentate side for species i:

$$\nabla\cdot\underline{j}_i+\rho(\underline{v}\cdot\nabla)w_i=R_i \quad (4\text{-}48)$$

$$\underline{j}_i=-\left(\rho D_\alpha^{eff}\nabla w_i+\rho w_i D_\alpha^{eff}\frac{\nabla M_n}{M_n}\right) \quad (4\text{-}49)$$

In which M_n is the mixture molar mass, R_i terms for each species are from equations 4-5 to 4-8.

On the retentate side dispersion is considered in order to take into account the influence of the packed bed reactor. Longitudinal and transverse dispersion coefficients (D_L^{eff} and D_T^{eff}) for fixed bed reactors were calculated using Eqs. 4-50 to 4-56 (Delgado 2006). The fixed bed porosity ε_p, and tortuosity τ were calculated from

$$\varepsilon_p=1-\frac{\rho_{load}}{\rho_{cat}} \quad (4\text{-}50)$$

and

$$\tau = 1 - p\ln(\varepsilon_p) \tag{4-51}$$

where p is a fitting constant which was equal to 0.77. The porosity was calculated to be 0.32, and the tortuosity was calculated to be 1.88. These values were used in the following

$$\mathrm{Pe} = \mathrm{Re} \cdot \mathrm{Sc} \tag{4-52}$$

$$1/\mathrm{Pe_L} = \varepsilon_p/(\tau \cdot \mathrm{Pe}) + 1/2 \tag{4-53}$$

$$\mathrm{D_L^{eff}} = \mathrm{ud}/\mathrm{Pe_L} \tag{4-54}$$

$$1/\mathrm{Pe_T} = \varepsilon_p/(\tau \cdot \mathrm{Pe}) + 1/12 \tag{4-55}$$

$$\mathrm{D_T^{eff}} = \mathrm{ud}/\mathrm{Pe_T} \tag{4-56}$$

2) Permeate side for species *i*:

$$\nabla \cdot \underline{\mathrm{j}}_\mathrm{i} + \rho(\underline{\mathrm{v}} \cdot \nabla)\mathrm{w_i} = 0 \tag{4-57}$$

$$\underline{\mathrm{j}}_\mathrm{i} = -\left(\rho \mathrm{D}_\alpha \nabla \mathrm{w_i} + \rho \mathrm{w_i} \mathrm{D}_\alpha \frac{\nabla \mathrm{M_n}}{\mathrm{M_n}}\right) \tag{4-58}$$

The diffusion coefficient is calculated using the equation.

$$\mathfrak{D}_{\mathrm{AB}} = 0.0018583\sqrt{\mathrm{T}^3(1/\mathrm{M_A} + 1/\mathrm{M_B})}(1/\mathrm{p}\sigma_{\mathrm{AB}}^2\Omega_{\mathfrak{D},\mathrm{AB}}) \tag{4-59}$$

Where σ_{AB} was obtained from the Lennard-Jones parameters, T is the temperature of the gases, p the pressure and $\Omega_{\mathfrak{D},\mathrm{AB}}$ the collision integral (Bird et al. 2007). A and B refer to hydrogen and nitrogen.

3) Boundary condition at the membrane (hydrogen flux) (Koc et al. 2014):

$$N_{H_2} = \begin{cases} -\gamma \cdot P_{H_2}\left[\sqrt{p_{H_2}^{shell}} - \sqrt{p_{H_2}^{tube}}\right], \text{Retentate} \\ +\gamma \cdot P_{H_2}\left[\sqrt{p_{H_2}^{shell}} - \sqrt{p_{H_2}^{tube}}\right], \text{Permeate} \end{cases} \quad (4\text{-}60)$$

$$P_{H_2} = \frac{6322.7\exp(-15630/(R \cdot T))}{l} \quad (4\text{-}61)$$

where P_{H_2} is the hydrogen permeance with the unit of $Nm^3 \cdot m^{-2} \cdot h^{-1} \cdot bar^{-0.5}$, in order to match with the unit for hydrogen flux, a unit transformation term γ is included.

$$\gamma = \frac{1\ atm/_{298\ K}}{R} \quad (4\text{-}62)$$

Where the numerator stands for normal conditions, and R is the gas constant 8.2× 10^{-5} $[m^3 \cdot atm/(mol \cdot K)]$. Hydrogen flux was defined by Sieverts' law, the positive and the negative terms with the same expression in Eq. 4-60 were defined on the permeate side and the retentate side respectively in order to describe the hydrogen permeation through the membrane. Compared with the previous isothermal model, hydrogen permeance is defined by the Arrhenius equation for temperature-dependence in order to consider the influence of the temperature distribution on hydrogen permeance.

Energy balance:

1) Retentate side:

$$\rho C_p \underline{v} \cdot \nabla T + \nabla \cdot \underline{q} = Q_R \quad (4\text{-}63)$$

$$\underline{q} = -k^{eff} \nabla T \quad (4\text{-}64)$$

Q_R is the heat generated by the reaction, which can be expressed by:

$$Q_R = \sum_{i=1}^{4} r_i \cdot (-\nabla H_i) \quad (4\text{-}65)$$

Same as the mass balance on retentate side, energy balance on retentate side also needs to consider the effect of the catalyst bed. Effective axial and radial thermal conductivity can be expressed by:

Axial:

$$\mathrm{Pe_a} = \frac{\rho U C_p d}{k_a} = \frac{\mathrm{RePr}}{\frac{k_0}{k_f} + \frac{\mathrm{Re^2 Pr^2}}{6(1-\varepsilon_P)\mathrm{Nu}}} \tag{4-66}$$

In which k_a is the effective axial thermal conductivity and $\frac{k_0}{k_f}$ is the stagnant conductivity ratio; Nu can be calculated as (Vortmeyer 1975):

$$\mathrm{Nu} = \frac{h_{fs} d}{k_f} = 1.75 \mathrm{Re}^{0.49} \mathrm{Pr}^{1/3} \tag{4-67}$$

where h_{fs} and k_f are the fluid-solid heat transfer coefficient and fluid thermal conductivity respectively.

Radial (Dixon 2012):

$$\frac{1}{\mathrm{Pe_r}} = \frac{U \rho C_p d}{k_r} = \frac{(2/3)\,\varepsilon_P}{\mathrm{RePr}} + \frac{1}{\mathrm{Pe_r}(\infty)} \tag{4-68}$$

In which k_r is the effective radial thermal conductivity; $\mathrm{Pe_r}(\infty)$ can be calculated by:

$$\mathrm{Pe_r}(\infty) = 8\left[2 - (1 - \frac{2}{N})^2\right] \tag{4-69}$$

2) Permeate side:

$$\rho C_p \underline{v} \cdot \nabla T + \nabla \cdot \underline{q} = 0 \tag{4-70}$$

$$\underline{q} = -k_f \nabla T \tag{4-71}$$

3) Boundary condition at the membrane (Energy flux):

$$q_m = \begin{cases} k_p \cdot \dfrac{(T_{perm} - T_{ret})}{l} + N_{H_2} \cdot (\tilde{H}_{perm} - \tilde{H}_{ret}), & \text{Retentate side} \\ k_p \cdot \dfrac{(T_{ret} - T_{perm})}{l} + N_{H_2} \cdot (\tilde{H}_{ret} - \tilde{H}_{perm}), & \text{Permeate side} \end{cases} \quad (4\text{-}72)$$

which includes the conduction through the palladium membrane (first term) and the enthalpy that hydrogen carries across the membrane (second term).

Hydrogen yield and recovery were defined by the following equations:

$$\text{Yield} = \frac{\text{Total } H_2 \text{ generated}}{5 \cdot \text{ethanol feed}} \quad (4\text{-}73)$$

$$\text{Recovery} = \frac{H_2 \text{ permeated}}{\text{Total } H_2 \text{ generated}} \quad (4\text{-}74)$$

The overall mass balance was checked for closure, by looking at the mass flows for several cases over the inlet and outlet surfaces. These showed that the error in the mass balance was approximately 0.008, defined by (Total mass inflow-Total mass outflow)/Total mass inflow. In other words, the mass balance error was approximately 0.8%. The average total inflow was 1.68×10^{-4} kg/s.

4.3 Membrane characterization

The membrane module was first flushed with He and the retentate pressure increased by 1 bar. Figure 4.5 shows the permeation and He leak tests of the membrane at different temperatures. The temperature (Figure 4) of the reactor was increased to 350°C at 1°C per minute under He. A leak test performed on the module showed a He flux of 0.2 sccm/bar. Hydrogen was fed to the system for 20 hours displaying a H_2 permeance of 11 $Nm^3m^{-2}h^{-1}bar^{-0.5}$. The temperature of the module was then increased to 450°C and the H_2 permeance was measured continuously for 20 hours. The membrane's permeance increased gradually reaching a steady value of 21 $Nm^3m^{-2}h^{-1}bar^{-0.5}$, or about 50% higher than at 350 °C. The He leak at this temperature increased to 1

sccm/bar. In order to test the leakage, He was introduced to the system instead of pure H_2 from 44- 46 hours as shown in Figure 4.5. The membrane had estimated ideal H_2/He selectivities of 10,800 and 1,139 at temperatures of 350 ^oC and 450 ^oC, respectively. Afterwards, the temperature was increased to 600 ^oC for 2 hours under pure H_2 in order to activate the catalyst, as specified by the provider. The membrane showed a good thermal stability since, after activation, no He leak was found on the membrane at a pressure difference of 1 bar, while the H_2 flux remained stable. This phenomenon as described by Mardilovich et al. (2015) could be the result of Au acting as a patch paste on the membrane defects.

The H_2 permeance of the membrane was tested when its composition and thickness was 6.9 µm Pd/ 0.2 µm Au/ 3.2 µm Pd; its permeance was 80 $Nm^3m^{-2}h^{-1}bar^{-0.5}$ at 450^oC. There was a 70% reduction in H_2 permeance after the membrane was replated. The decline in H_2 permeance occurred as the thickness of the membrane was increased, inferring higher resistance to the diffusion of protons through the Pd lattice. Furthermore, there is an overall increase in the gold content of the membrane, which can significantly influence the solubility of H_2 in the active sites of the membrane, as reported by Sonwane et al. (2006). Nonetheless, the H_2 permeance of the membrane is in agreement with the values presented in the literature for Pd and Pd/Au membranes (Mardilovich et al. 2015; Guazzone et al. 2012; Ayturk et al. 2009) and with 20 µm free standing foils, which have a theoretical permeance of 15 and 23 $Nm^3m^{-2}h^{-1}bar^{-0.5}$ at 350 ^oC and 450 ^oC, respectively. Notice that the resistance of the support is not taken into consideration for the theoretical calculation of the free standing foils, suggesting that the selective layer of the membrane presented in this work has enhanced properties and/or the resistance of the support is negligible.

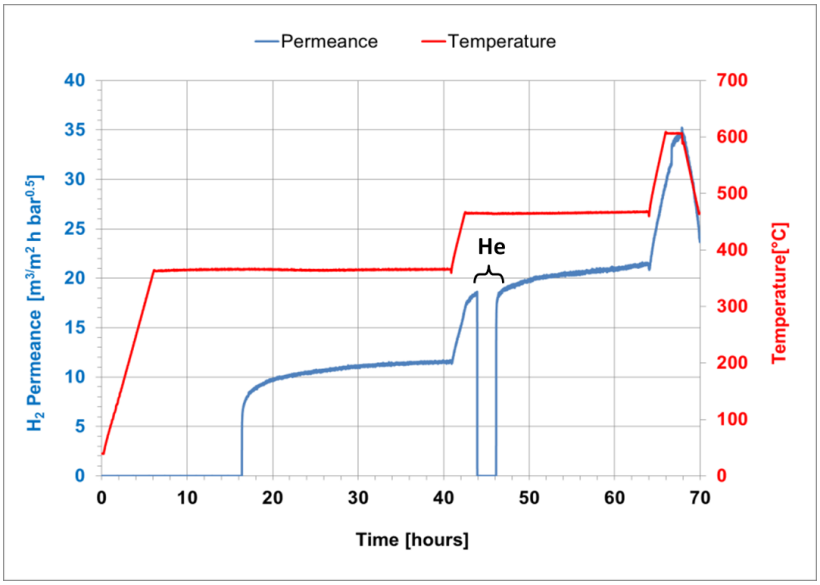

Fig 4.5 Hydrogen permeance at different times and temperatures

4.4 Performance of the 1-D and 2-D isothermal simulations

The 1-D and 2-D simulation models were compared to the experiments carried out in the large-scale catalytic membrane reactor presented in this work. In Figure 4.6 only the experimental results for the H_2 mole fraction at the retentate were compared against those found through the simulation models, in order to avoid unnecessary and repetitive information; nonetheless, both simulations predicted accurately the tendency of the reaction. The result of the 2-D model shows a higher accuracy than that of the 1-D simulation. While the 1-D model showed 85% accuracy, the 2-D improved its performance to 91%. The 2-D model takes into consideration the effect of radial mass transfer limitations as well as the features of porous media, which can affect the performance of CMRs.

The discrepancies found between the simulation results and the experiments could be triggered by four main effects or a combination of them:

i) The permeance of the membrane is assumed to be constant under reacting conditions. Experimentally, the permeance of the membrane has been shown to be affected by

components such as CO and steam (Li et al. 2000), which are unevenly distributed along the reactor.

ii) Carbon deposition in the catalytic bed is neglected in the simulation models. The possibility of coking can lead to a decrease in the activity of the catalyst as well as in the permeance of the membrane. Nonetheless, operating at mild temperatures (350-450^{o}C) significantly reduces the possibility of coking for MSR and WGS reactions (Rostrup-Nielsen et al. 1993).

iii) Potential temperature gradients along the catalytic bed are neglected. The CMR used in this study had a length of 39.4 in. and its temperature was supplied by a furnace (Watlow 1.6 kW) with a length of 31.5 in. Although the connections and auxiliary equipment were thermally insulated to avoid cold spots, temperature gradients were observed, as reported previously by Catalano et al. (2012).

iv) The simulation model inputs are based on lab-scale parameters. The current CMR study was performed on a large-scale bench, which can induce changes in the operational and modelling properties of the system (Caygill et al. 2006).

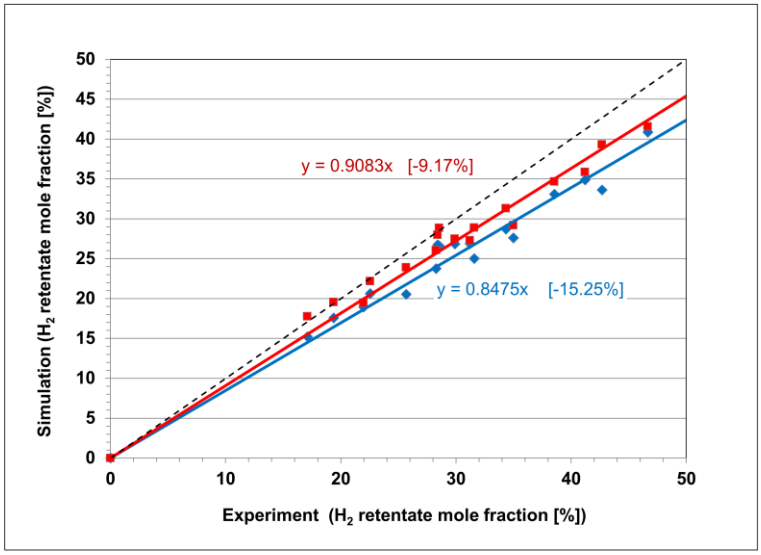

Fig 4.6 Comparison of the simulation and experimental results found in the present study: 1D Simulation-Experiment (◆), 1D Simulation-Experiment trendline (—); 2D Simulation-Experiment (■), 2D Simulatiom-Experiment trendline (—)

4.5 Catalytic membrane reactor performance (Isothermal)

The CMR module was tested continuously for 300 hours, generating H_2 with a purity of 99.9%. The conversion of ethanol was 100% for every condition, in agreement with the results reported by Kumar et al. (2014), where it was shown that noble metal catalysts achieve 100% ethanol conversion with a selectivity near to 99% depending on the type of support and loading metal. A hydrogen flux of 0.38 grams of H_2 per hour was achieved by the module. The following subsections describe in detail the performance of the CMR when the operational variables were modified.

4.5.1 Effect of space velocity

At first, the effect of space velocity in the performance of the CMR for ESR was explored at 450^{o}C and a S/E ratio of 3. Figure 6 shows the mole fraction on a dry basis at the retentate outlet as a function of the space velocity for the experiments performed (scattered points), the 1-D model (solid line) and the 2-D CFD simulation (dashed line). Notice that one experimental point was outside range and therefore it was considered an error; Figure 6 neglects this point in the graph. It can be observed that in most cases H_2 appears to grow as the space velocity increases, this is the result of decreasing the H_2 contact time with the membrane surface, which causes an accumulation of H_2 at the retentate side. Although at higher space velocity the membrane recovery decreases by the lack of contact time with the membrane, more H_2 is observed at the permeate side. This effect occurs since as the space velocity increases, more reactant is fed to the reactor, leading to an overall higher H_2 production.

The mole fraction of methane in the retentate appears to have a slight decrease at higher velocities for the 2-D simulation and for the experimental results. The 1-D model showed a steady performance where CH_4 appeared constant at all velocities. In CMRs, the process of MSR is expected to proceed further when operating at reduced feed flow rates, assuming that the reaction is not kinetically limited but rather controlled by the permeation rate of the membrane. This phenomenon has been previously reported in the literature (Barbieri et al. 1997; Ayturk et al. 2009), where methane conversion reduces as the space velocity is increased.

In Figure 4.7, CH_4 appears to decrease rather than increase, indicating that the reaction is being hindered by the presence of H_2 in the reaction zone. In other words, higher velocities influence the rate of H_2 removal more strongly than the reaction rate. A similar performance is observed with carbon dioxide, where it appears to have a slight decrease towards higher velocities. A reduction in CO_2 can be caused by a reduced conversion of ethanol and/or methane. As mentioned before, the total conversion of ethanol was achieved and since CH_4 is reduced, it is suggested that the lower CH_4 conversions caused the reduction in CO_2 at higher flow rates.

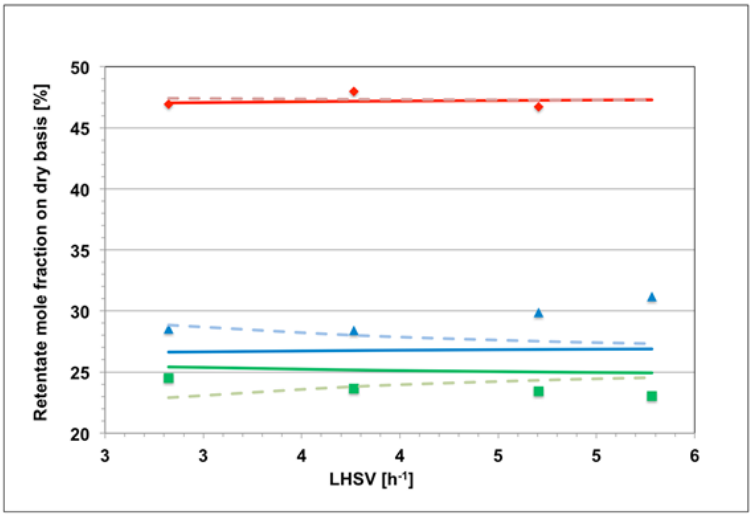

Fig 4.7 Retentate composition at different LHSV and 450°C, 3 bar and a S/E = 3: H_2 Experiment (▲), H_2 1D Simulation (—), H_2 2D Simulation (– –); CH_4 Experiment (◆), CH_4 1D Simulation (—), CH_4 2D Simulation (– –); CO_2 Experiment (■), CO_2 1D Simulation (—), CO_2 2D Simulation (– –)

4.5.2 Effect of pressure and steam content

After the analysis of the space velocity, the liquid feed flow rate was fixed at 2.48 cm^3/min or a LHSV of 3.77 h^{-1}. The CMR module was tested at different pressures and S/E ratios as shown in Figure 4.8. At first, the S/E was fixed to 3 and the pressure was varied from 2 to 10 bar. It can be observed that as the operating pressure increases, the H_2 mole fraction of retentate decreases implying that the H_2 removal through the membrane is intensified as the driving force for

permeation is increased. Moreover, higher pressures enlarged the mole fraction of CH_4 at the retentate. This effect does not indicate that the content of CH_4 increases, but rather that, due to the removal of H_2, the mole fraction of methane appears higher. This hypothesis is valid in all conditions, since no ethanol was detected at the retentate outlet. The same effect appears to occur for CO_2, where, as the pressure increases, the CO_2 mole fraction of the retentate increases. In conventional reactors, ESR (Mathure et al. 2007) and MSR (Ayturk et al. 2009) show a negative response to pressure as it is thermodynamically unfavorable, as described by Le Chatelier's principle. Nonetheless, the removal of H_2 from the reaction zone changes the composition of the reaction zone, improving the overall performance of the reactions. The effect of pressure at different S/E ratios did not seem to influence the aforementioned trend. Indeed, as pressure increased the H_2 mole fraction of the retentate decreased, CH_4 increased and CO_2 increased.

An increase in the driving force of H_2 transport certainly has an important contribution in the performance of CMR technology. Based on simulation data, Figure 4.9 shows how much H_2 is generated in CMRs when compared to traditional packed bed reactors (PBR) at different membrane permeances and pressures and thus the term (σ) was used to describe this effect (Eq. 4-75). A similar study has been done by Helmi et al. (2016) in which the benefit of fluidized bed membrane reactor (FBMR) compare with traditional fluidized bed reactor (FBR) was observed by analyzing the improvement of CO conversion in WGS reaction operating in the two reactors.

$$\sigma[\%] = [\left(\mathrm{F}_{\mathrm{H2}}^{\mathrm{per}} + \mathrm{F}_{\mathrm{H2}}^{\mathrm{ret}}\right)_{\mathrm{CMR}} - (\mathrm{F}_{\mathrm{H2}}^{\mathrm{ret}})_{\mathrm{PBR}}]/(\mathrm{F}_{\mathrm{H2}}^{\mathrm{ret}})_{\mathrm{PBR}} \cdot 100 \qquad (4\text{-}75)$$

The effectiveness of CMR technology in generating H_2 directly depends on the total amount of H_2 removed from the reaction zone. One method to improve this rate of removal is by increasing the driving force for H_2 transport or the H_2 partial pressure difference between the retentate and the permeate. Therefore, higher retentate pressures significantly improved the generation of H_2 (Figure 4.9). In Figure 4.9, an increase in pressure not only made the CMR more efficient, but simultaneously reduced the performance of conventional PBRs. Therefore, the term (σ) appears to increase significantly as pressure was increased.

Another factor that influences the rate of H_2 removal from the reactor is the permeance of the membrane. Low permeances in CMRs imply analogous features with conventional PBRs; however, as the permeance increases, the generation of H_2 is enhanced. This boost, shown in Figure 4.9, reaches a plateau which occurs when the permeance of the membrane is hindered by a low driving force for H_2 transport. In other words, as more hydrogen is depleted from the retentate and collected on the permeate side, the hydrogen partial pressure on each side becomes equal, making the driving force close or equal to zero. After reaching this condition, an increase in H_2 permeance does not reflect the effect of process intensification. This phenomenon can be confirmed when analyzing the point where the plateau is reached. The plateau appears at higher permeance values when the operating pressure is increased (Figure 4.9); this effect will continue until the driving force becomes limited by the kinetics of the reaction.

Steam showed an enhancing effect on the production of H_2 and the reaction overall. As the S/E ratio increased, the H_2 mole fraction at the retentate increased as shown in Figure 4.8. This outcome indicates that the rate of H_2 removal is the limiting process within the CMR, and that an increase in pressure will generate more H_2. On the other hand, the mole fractions of CH_4 and CO_2 in the retentate decreased and increased, respectively, as the S/E increased. This trend indicates that the conversion of CH_4 in the process improves in the presence of higher steam content. Although the presence of steam appears to be beneficial to the overall production of H_2, Li et al. (2000) reported that steam significantly affects the permeability of Pd membranes as it has shown strong adsorption ability on Pd surfaces. This suggests that there is a tradeoff between operating at high S/E ratios to improve the kinetics of the reaction while maintaining high permeability properties in the membrane.

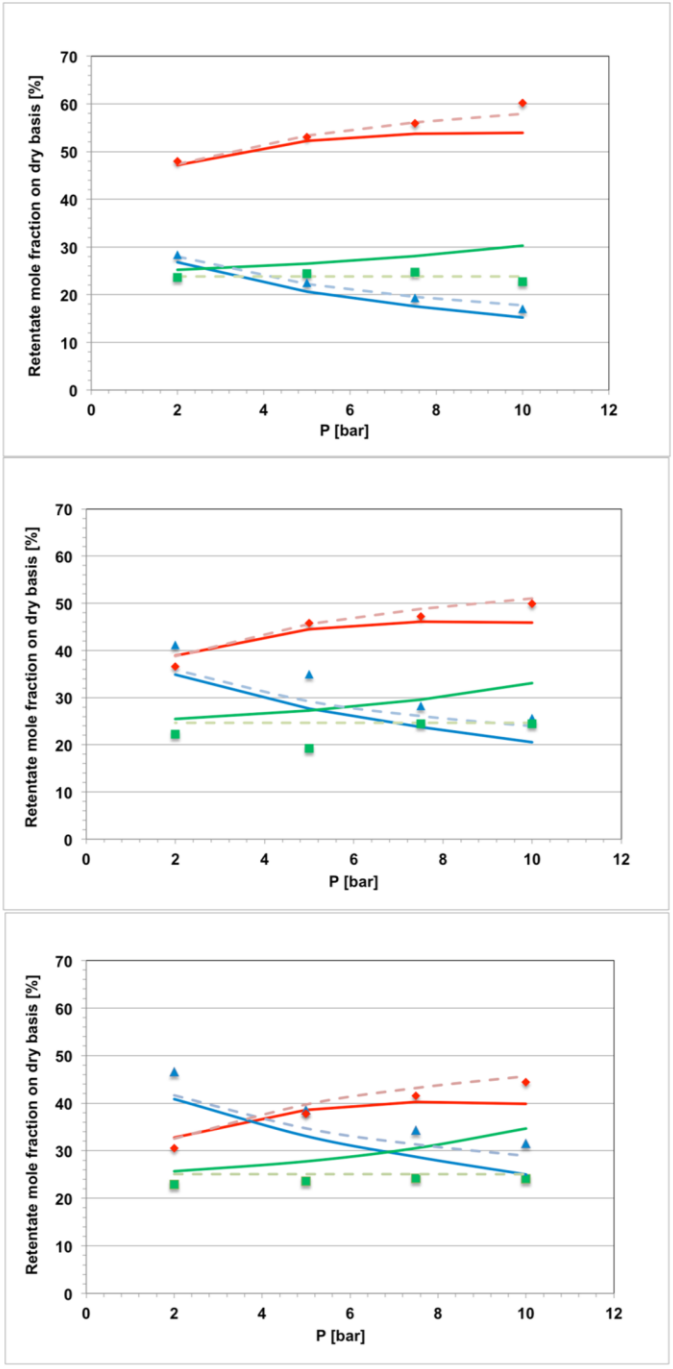

Fig 4.8 Composition of the retentate at different pressures at 450°C, LHSV=3.77 $h^{-1}$and a) S/E= 3, b) S/E= 5 and c) S/E= 7: H_2 Experiment (▲), H_2 1D Simulation (—), H_2 2D Simulation (– –); CH_4 Experiment (◆), CH_4 1D Simulation (—), CH_4 2D Simulation (– –); CO_2 Experiment (■), CO_2 1D Simulation (—), CO_2 2D Simulation (– –)

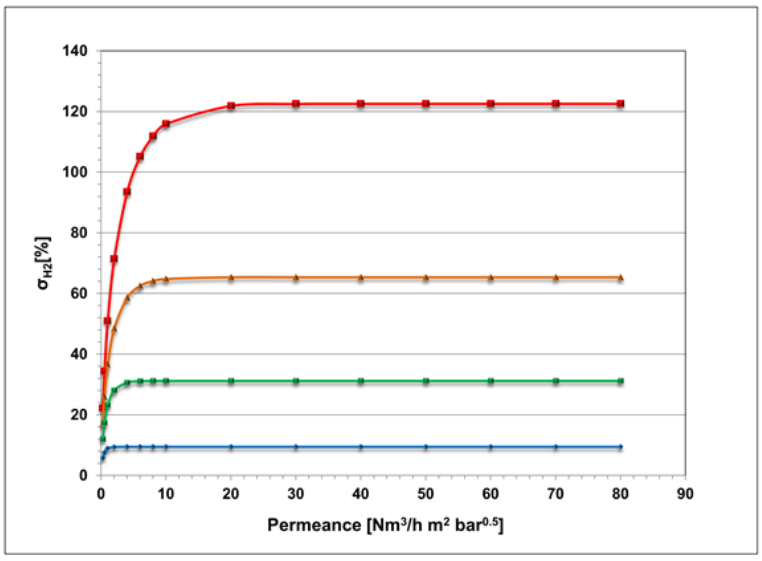

Fig 4.9 Hydrogen production improvement at different membrane permeances and retentate pressures: 11bar (—), 8.5 bar (—), 6 bar (—), 3 bar (—)

4.5.3 Effect of temperature

The highly endothermic characteristic of ESR indicates that the process is thermodynamically favored by high temperatures. In CMR technology, temperature is a critical factor since it strongly relates to the H-diffusion through the Pd lattice and the activation energy for solution. To analyze the influence of temperature, the experiment was carried out under a fixed LHSV of 3.77 h^{-1}, a S/E ratio of 5 and a retentate pressure of 6 bar. The temperature was studied in the range of 350°C - 500°C. As shown in Figure 4.10, as the temperature increased, the H_2 mole fraction in the retentate side increased, as a consequence of different elements. The first one relates to an increase in the kinetic properties of the catalyst, which induces higher CH_4 conversions, as previously shown in the literature (Gallucci et al. 2008). Another factor is the membrane's H_2 permeance, which is enhanced by high temperatures (Eq. 4-76). Nonetheless, the generation of H_2 overcame the rate of removal and therefore an accumulation of H_2 is observed at the retentate.

$$Q = Q_0 e^{-E_p/(R \cdot T)} \quad (4\text{-}76)$$

In which Q_0 is the membrane permeability constant $(m^3 \mu m/[m^2 h\ atm^{0.5}])$, E_p represents activation energy of H_2 diffusion (kJ/mol) and R is the gas constant.

It is important to mention that the trend was accurately depicted by the 1-D and 2-D simulation models; but the experimental H_2 mole fraction appeared to be underestimated in Figure 4.10. This difference in the performance of the simulation and experimental results could be caused by the inhibition of the H_2 permeance, caused by the presence of components such as CO, steam, CO_2 and ethanol (Boon et al. 2015). The simulation model did not consider variances in H_2 permeance; in other words, the model assumes that all gas species, excluding H_2, act as inert components.

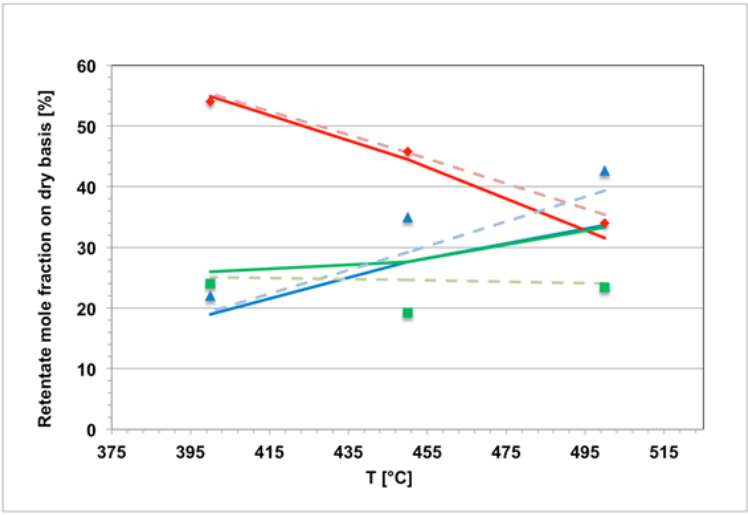

Fig 4.10 Composition of the retentate at different temperatures, a retentate pressure of 6 bar and S/E=5: H_2 Experiment (▲), H_2 1D Simulation (—), H_2 2D Simulation (– –); CH_4 Experiment (◆), CH_4 1D Simulation (—), CH_4 2D Simulation (– –); CO_2 Experiment (■), CO_2 1D Simulation (—), CO_2 2D Simulation (– –)

The mole fraction of methane decreased as temperature increased since the methane steam reforming reactions (Eqs.3-4) are enhanced with temperature. The effect of temperature on methane during ESR (Eq.1-4) was studied in Figure 4.11, where the molar flow rate of CH_4 is computed at different membrane reactor lengths. It can be seen, at first, that CH_4 is generated early in the catalytic bed by breaking down ethanol; once ethanol is completely consumed, the

process of MSR limits the generation of H_2. In Figure 4.11, the conversion of CH_4 (X_{CH4}) was defined as:

$$X_{CH4}[\%] = (F_{CH4}^{max} - F_{CH4}^{ret})/F_{CH4}^{max} \cdot 100 \quad (4\text{-}77)$$

Where F_{CH4}^{max} and F_{CH4}^{ret} are the maximum CH_4 molar flow rate identified and the CH_4 molar flow rate at the outlet of the retentate, respectively. Figure 4.11 shows that the conversion of the generated methane, during the ESR process, improves as temperature increases.

Methane steam reforming was studied in simulation under "MSR conditions only" (CH_4 and steam) and labelled as MSR-CMR and "ESR conditions" and labelled ESR-CMR. The purpose was to compare the performance of the MSR-CMR and the ESR-CMR. Notice that the maximum CH_4 molar flow rate identified in the ESR-CMR was used as the feed stream for the MSR-CMR and MSR-CMR which agrees with the result previously reported by Medrano et al. (2016). Table 4-2 shows the theoretical methane conversion of the ESR-CMR and MSR-CMR. Under MSR conditions, the CH_4 conversion is higher than under ESR conditions. The reason is that the pseudo-composition formed in the reaction zone is different in both cases. For instance, in ESR, when ethanol reacts, it produces CH_4, CO and H_2; at this moment, CO immediately reacts in the WGS process (Eq. 2) to generate more H_2 and CO_2. Meanwhile, CH_4 reacts, at a slower rate, in the MSR process (Eqs. 3-4); nonetheless, the presence of CO, CO_2 generated from the other reactions, thermodynamically inhibits the conversion of CH_4. In contrast, under MSR conditions only, when CH_4 starts reacting, no products are present and that the generated compounds are in stoichiometric balance, allowing higher CH_4 conversions. It is important to mention that the presence of a H_2 selective membrane in the reactor improves the generation of H_2 for ESR; however, when compared to MSR, the effect of "process intensification" is reduced.

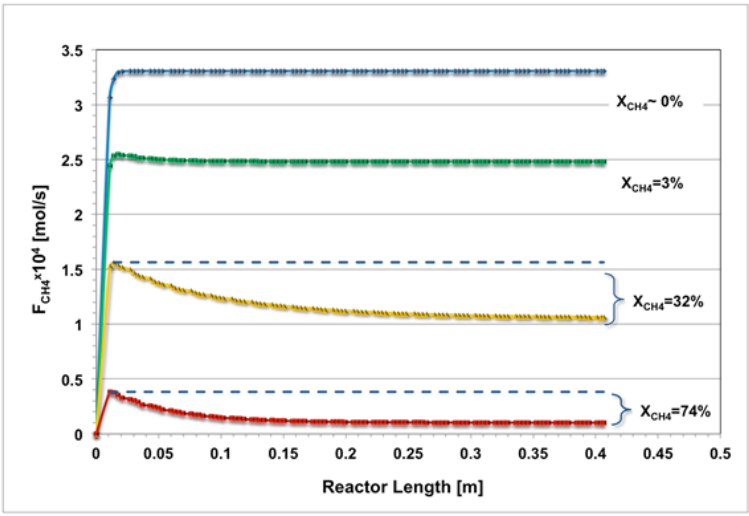

Fig 4.11 Methane molar flow rate along the length of the membrane at different temperatures, a retentate pressure of 3 bar and S/E=5: 450 °C (—), 525°C (—), 600 °C (—), 700 °C (—)

Table 4-2. Comparison of CH_4 conversion under ESR and MSR conditions

Temperature (°C)	X_{CH4} in ESR-CMR (%)	X_{CH4} in MSR-CMR(%)
450	0	28
525	3	60
600	32	95
700	74	100

For the case of CO_2, Figure 4.10 shows a stable performance as a function of temperature, possibly due to the integrated effect of WGS reaction and MSR. In Figure 4.10, CO_2 appears to deviate more experimentally, but this data has an estimated average standard deviation of 0.4. At different temperatures, CO_2 shows a rather constant mole fraction, as previously reported in the literature (Murmura et al. 2015; Papadias et al. 2010; V. Palma 2012; A. B. F. Gallucci 2007). The 2-D model shows this stable CO_2 trend and also it shows a higher accuracy with respect to the experimental points than the 1-D model, possibly due to radial mass transfer effects. At

high temperatures, the reaction rate of MSR increases, but the activity of WGS decreases. In contrast, at low temperatures, the WGS reaction improves while the MSR deteriorates, as reported by Sahoo et al. (2007) and Murmura et al. (2015). It is important to mention that CO was not detected in the present work; nonetheless, to further explain the phenomenon observed in Figure 4.10, the tradeoff between MSR/WGS during the process of ESR in CMRs is presented in Figure 4.12. The selectivity of CO_2/CO, defined in Eq. 4-78, was computed at different temperatures and a retentate pressure of 3 bar.

$$S_{CO2/CO} = F_{CO2}^{ret}/F_{co}^{ret} \quad (4\text{-}78)$$

At high temperatures (Figure 4.12), the generation of CO is expected to rise, as WGS is a moderately exothermic reaction, which is repressed at high temperatures (>450^{o}C). As the temperature decreases, the selectivity towards CO_2 increases exponentially, since WGS becomes more active. The maximum CO_2/CO selectivity is presented at a temperature of 320^{o}C; lower temperatures, showed a sharp decrease in selectivity. The reduction in selectivity at the colder temperatures can be attributed to i) the reduction in permeance of the membrane and ii) a slower ESR reaction rate. The reaction of ethanol is expected to proceed later in the catalytic bed, as the ESR reaction rate is reduced; consequently, the process of WGS will have lower residence times for the reaction to proceed. This reduction in residence time potentially affects the total CO concentration. Furthermore, as the permeance of the membrane decreases with reduced temperatures, it is expected to have a higher H_2 concentration in the reaction zone. The presence of H_2 allows the system to reach thermodynamic equilibrium faster, inhibiting the WGS reaction and thus resulting in higher CO levels.

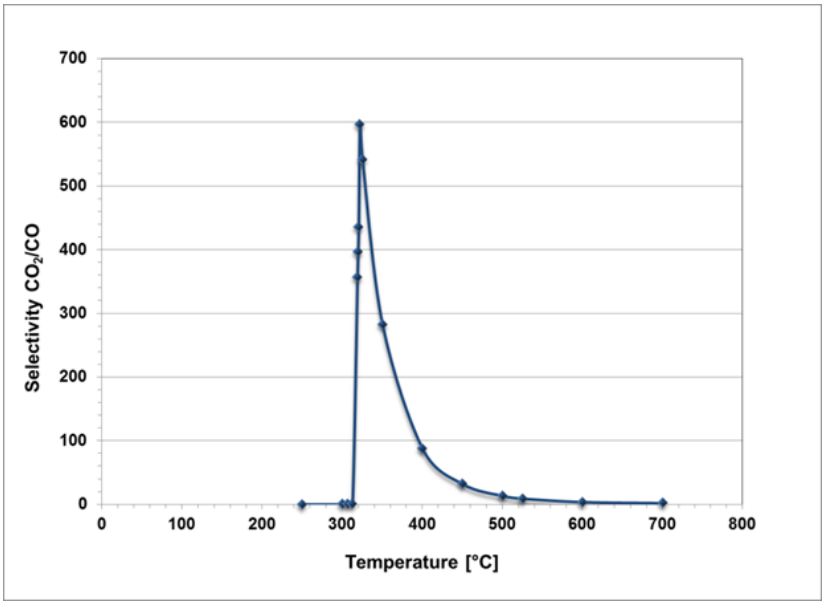

Figure 4.12 Selectivity of CO_2/CO of the Ni-based reforming catalyst under ESR-CMR conditions

4.6 Non-isothermal result analysis

The non-isothermal behavior was included into the existing model for the comparison with the previous study. A temperature gradient was observed as expected, and a “cold spot” was shown adjacent to the membrane. The study of reaction rate was introduced and since the process reaches equilibrium very soon after the reactants enter the reactor, different inflow rates and counter-current sweep gas flow were discussed in order to fully use the reactor length and membrane surface area.

4.6.1 Hydrogen mole fraction distribution

The process was simulated under the previous experimental conditions, where the sweep gas helium was introduced into the tube side with the same flow direction as the reactant inlet on the shell side. To ensure high ethanol conversion, reactants with excess steam were fed into the system. Hydrogen distribution from the simulation is shown in Figure 4.13. All the reactions took place immediately as the reactants were fed to the system, in order to clearly observe the performance of the reactor, only 2/3 of the whole reactor geometry is shown in the following figure for concentration distribution and in all the temperature distribution figures. Shortly

after the reactants were fed to the system, hydrogen was generated and an accumulation can be seen on the retentate side, then the hydrogen mole fraction decreases due to the hydrogen depletion by the membrane, and finally reaches an equilibrium with the permeate side as the driving force drops to zero, as the partial pressure decreases on the retentate side and increases on permeate side. For the co-current sweep gas model, since at the beginning of the reactor, the hydrogen partial pressure on the permeate side is zero and the reactions start immediately after entering the reactor, indeed, it is useful to have the membrane from the beginning of the reactor. However, as the process reaches equilibrium, which is not far from the inlet in this case, most of the membrane surface is not improving the reactor performance, which leads to a waste of the materials. Thus different reactant inflow rates were also studied in order to fully utilize the reactor capacity.

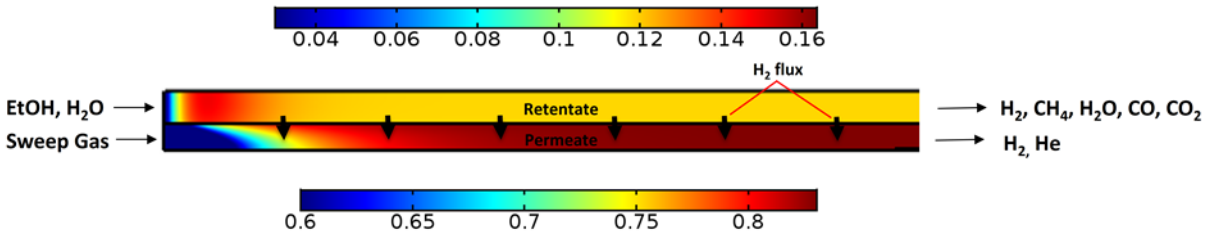

Fig 4.13 Hydrogen mole fraction profile in the co-current reactor at LHSV=3.77h^{-1}, P_{ret} =6 bar, S/E=5 and T_{in}=723K on both permeate and retentate side.

The sweep gas hydrogen mole fraction increases from zero to approximately 0.85. The sweep gas is necessary to maintain a low enough hydrogen partial pressure on the permeate side to prevent back-diffusion of hydrogen into the retentate downstream as the partial pressure of hydrogen on the retentate side decreased. An alternative would be to pull a vacuum on the permeate side to remove the permeated hydrogen, however that option was not pursued in this work.

At higher reactant inflow rate, the membrane reactor is used more effectively as the equilibrium between the two sides of the membrane is now achieved further downstream into the reactor, as shown in Figure 4.14. The hydrogen partial pressure shown in the figure is the product of reactor pressure and the hydrogen mole fraction.

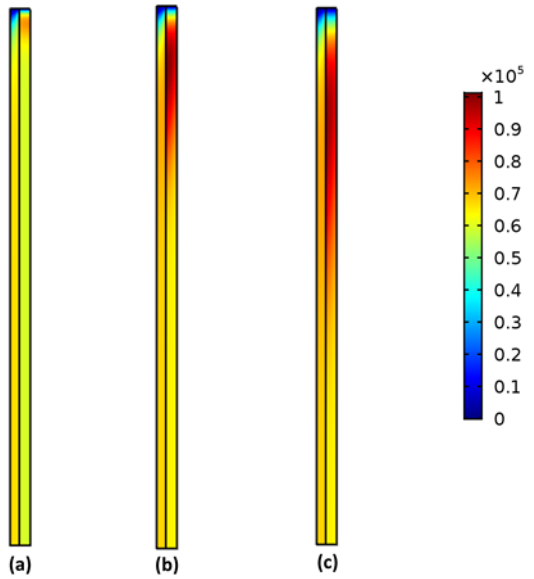

Fig 4.14. Hydrogen partial pressure (Pa) profile on permeate side (left) and retentate side (right) of the reactor at P_{ret} =6 bar, S/E=5 and T_{in}=723K with (a) LHSV = 3.77 h^{-1} (b) LHSV = 18.85 h^{-1} (c) LHSV = 37.7 h^{-1}

The influence of increasing the inflow rate can also be seen from the study of the individual reaction rates. At the original experimental conditions, the reaction rates at the membrane surface and next to the reactor shell are shown in Figure 4.15a. As the reactants were fed to the reactor, the decomposition of ethanol took place immediately, followed by methane steam reforming and water gas shift, which uses the generated methane and CO. All the reactions were conducted very rapidly and reached equilibrium for the rest of the reactor. Furthermore, a reverse methane steam reforming process near the reactor entrance is noticed from the figure due to a relatively local low temperature. From the figure, the generation and depletion process of hydrogen is visualized. Notice that under all the operating conditions studied in this manuscript, full conversion of ethanol is achieved, and the overall hydrogen production depends on the performance of the methane steam reforming and water gas shift reactions.

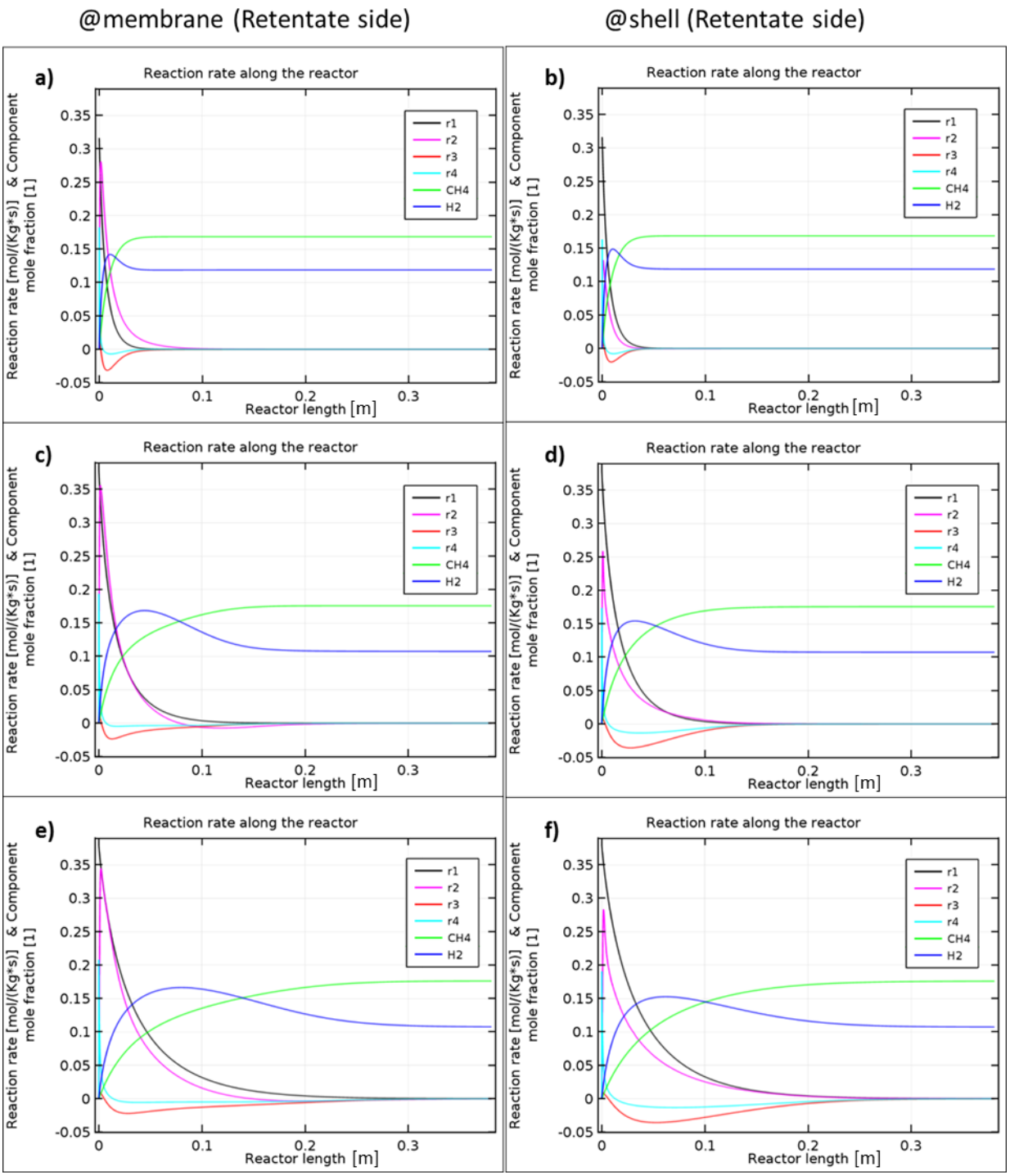

Fig 4.15 Reaction rate (r1:ESR, r2:WGS, r3&r4:MSR) adjacent to the membrane and adjacent to the shell at the experimental condition P_{ret} =6 bar, S/E=5 and T_{in}=723K , a,b at LHSV = 3.77h^{-1}, c,d at LHSV = 18.85 h^{-1}, e,f at LHSV = 37.7 h^{-1}

As the inflow rate increases, the reactions are taking place further axially before reaching equilibrium (Fig 4.15), and the reactor is used more efficiently. Although the negative reaction rate of the two methane steam reforming reactions r_3 and r_4 still can be seen, and a considerable methane slip is still shown due to the low temperature.

Table 4-3. Outlet composition, yield and recovery under co-current sweep gas flow pattern.

LHSV (h^{-1})	C_2H_5OH	CH_4	H_2	CO_2	CO	H_2O	Yield (%)	Recovery (%)
3.77	≈ 0	0.170	0.111	0.0867	0.00197	0.630	15.4	4.530
18.85	8.06E-09	0.176	0.107	0.0988	0.00222	0.616	16.0	0.968
37.7	4.36E-05	0.176	0.108	0.0994	0.00223	0.615	16.1	0.465

From Table 4-3 we can see that ethanol is being completely consumed, also the hydrogen yield increases as the flow rate increases, not by much, but since the yield is defined as the H_2 produced/ maximum H_2 that can be produced from the ethanol feed and the ethanol feed is higher at higher flow-rate, the overall hydrogen production is much higher at higher flow rate. Hydrogen recovery is decreasing on the other hand, as the retentate pressure condition is low and the equilibrium is formed; if higher pressure is used, more hydrogen should be seen on the permeate side.

4.6.2 Temperature distribution

Due to the endothermic property of the reactions, the flow temperature decreases by around 25 K shortly after entering the reactor, and recovers as the reactions reach equilibrium, mainly due to the heat provided by the oven to the system. As shown in Figure 4.16, a “cold-spot” was formed adjacent to the membrane surface. For membrane reactors, as one of the products hydrogen was depleted from the retentate side, higher reactant conversion is achieved, which leads to a more severe temperature reduction. The existence of a relatively large “cold spot” is not ideal for the endothermic steam reforming process.

The effect of this “cold spot” can also be seen from the aforementioned reaction rate study (Figure 4.15). For this highly endothermic process, some reverse reactions might be able to proceed when the temperature is not high enough. In this case, methane steam reforming

reactions experienced a negative reaction rate in the reactor. At experimental operating conditions, this phenomenon is more obvious at the “cold spot” adjacent to the membrane compared to the area adjacent to the reactor shell, where the temperature is relatively higher as it is closer to the oven heat source and convection heat transfer is the dominant heat transfer method inside the reactor. The concentration polarization effect can also be seen from the reaction rate plot. Lower hydrogen mole fraction is seen adjacent to the membrane, and as a consequence, reaction equilibrium is shifted to the product side. However, as the reactant inflow rate increases, concentration polarization is less recognizable. Additionally, the reaction rate of the water gas shift reaction at the shell is lower than at the membrane, thus more CO exists in the system which is detrimental to the equilibrium, and the reverse reaction is more noticeable adjacent to the shell. The radial reaction rate gradient also decreases as the inflow rate increases. At higher inflow rates, the “cold spot” spreads out along the reactor, but at a higher minimum temperature, since the reactions are taking place further along the tube.

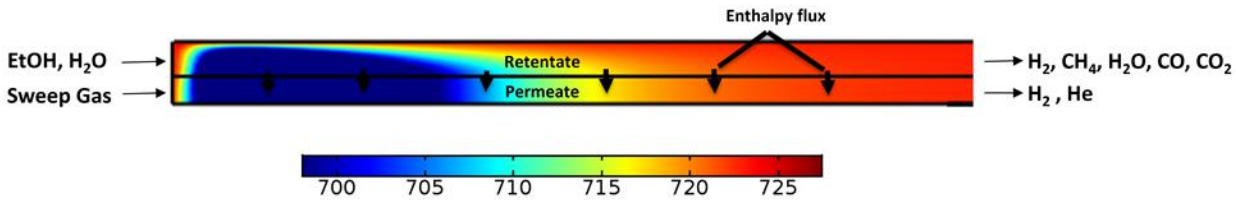

Fig 4.16 Co-current temperature distribution in the reactor at LHSV=3.77h^{-1}, P_{ret} =6 bar, S/E=5 and T_{in}=723K on both permeate and retentate side.

4.6.3 Counter-current sweep gas

In order to further increase the hydrogen production rate and membrane usage, the case of counter-current sweep gas was studied. This allows the driving force to be distributed more evenly throughout the whole reactor. As shown in Figure 4.17, similar hydrogen mole fractions to the co-current reactor are observed and a lower hydrogen mole fraction in the main part of the reactor is achieved by switching to counter-current sweep gas.

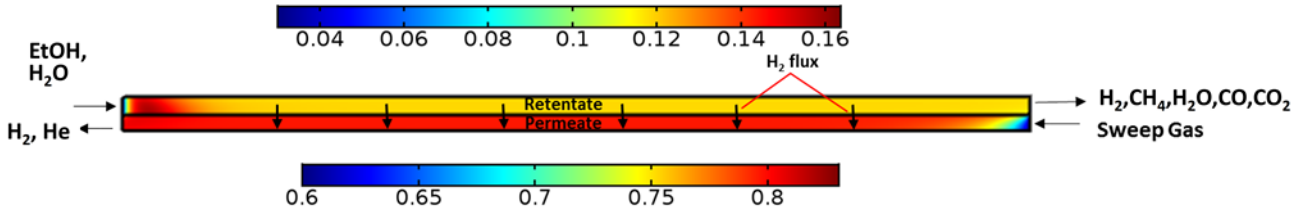

Fig 4.17 Hydrogen mole fraction profile in the counter-current reactor at LHSV=3.77h^{-1}, P_{ret} =6 bar, S/E=5 and T_{in}=723K on both permeate and retentate side.

A lower hydrogen mole fraction can also be seen from the 1-D plot of reaction rate and mole fraction (Figure 4.18). At the retentate outlet, the counter-current system shows a further decrease of hydrogen, since a sweep gas with zero content of hydrogen is introduced at that end of the reactor which breaks the previously reached equilibrium by increasing the driving force. However, the effect is not obvious adjacent to the shell, since the hydrogen transport is limited radially. Counter-current flow is also beneficial to the individual reactions, as the reactions that previously reached equilibrium would start having positive reaction rate again. This effect is beneficial for the efficient usage of the reactor length as well as the hydrogen production.

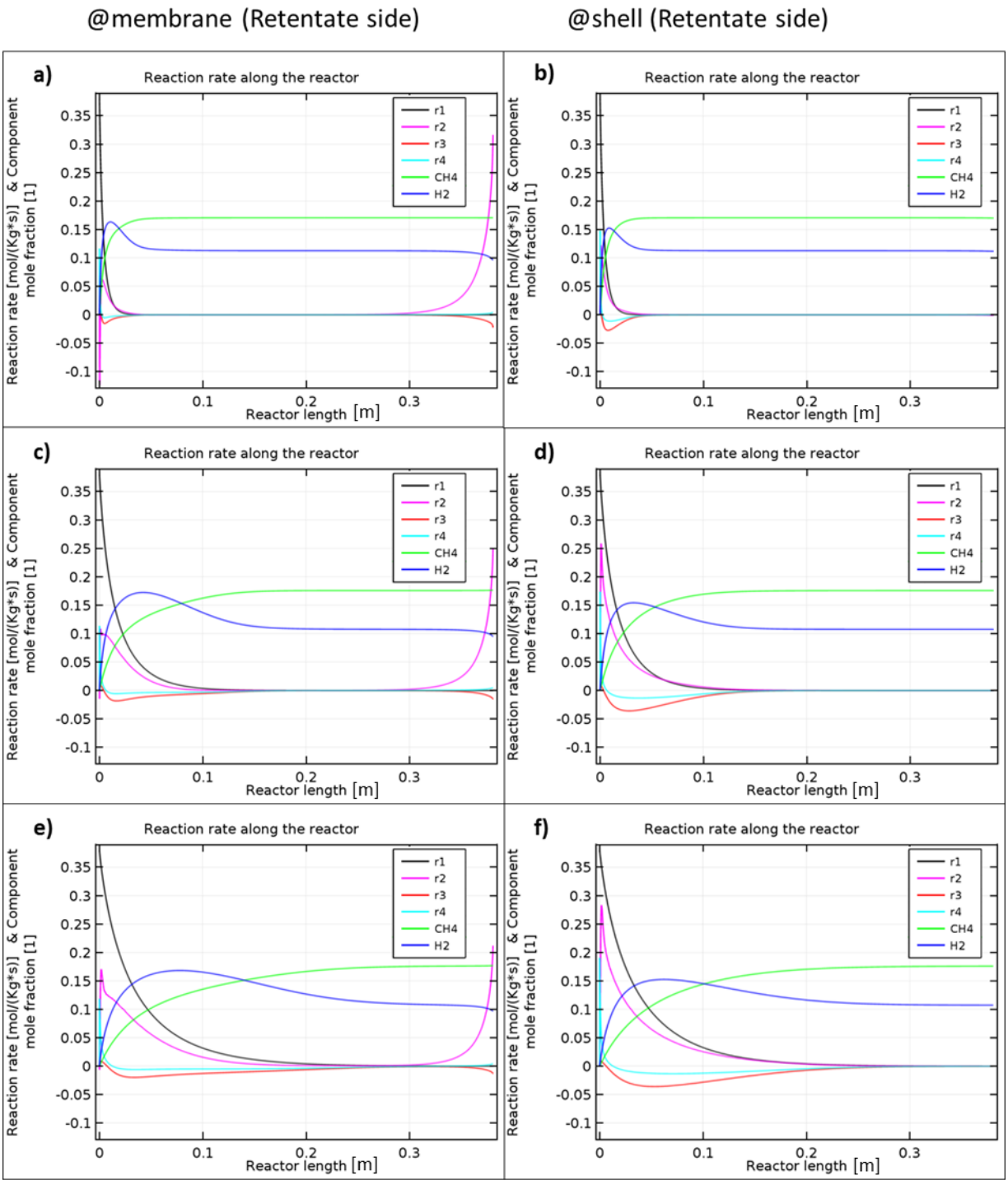

Fig 4.18 Reaction rate (r1:ESR, r2:WGS, r3&r4:MSR) adjacent to the membrane and adjacent to the shell at the experimental condition P_{ret} =6 bar, S/E=5 and T_{in}=723K, a,b at LHSV = 3.77h^{-1}, c,d at LHSV = 18.85 h^{-1}, e,f at LHSV = 37.7 h^{-1}

Although positive reaction takes place again at the end of the reactor, under the original experimental operating conditions equilibrium is still reached in the middle section of the reactor, which can be improved by increasing the inflow rate. While looking at the individual reactions, the reverse methane steam reforming process still exists, but it is less severe than in the co-current system. As shown in Figure 4.18 (a,c,e), the reactor is used more efficiently under higher inflow rate conditions, and the reactor usage is the highest under the condition of LHSV = 37.7 h^{-1}, counter-current sweep gas. From Table 3 for counter-current sweep gas we can again see that ethanol is being completely consumed and hydrogen yield increases slightly as the flow rate increases. Hydrogen recovery decreases as in the co-current case and for the same reasons, however it is slightly higher for each flow rate compared to the co-current results.

Table 4-4. Outlet composition, yield and recovery under counter-current sweep gas flow pattern

LHSV (h^{-1})	C_2H_5OH	CH_4	H_2	CO_2	CO	H_2O	Yield (%)	Recovery (%)
3.77	≈ 0	0.170	0.110	0.0867	0.00227	0.631	15.2	4.97
18.85	8.26E-09	0.176	0.107	0.0987	0.00223	0.616	15.9	1.07
37.7	4.40E-05	0.176	0.107	0.0993	0.00223	0.615	16.0	0.486

For the counter-current sweep gas system, the hydrogen content at the exit of the permeate side is higher compared to the co-current case, which has zero hydrogen content at the same place, and thus less hydrogen is removed from the retentate inlet due to the smaller driving force. A similar characteristic was described by Piemonte et al. (2010) with the study of water gas shift reaction in a counter-current sweep gas reactor, which states that the membrane is less useful at the entrance for a counter-current sweep gas system due to the low driving force and the rapid reaction rate. This accumulation of hydrogen triggered a reverse water gas shift reaction at the entrance of the reactor; however, as the inflow rate is improved, hydrogen accumulation is spread out further down the reactor (Figure 4.19) and the reverse water gas shift reaction is reduced.

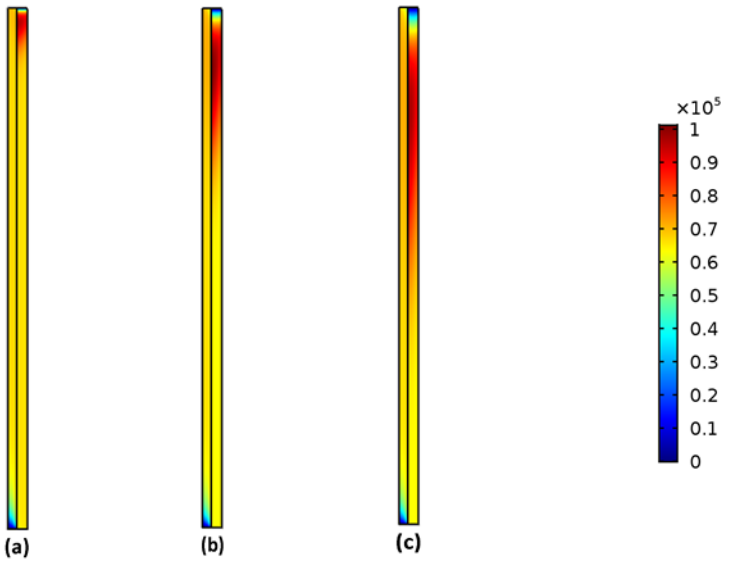

Fig 4.19 Hydrogen partial pressure profile on the permeate side (left) and the retentate side (right) of the reactor at Pret =6 bar, S/E=5 and Tin=723K with (a) LHSV = 3.77 h-1 (b) LHSV = 18.85 h-1 (c) LHSV = 37.7 h-1

The “cold spot” of this system appears at the retentate inlet due to the combined effect of the hydrogen removal and the endothermic property of the steam reforming process (Figure 4.20). Less hydrogen removal at the entrance leads to less heat removal, which brings up the temperature slightly compared to the co-current case. The decrease in reverse methane steam reforming can be explained by the temperature distribution. The “cold spot” appears to be smaller and the temperature within the spot is much higher than previously. At the downstream of the reactor, the reaction rate is not as high as at the entrance. Although the hydrogen removal is higher, no multiple “cold spot” is formed in the rest of the reactor considering the slow reaction and the heat provided by the furnace. Thus, it is possible to conclude that the counter-current sweep gas pattern is beneficial to the temperature control of the ethanol steam reforming process.

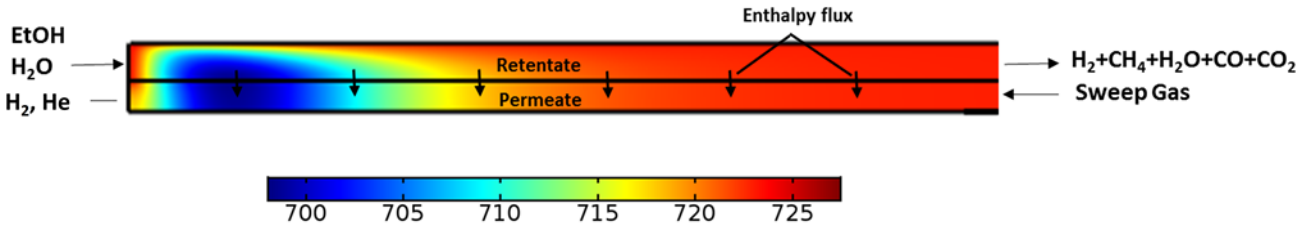

Fig 4.20 Counter-current temperature distribution in the reactor at LHSV=3.77h^{-1}, P_{ret} =6 bar, S/E=5 and T_{in}=723K on both permeate and retentate side.

4.6.4 Study of the reactor pressure and temperature

In order to fully understand the reactor performance of both co-current and counter-current systems, other aspects of the operating conditions, furnace temperature and pressure were studied. Pressure plays an important part in membrane reactors for its significant effect on the thermodynamics of the reactions, and the hydrogen permeation rate. Temperature is an important parameter for reforming processes due to the reactions' highly endothermic property. Figure 4.21 shows that more hydrogen is generated under higher temperature conditions. Although hydrogen removal is favored by higher temperatures, the higher hydrogen generation dominates the reactor performance, as a consequence, a higher hydrogen yield is seen. On the other hand, since the membrane permeance is not as highly thermally activated as reaction rates, hydrogen recovery shows a decreasing trend while yield increases as shown in Figure 4.22.

The effect of pressure on the system can be considered in two aspects, without the effect of membranes, higher pressure leads to lower hydrogen production; however, as the driving force for palladium membrane, higher pressure leads to more hydrogen removal from the retentate side, and a higher hydrogen recovery can be seen (Figure 4.22). In this case, a lower hydrogen yield is observed at higher pressures (Figure 4.21), indicating that the effect of membrane is not prominent and membranes with higher permeabilities can be considered.

Under all the discussed temperature and pressure conditions, the counter-current sweep gas system shows a higher hydrogen recovery, which is a consequence of higher rates of hydrogen removal. On the other hand co-current sweep gas system shows a slightly higher hydrogen yield, which is in agreement with Tosti et al. (2008).

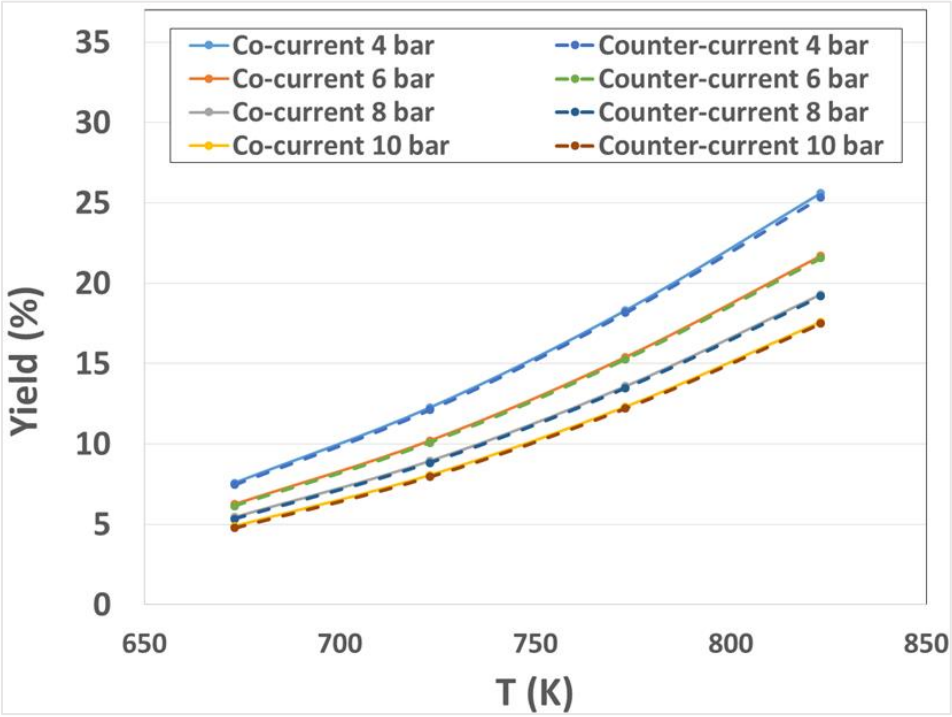

Fig 4.21 Hydrogen yield under different operating temperature and pressure for both co-current and counter-current system.

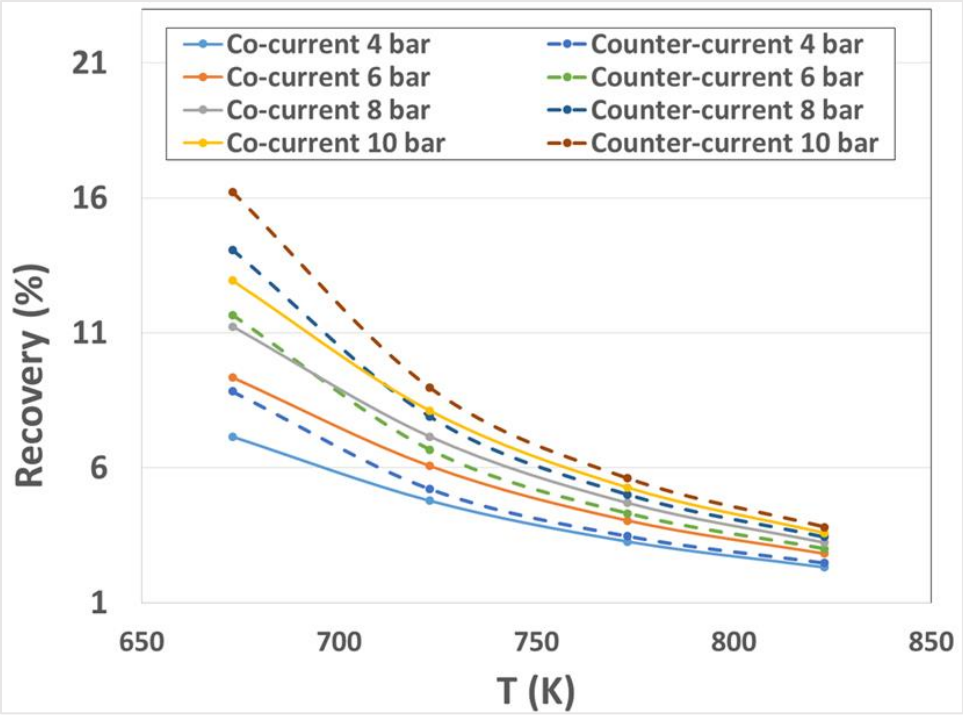

Fig 4.22 Hydrogen recovery under different operating pressures for both co-current and counter-current system.

4.7 Conclusions

The performance of a large-scale catalytic membrane reactor (CMR) used for ethanol steam reforming (ESR) was demonstrated through a comprehensive experimental and computational analysis. In this work, the CMR used a Pd/Au/Pd/Au composite asymmetric membrane that displayed a H_2 permeance of 11 and 21 $Nm^3m^{-2}h^{-1}bar^{-0.5}$ at 350 ^oC and 450^oC, respectively. The performance of the CMR was tested under a range of liquid hourly space velocities (LHSV), operating pressures, temperatures and S/E ratios. The CMR module was operated for 300 hours showing 100% conversion of ethanol for all conditions and producing H_2 with a purity of 99.9% at a rate of 0.38 grams per hour at 5 bar, 500°C, a S/E ratio of 5 and a LHSV of 3.77 h^{-1}. Furthermore, the isothermal 1-D and 2-D simulation models were generated using Polymath and Comsol, respectively. These models were validated first with kinetic data available from conventional reactors. In this work, the models presented an accuracy of 85% and 91%,

respectively, when compared to the experimental results. The simulation models suggested that the production of H_2 can be enhanced by up to 122% when operating a higher pressures and membrane permeances. These results showed that ethanol can be used as an alternative H_2 carrier source and the application of membrane technology significantly enhances its dehydrogenation process.

Furthermore, a 2-D non-isothermal CFD model was developed extending the experimentally validated isothermal models. Both co-current and counter-current sweep gas systems were studied at different operating conditions using the model. The temperature distribution profile was depicted within the reactor. From the temperature profile, a "cold spot" was observed at the reactor entrance as the endothermic reactions proceeded very rapidly. In addition, the hydrogen removal allows for higher conversions. For the counter-current sweep gas system, both the area and the temperature reduction of the cold spot are smaller as the hydrogen permeation driving force is lower at the reactant entrance where the reaction rate is the fastest. Although the hydrogen permeation driving force in the counter-current system is higher at the end of the reactor compared to the co-current system; no "cold spot" is formed at downstream of the reactor since the reaction rate is not as rapid. Low temperature is not ideal for highly endothermic reactions like ethanol steam reforming process, thus the counter-current system is preferred because of the more even temperature distribution. The effect of the "cold spot" was shown from the study of the individual sub-reactions in the ethanol steam reforming process. Reverse methane steam reforming reactions were seen adjacent to low temperature spots.

In order to fully take advantage of the reactor capacity, higher LHSV under both co-current and counter-current systems were studied. It was shown that higher LHSV is beneficial for the reactor usage since the equilibrium is formed further down in the reactor. Likewise, it is shown that the counter-current sweep gas system uses the reactor more efficiently since the previously formed equilibrium can be disturbed at the end of the reactor. It was also shown that at a value of LHSV = 37.7 h^{-1}, in the counter-current system, the reactor is most efficiently used. A higher spatial velocity led to a waste of inflow reactant as the equilibrium was not reached anywhere in the reactor. In conclusion, reducing the "cold spot" in a steam reforming

process is beneficial for the membrane reactor performance and can be achieved by modifying the sweep gas flow pattern. Also, to produce and collect H_2 more efficiently, higher temperatures and pressures are preferred with a proper spatial velocity for the specific reactor scale.

Finally, it is possible to conclude that in order to apply this CMR technology at industrial proportions more pilot-scale prototypes are needed to overcome the current “demonstration-stage” and move to commercialization “deployment-stage”.

5. Methane steam reforming and water gas shift reaction integration

------- *Published as* *Integration of methane steam reforming and water gas shift reaction in a Pd/Au/Pd-based catalytic membrane reactor for process intensification. Membranes, 6(3), 44.*

This work aims to implement the integration of one more processes into a single unit. Specifically, the operation of a large-scale Pd-based CMR module is shown where both MSR and WGS reactions are integrated in a single unit, in order to provide high CH_4 yields with little or no CO. In the CMR, the first catalyst (MSR) is confined on the shell side of the reactor, while the WGS catalyst is positioned subsequently in series. A tubular Pd/Au/Pd membrane situated throughout the reactor, continuously removes the H_2 to yield higher conversions. The higher shell pressure facilitates the acquisition of clean pressurized CO_2 and water, while ultrapure H_2 is obtained in the permeate stream. Furthermore, for comparison, the reaction is carried out in a conventional packed bed reactor for both configurations: MSR and multistage MSR-WGS (5 layers). Additionally, a 2-dimensional computational fluid dynamics (CFD) model was developed in order to further analyze the properties of this unit. Please notice that the aim of this work has a proof-of-concept approach that explores the potential use of catalysts packed in series and/or in parallel to enhance conventional processes.

5.1 Methodology

5.1.1 Membrane fabrication

A composite Pd/Au/Pd membrane was prepared on a 1.27 cm OD and 38.1 cm in length 316L PSS support with media grade of 0.5 μm. The total permeable area of the membrane was 152 cm^2. One end of the membrane was welded to a 316L nonporous capped tube while the other end was welded to a nonporous tube. The support showed an initial He flux of 200 L/min at a pressure difference of one bar. To synthesize the membrane, the support was first covered with

sol-gel and then calcined at 600°C for 12 hours. After calcination, the supports were graded following a previously reported procedure with medium and fine pre-activated powder, provided by Johnson Matthey (UK), based on a 2 wt% Pd-alumina catalyst without any additional activation or treatment (Ma et al. 2000; Ma et al. 2007; Ma et al. 2010). Notice that the grading procedure reduced the He leak across the membrane by 3 orders of magnitude, as shown in Table 5-1. After grading, the surface of the membrane was activated with $SnCl_2$-$PdCl_2$ and then electroless plating was used to deposit a dense Pd layer. A thin gold layer of 0.2 μm was deposited on top of the palladium surface via conventional electroplating. Notice that gold has been shown to enhance the properties of Pd-based membranes such as: permeance, stability and contaminant-recoverability (Chen et al. 2010) and therefore was used in this work. Finally, to provide active sides on this asymmetric membrane and further reduce the He leak present, a pure Pd topmost layer was deposited. The thickness of the membrane was estimated by gravimetric methods. The final composition and leak of the membrane was 6.9 Pd/ 0.2 Au/ 3.2 Pd and < 0.01 sccm/bar, respectively. The thicknesses and He leak at each step of the synthesis are shown in Table 5-1.

Table 5-1. Characteristics of the membrane at different phases of the synthesis

Membrane synthesis step	Thickness / μm	He Leak (sccm/bar) @25°C
Initial support	NA	197,360
Oxidation and calcination	NA	91,830
Grading Pd(Al_2O_3)	2.8	66
Pd layer	6.9	3
Au deposition	0.2	1.39
Pd layer (final)	3.17	NA

5.1.2 Reaction tests and membrane characterization

The H_2 permeation tests and reactions were performed in the same WGS-CMR rig previously reported by Catalano et al. (2012). The composition of the feed was controlled by mass flow controllers and premixed with steam generated in a preheater. The wet mixture was fed to the reactor which contains the membrane surrounded by the catalysts. The catalysts used for MSR and WGS were a nickel-based catalyst (HiFUEL R110, Alfa-Aesar) and an iron-chrome catalyst (HiFUEL W210, Alfa-Aesar), respectively; these catalysts were crushed and sieved (16/+40 mesh) before usage. The water of the retentate was condensed, while the product and retentate flow rates were passed through water absorbent beds before the composition was measured by mass flow meters and a gas chromatograph (J. Catalano 2012). Three main experiments were conducted on the CMR-rig including: i) MSR in a conventional packed bed reactor (PBR), ii) multi-staged (5 layers) MSR/WGS in a PBR, and iii) MSR/WGS in a CMR. It is important to note that no sweep gas was utilized in any of the experiments presented in this work.

For the CMR reaction, a protective cage was designed in order to prevent any potential damage of the membrane caused by the friction of the catalyst particles and the wall of the membrane as previously reported in the literature (Fernandez et al. 2015; Brunetti et al. 2015). The cage was made out of stainless steel grids and it consisted of two concentric confines; one surrounded the membrane while the other was used to hold the catalyst in place, as shown in Figure 5.1b. Notice that the surface of the membrane was never in contact with the grid of the cage. The catalyst section of the cage had a volume was of 480 cm^3 and it was filled with 120 g of MSR catalyst and 120 g of WGS catalyst for the membrane reactor, while the PBR was packed in 5 sections. This membrane-catalyst cage system can be up-scaled in order to develop multitube CMR modules.

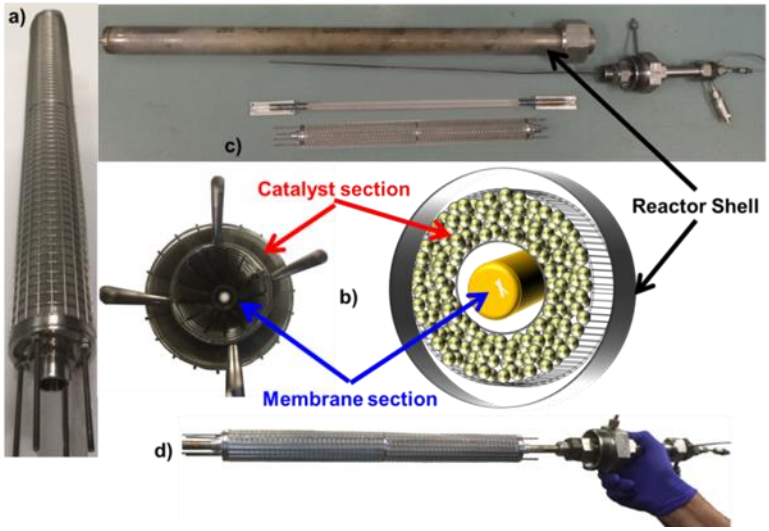

Fig 5.1 Cage, catalyst and membrane configurations used in this work: a) assembled protective cage without a membrane, b) cross-sectional view of the cage and its schematic representation, c) different components of the CMR module, d) integrated cage-catalyst-membrane

5.1.3 CFD simulation framework

A detailed modeling framework, helpful for the analysis of CMRs, has been used for the interpretation of data (Dixon et al. 2003) and accordingly, a 2-D computational fluid dynamics (CFD) model was developed in COMSOL Multiphysics 4.3b in order to examine the properties of the module and compare theoretical values with experimental results. A 2-D configuration of the model was chosen in order to include the non-ideal flow effects that occur in the reactor due to the axisymmetry of the reactors. The performance of the simulation was compared against the experimental values obtained in this work and, for MSR, against the 1-D model presented by Ayturk et al. (2009) where a 99.4% accuracy was found when compared to other literature sources including conventional PBRs and CMRs. Figure 5.2 shows the configuration of the 2-D model, where the MSR catalytic section is located adjacent to the feed flow stream, followed by the WGS section upstream; the membrane was specified to be at the bottom, taking advantage of the symmetrical configuration of the reactor module; additionally, the mathematical mesh, displayed in Figure 5.2, is used to solve the momentum and continuity

equations for retentate side (Equation 5-1 to 5-3) [COMSOL Multiphysics]. The Darcy-Forchheimer law was applied in the present model accompanied by the following assumptions:

1) Isothermal conditions
2) Steady state
3) Laminar flow
4) Non-slip boundary condition for the fluid flow
5) Negligible effect of the protective cage on the flow pattern

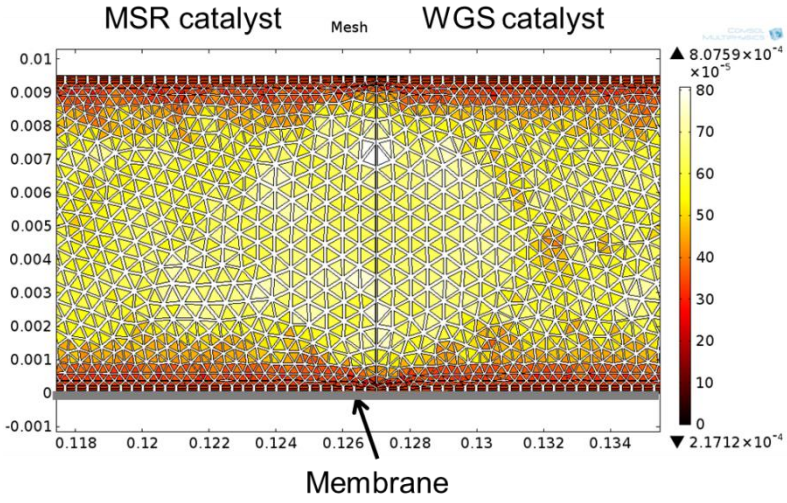

Fig 5.2 Configuration of the CMR simulation depicting the two catalyst sections, the location of the membrane, and the size and geometry of the used mesh

The modified Navier-Stokes equation for a fixed bed porous medium is:

$$\frac{\rho}{\varepsilon_p}\left((u\cdot\nabla)\frac{u}{\varepsilon_p}\right)=\nabla\cdot\left[-pI+\frac{\mu}{\varepsilon_p}(\nabla u+(\nabla u)^T)-\frac{2u}{3\varepsilon_p}(\nabla\cdot u)I\right]-(\mu k^{-1}+\beta_F|u|)u+F \qquad (5\text{-}1)$$

where ε_p represents the system porosity and β_F is Forchheimer coefficient

$$\nabla\cdot(\rho u)=0 \qquad (5\text{-}2)$$

$$\nabla\cdot(-D_i\nabla c_i)+u\cdot\nabla c_i=R_i \qquad (5\text{-}3)$$

The reaction rates for MSR were specified as (M.E. Ayturk 2009):

$$r_1 = \frac{k_1}{P_{H2}^{2.5}} \frac{P_{CH4}P_{H2O} - (P_{H2}^3 P_{CO}/K_1)}{DEN^2} \quad (5\text{-}4)$$

$$r_2 = \frac{k_2}{P_{H2}} \frac{P_{CO}P_{H2O} - (P_{H2}P_{CO2}/K_2)}{DEN^2} \quad (5\text{-}5)$$

$$r_3 = \frac{k_3}{P_{H2}^{3.5}} \frac{P_{CH4}P_{H2O}^2 - (P_{H2}^4 P_{CO}/K_3)}{DEN^2} \quad (5\text{-}6)$$

where DEN is defined as:

$$DEN = 1 + K_{CO}P_{CO} + K_{H2}P_{H2} + K_{CH4}P_{CH4} + \frac{K_{H2O}P_{H2O}}{P_{H2}} \quad (5\text{-}7)$$

Notice that r_1, r_2 and r_3, correspond to the reactions specified in Eq. 5-4, 5-5 and 5-6, respectively. Refer to the previous literature for the kinetic, adsorption and equilibrium constants (Ayturk et al. 2009). Furthermore, the reaction rate used for the WGS reactor model over Fe-Cr based catalyst was specified as:

$$r4 = 10^{2.845} \cdot e^{\frac{-111}{Rg \cdot T}} \cdot P_{CO}^{1.0} P_{CO2}^{-0.36} P_{H2}^{-0.09} \cdot \left[1 - \frac{P_{H2}P_{CO2}}{K\, P_{H2O}P_{CO}}\right] \quad (5\text{-}8)$$

where K is the equilibrium constant.

The reaction model is homogenous as the internal effectiveness factor was calculated to be 1. The internal effectiveness factor is defined as the actual rate of reaction divided by the rate of reaction that would occur if the entire internal surface of the catalytic particle would be exposed to the external conditions.

Additionally, the flux across the membrane (N_i) was based on Sieverts' law as follows (Ayturk et al. 2009; Ma et al. 2016):

$$N_i = \overline{P_{H2}} \left(\sqrt{P_{H2}^{Shell}} - \sqrt{P_{H2}^{Tube}} \right) \quad (5\text{-}9)$$

where P_{H2}^{Shell} and P_{H2}^{Tube} represent the hydrogen partial pressure at the retentate side and the permeate side, respectively, and $\overline{P_{H2}}$ is the permeance of the membrane obtained experimentally. Furthermore, the calculation of binary fluid diffusion coefficients (D_m) were estimated according to standard engineering procedures (Bird et al. 2007):

$$D_m = 0.0018583 \sqrt{T^3 \left(\frac{1}{M_A} + \frac{1}{M_B}\right)} \frac{1}{P\sigma_{AB}^2 \varphi_{D,AB}} \quad (5\text{-}10)$$

where M_i is the molecular weight of component i, P is the pressure of the system, σ_{AB}^2 denotes the parameters of the Lennard-Jones potential between molecules A and B, and $\varphi_{D,AB}$ represents the collation integral for diffusion.

The longitudinal and transversal dispersion D_L and D_T are calculated using equations below (Delgado 2006):

$$Pe_m = \frac{d \cdot u}{D_m} \quad (5\text{-}11)$$

$$1/Pe_L = 1/(\tau \cdot Pe_m) + 1/2 \quad (5\text{-}12)$$

$$1/Pe_T = 1/(\tau \cdot Pe_m) + 1/12 \quad (5\text{-}13)$$

$$D_L = u \cdot d/Pe_L \quad (5\text{-}14)$$

$$D_T = u \cdot d/Pe_T \quad (5\text{-}15)$$

where Pe_m, Pe_L and Pe_T are the molecular Peclet number, the longitudinal Peclet number and the transversal Peclet number, respectively, τ denotes tortuosity and d represents the catalyst particle diameter.

The conversion of methane was defined as (Ayturk et al. 2009):

$$X_{conversion} = \frac{F_{CH4,feed} - F_{CH4,ret}}{F_{CH4,feed}} \quad (5\text{-}16)$$

5.2 Test and simulation result analysis

5.2.1 He leak test and H_2 permeation test of the membrane

After the module was installed in the CMR rig, the temperature of the membrane module was increased from room temperature to 350^{o}C under He gas at a rate of 1^{o}C/min and a pressure of 2 bar. At this temperature, a helium leak test showed undetectable leak and H_2 was introduced to the module. Hydrogen permeance was measured as a function of time continuously every 30 seconds as shown in Figure 5.3. After 80 h, the temperature was increased to 450^{o}C displaying a slight increase in H_2 permeance. The temperature was kept for 160 h and two helium leak tests were performed displaying undetectable He leak. Notice that on the first He leak test, steam was fed to the system along with He for one hour to fully oxidize the WGS catalyst. The membrane showed a H_2 permeance of 70 and 80 $Nm^3m^{-2}h^{-1}bar^{-0.5}$ at 350 and 450^{o}C, respectively. After 290 hours of continuous testing, the module temperature was increased to ~600 ^{o}C under pure H_2 stream for 3 h to activate the MSR catalyst. Notice that after activation, the membrane presented a He leak of 0.4 sccm/bar at 450 ^{o}C. The asymmetric Pd/Au/Pd membrane showed high H_2 flux and an ideal H_2/He selectivity of over 4,300 after the catalyst was activated. Even though it has been shown that to improve the thermal stability of the membranes, porous Hastelloy and Inconel supports perform better than PSS at temperatures higher than 500^{o}C (Uemiya et al. 1999), the membrane showed a high thermal stability.

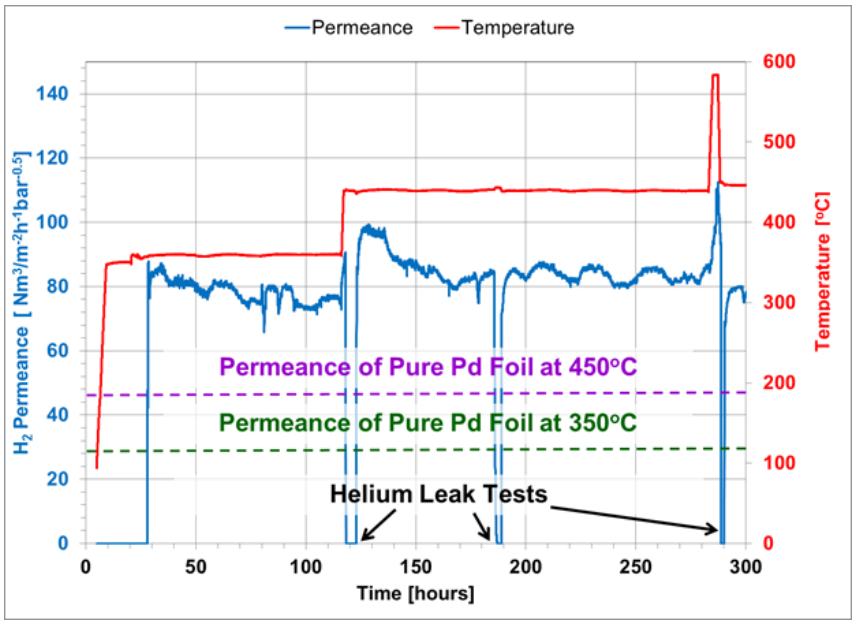

Fig 5.3 Hydrogen permeance, He leak tests at 350, 450 and activation at 585°C at different elapsed times

Moreover, Gade et al. (2009) showed that unannealed Pd-Au membranes require ~300 hours under typical operating conditions to fully anneal *in situ* the Pd-Au surface of the membrane and consequently reach a steady H_2 flux. Nevertheless, as shown in Figure 5.3, after H_2 feed was introduced in to the system at 350°C, the H_2 flux across the membrane reached a steady state very fast. This effect could be the result of plating Pd on top of the Au surface which added active sites for the permeance to occur.

Pure Pd membrane foils have shown a H_2 permeance that follows the Arrhenius correlation as shown in Equation 20, where *t* is the thickness of the membrane in µm, 15,630 is the activation energy in J/mol and 6322.7 is the pre-exponential factor in $m^3\mu m.m^{-2}h^{-1}atm^{-0.5}$ (Ayturk et al. 2009). Furthermore, considering that the presented Pd/Au/Pd membrane has a Pd layer of 10.1 µm, the expected permeance of its pure Pd foil analog is 47 $Nm^3m^{-2}h^{-1}bar^{-0.5}$ at 450°C. It is important to mention that the hydrogen permeance of the presented Pd/Au/Pd membrane is superior by a factor of 1.7. This enhanced behavior of the membrane is due to the presence of gold, which as previously reported (Guazzone et al. 2012; McKinley et al. 1966) can raise the permeance up to 2 times higher due to an increase in diffusivity. Although the amount of gold

in the presented membrane is 2%, which is below the optimum 5% (Gryaznov et al. 2000), the membrane displayed an excellent and stable H_2 flux.

$$\overline{P_{H2}} = \left[6322.7\, e^{-\frac{15630}{RT}}\right]/_{t} \quad (5\text{-}17)$$

5.2.2 MSR in traditional packed bed reactor (PBR) with single catalyst

Methane steam reforming was carried out in a conventional packed bed reactor (PBR) to experimentally demonstrate the effect of process intensification and the presence of the secondary catalyst. As mentioned before, the major advantage of the CMR compared to a conventional PBR is the conversion enhancement of the equilibrium-limited MSR by removing in-situ the produced H_2. Therefore, in order to study the performance of a PBR, a solid stainless steel pipe was placed instead of the membrane in order to maintain identical geometric features of the CMR reactor. As shown in Figure 5.4, different space velocities, temperatures and steam-to-carbon ratios were used to investigate the performance of the PBR; all reaction conditions were set to a total pressure of 2 bar, since higher pressures did not show significant changes in the reaction performance. Notice that the catalyst loading was set around 5000 h^{-1} as specified by the provider of the catalyst. Furthermore, the experimental results were graphically depicted along with the computational simulation outcomes as shown in Figure 5.4.

We examine the performance of the PBR by analyzing its methane conversion at 500^{o}C and a steam-to-carbon ratio of 3. It is observed, that even at small space velocities, methane conversion is below its chemical equilibrium (shown as a dotted line in Figure 5.4); this effect is caused by the reduction of the contact time of methane with the catalyst. Furthermore, the effect of temperature on the conversion of methane is clear; it increased from 40 to 60% when the temperature of the reactor was increased from 500 to 600^{o}C. This is in agreement with the fact that MSR is an endothermic reaction which is highly favored by high temperatures.

Additionally, adding steam has a positive effect on the reaction, doubling the conversion when the steam-to-carbon ratio is increased from 3 to 5. Furthermore, excess steam is generally

present in the MSR process since it not only increases conversion but also prevents coke formation. It is important to mention that the results presented in this work are similar to the results reported in the pertinent literature (Ayturk et al. 2009; Gallucci et al. 2004). Additionally, the CFD simulation results, shown in Figure 5.4, match the experimental data with an average error of 7.8%. The experiments were carried out in a pilot-scale module and therefore these results were more susceptible to divergence from controlled settings.

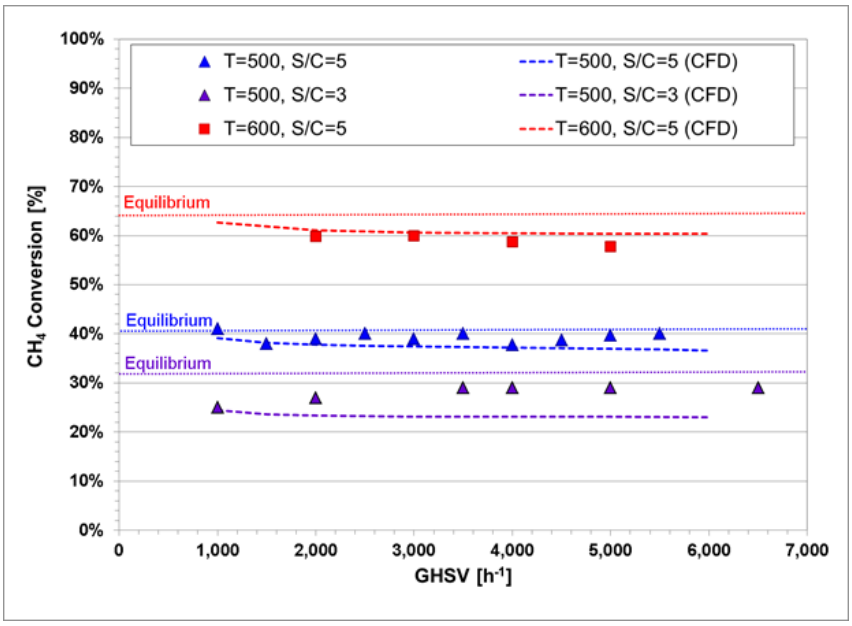

Fig 5.4 Experimental and computer simulation methane conversions in a PBR as a function of different space velocities and conditions at a total pressure of 2 bar.

5.2.3 MSR/WGS in traditional packed bed reactor (PBR) with dual catalyst

The reforming of methane and the water gas shift reactions were studied in a conventional packed bed reactor (PBR) to demonstrate the effect of the secondary catalyst and thus effectively demonstrate the presence of a membrane. The reactor was packed in stages while a solid stainless steel pipe was used instead of a membrane in order to maintain the geometry of the module as shown in Figure 5.5. The PBR was packed in series with a fresh Ni-based reforming catalyst and a Fe-Cr based WGS catalyst with an overall proportion of 20% and 80% for reforming and WGS, respectively. The configuration of the catalysts within the reactor,

shown in Figure 5.5, was split as MSR-WGS-MSR-WGS-MSR. The MSR-WGS reactor was tested at 475^{o}C since the Fe-Cr catalyst temperature limit is specified by the provider to be of 500^{o}C. After packing the module, steam and He were fed to the system to oxidize the WGS catalyst. The catalyst emitted H_2 and therefore oxidation continued until H_2 was not detectable by the GC (Catalano et al. 2012); this process took around 1 hour. Afterwards, the temperature of the module was increased to ~600 ^{o}C under pure H_2 stream for 3 h to activate the MSR catalyst. After these procedures, the reaction tests were carried out. Notice that a CFD simulation for this multistage packing configuration was performed to further analyze the PBR.

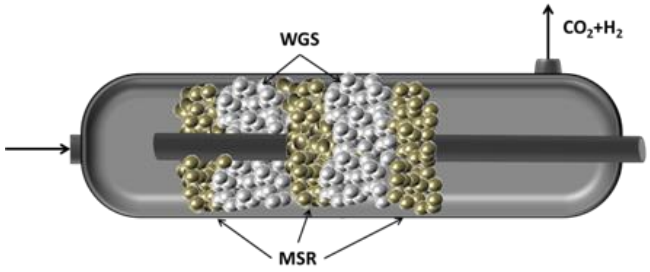

Fig 5.5 Conceptual illustration of the catalyst distribution throughout the PBR reactor with the left side cut away to show the tube and the catalyst.

The conversion of methane at 475^{o}C, 2 bar and a GHSV of 3500 h^{-1} was found to be 18% as shown in Figure 5.6; however, it decreased slightly as the pressure was increased. It is important to mention that the purpose of adding the WGS catalyst is to prevent or reduce the formation of CO in the module. As shown by Figure 5.6, it can be observed that although in small quantities, CO is present in the product of the reaction. For both, experiments and simulations, the amount of CO reduces as pressure increases; this indicates that the production of CO may be hindered by pressure, or that the activity of the WGS catalyst is favored at higher pressures (Eq. 2). Given the stoichiometry of MSR (Eq.1-3), a reduction of methane conversion and simultaneously CO generation as the pressure of the reactor increases is expected; at the same time, as reported by Atwood et al. (1950), the WGS reaction intensifies at higher pressures. These two mechanisms contribute to obtaining lower CO yields.

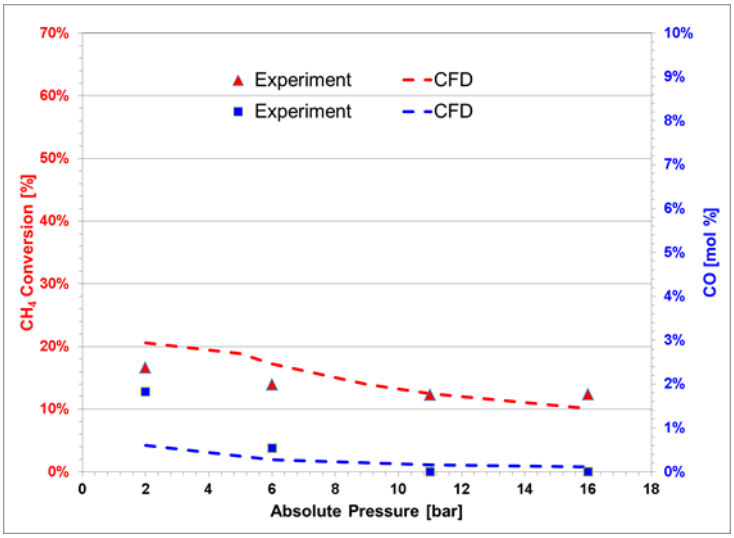

Fig 5.6 Experimental and computational simulation of two catalysts in a PBR as a function of different pressures at a GHSV of 3500 h^{-1}, a temperature of 475 ^{o}C and S/C=5.

It is important to notice that in this dual-catalyst reactor, the WGS reaction occurs in the presence of a significant amount of H_2, which limits its performance. Figure 5.7 shows that even though lower theoretical CO is present in the dual-catalyst reactor; the experimental results of the pilot-scale bed appeared to be hindered by the intrinsic error in the measurements. Nevertheless, through the simulation, it is found that as the space velocity increases, the difference in CO production decreases further for the dual-catalyst bed. This effect can be attributed to two factors: i) the reduced presence of H_2 and ii) lower concentrations of CO. The aforementioned factors are generated due to reduced CH_4 conversions. Additionally, a surface plot of CO concentration through the reactor module is shown in Figure 5.8 to illustrate the effect of the water-gas-shift catalyst. At first, CO is generated on the first MSR catalyst bed section, followed by its consumption by the WGS reaction zone. The next MSR layer induces the production of more CO which is later reduced by the following WGS segment. Finally, the MSR catalyst at the end of the PBR increases the overall CO concentration inside the reactor.

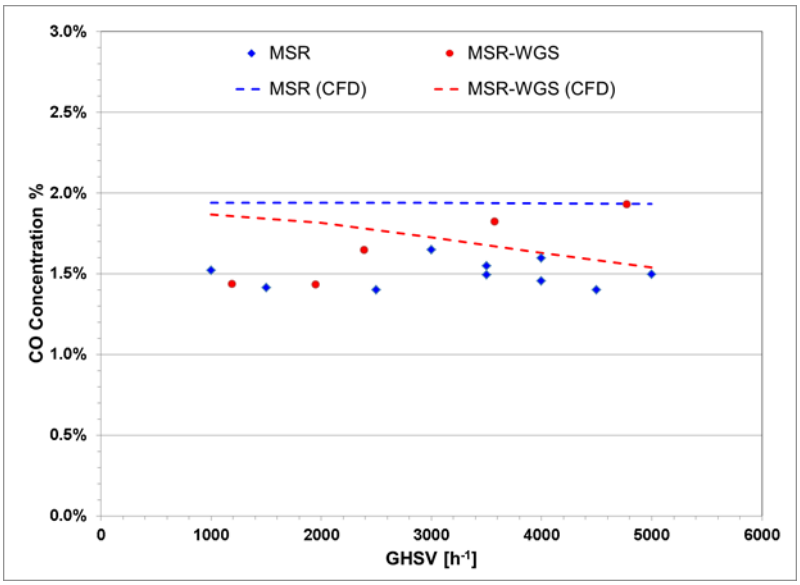

Fig 5.7 Concentration of CO in conventional PBRs containing a single MSR catalyst and dual MSR-WGS catalyst at a pressure of 2 bar, a temperature of 475 ^{o}C and a S/C=5.

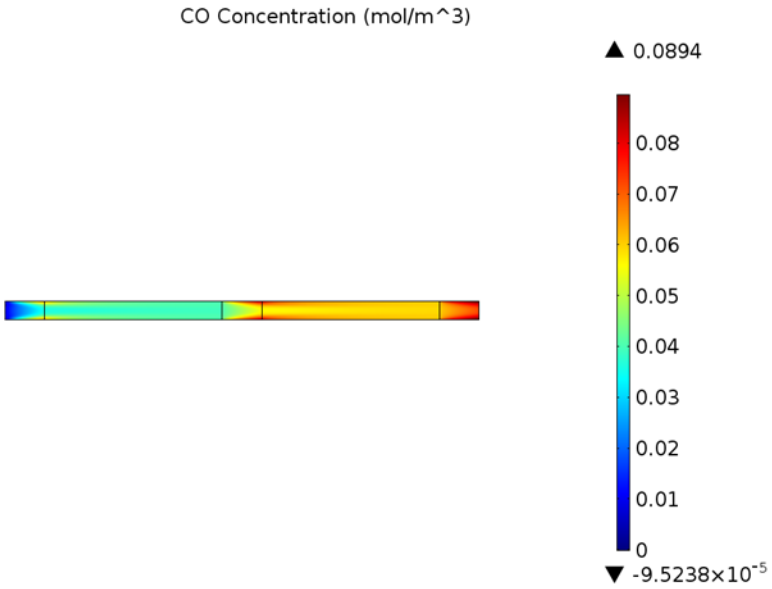

Fig 5.8 CFD concentration profile of CO inside in a PBR containing MSR-WGS catalysts

5.2.4 MSR/WGS in a catalytic membrane reactor (CMR)

The CMR was packed with two layers of catalysts in series only (in contrast with the 5 layers in the PBR) and with a membrane placed at the center of the reactor to remove in situ the H_2 generated by the reactions. The experimental CH_4 conversion results are shown in Figure 5.9 for different steam-to-carbon ratios, a temperature of 475°C and a pressure of 5 bar. The highest conversion achieved was of 43.3% at a steam-to-carbon-ratio of 5 and a space velocity of 1172 h^{-1}. Furthermore, it is found that as the GHSV was increased, the conversion of methane decreased accordingly; this was caused by the reduction of residence time in the reactor. In addition, the amount of water influenced the reaction significantly; a steam-to-carbon ratio of 5 produced about 20% higher CH_4 conversion than a ratio of 3. Notice that the H_2 purity generated by this Pd/Au/Pd membrane was 99.94% throughout a testing time of 350 hours under MSR/WGS conditions. The best flux achieved by the CMR under optimum conditions was over 500 NL/day. After the experiments were terminated, the surface of the membrane did not show carbon deposition for the reason that the protective cage separated effectively the reaction zone from the membrane.

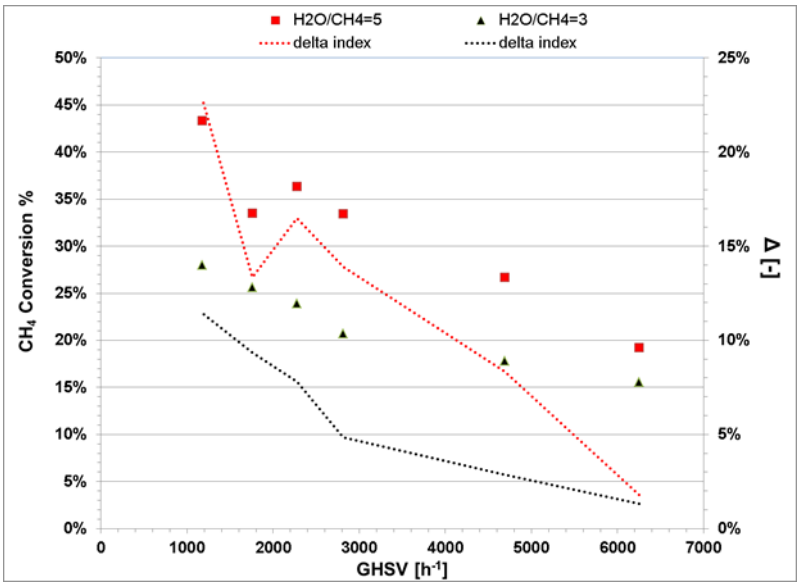

Fig 5.9 Experimental methane conversion of the dual catalyst CMR represented as scatter points and difference between CMR and PBR at 5 bar, a temperature of 475 °C.

The reactor performance indicator for process intensification was quantitatively analyzed based on the Δ-index previously reported by Ayturk et al. (2009). This index is represented in Equation 5-18 as the difference between the CH_4 conversion achieved by the CMR and the one by PBR under similar conditions.

$$\Delta = X_{CH4}^{CMR} - X_{CH4}^{PBR} \quad (5\text{-}18)$$

It is important to mention that the PBR was not operated experimentally at 475°C and 5 bar; consequently, the CFD performance outcome of the conventional PBR was utilized to estimate the Δ-index of this work. The Δ-index represented in Figure 5.9 shows that at all GHSV the conversion of methane increases when sized against a conventional reactor. Nevertheless, the concept of process intensification is better appreciated at low space velocities since H_2 has better rate of removal and the contact time of the gases with the catalysts increases.

For the simulation result, as expected, compared to a PBR, the constant removal of H_2, shown by the hydrogen concentration profiles in Figure 5.10, changes the composition of the retentate allowing both reactions to proceed further. In Figure 5.10, it is possible to observe that as soon as the feed stream (on the left) is in contact with the catalyst bed, H_2 is generated and increases as the reaction proceeds; this continues until the H_2 partial pressure in the retentate is high enough to provide the driving force for the membrane to start removing it. Notice that even though the reaction continues to take place in the module, an increase in H_2 concentration is no longer observed; this effect is caused by the rate of removal overcoming the rate of reaction. Furthermore, it is possible to observe from top to bottom, a gradual reduction in H_2 concentration caused by the presence of the membrane. This reduction in H_2 concentration adjacent to the surface of the membrane causes a H_2 depleted boundary layer formed by low radial diffusion rates. This effect is often referred as concentration polarization and it can significantly reduce the performance of the membrane (Zhang et al. 2006).

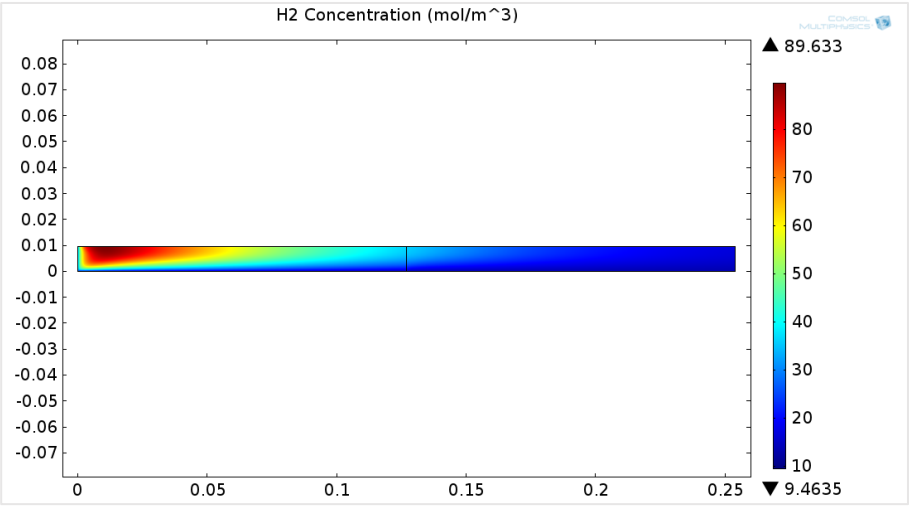

Fig 5.10 Concentration profile of H_2 inside in a dual MSR-WGS catalytic membrane reactor

To further characterize the performance of the membrane reactor the product of Damkohler and Peclet numbers (DaPe number) is utilized since it provides the ratio of maximum reaction rate over maximum permeation rate per volume (Battersby et al. 2006). In PBRs, the Damkohler number (Da) exemplifies the performance of the reactors, since it shows the ratio of the reaction rate over the convective mass transport of the reactant; while in membrane technology, the Peclet number shows the relative convection transport rate over the diffusive rate (permeation). Consequently, the product DaPe dictates the overall effectiveness of the CMR; for instance, having a DaPe > 1, means that the permeation rate is low and thus the H_2 rate of removal through the membrane is the limiting factor of the reactor's productivity. As reported by Battersby et al. (2006), the DaPe number can be estimated as shown in Equation 5-19 where $X_{equilib}$ is the conversion achieved when the reaction is thermodynamically at equilibrium and X_{actual} is the conversion displayed by the membrane reactor. Most of the DaPe numbers displayed by this CMR, shown in Table 5-2, are lower than one; this implies that the rate of H_2 removal is high enough to change the pseudo-equilibrium state favorably to achieve higher conversions. Notice that the term "pseudo-equilibrium" is used to describe the situation where the reaction product (H_2) is independently manipulated, by the use of a permeable membrane (Battersby et al. 2006). Furthermore, Table 5-2 shows that at high GSHV, the DaPe number approaches one, implying that the rate of reaction matches the maximum permeation

equivalent. It is important to mention that it is considered that the optimum design of a CMR should operate at a theoretical DaPe =1.

$$\mathrm{DaPe} = \frac{\mathrm{X_{equilib}}}{\mathrm{X_{actual}}} \tag{5-19}$$

Table 5-2. DaPe number of the dual catalyst CMR at different space velocities at 5 bar and 475 ^{o}C.

GHSV [h^{-1}]	1170	1750	2270	2810	4680	6250
DaPe number	0.47	0.61	0.56	0.61	0.77	1.07

The concentration of CO in the system was undetectable in this dual catalytic CMR. However, it is not clear if this is the result of the presence of the secondary WGS catalyst or if it is caused by the presence of a H_2-permeable membrane as previously reported (Catalano et al. 2012; Lin et al. 2003; Bi et al. 2009; Augustine et al. 2011). For instance, Lin et al. described a reduction of CO yield from 50% to < 2% in a Pd-based CMR (Lin et al. 2003). Therefore, to observe the effect of the secondary catalyst, a simulation of both single and dual catalyst CMRs was performed. In Figure 5.11a), it can be observed that the CO yield increases in both CMRs as the temperature is increased and the GHSV is reduced. Nonetheless, the effect of the secondary catalyst is also observed by reducing the CO yield, especially at higher operating temperatures. For instance, at the lowest GSHV and 650^{o}C, the CO yield at the retentate is reduced from 9% on the CMR with one catalyst to 6.5 % on the dual CMR, while at 450^{o}C, it is reduced from 0.2% to < 0.05%.

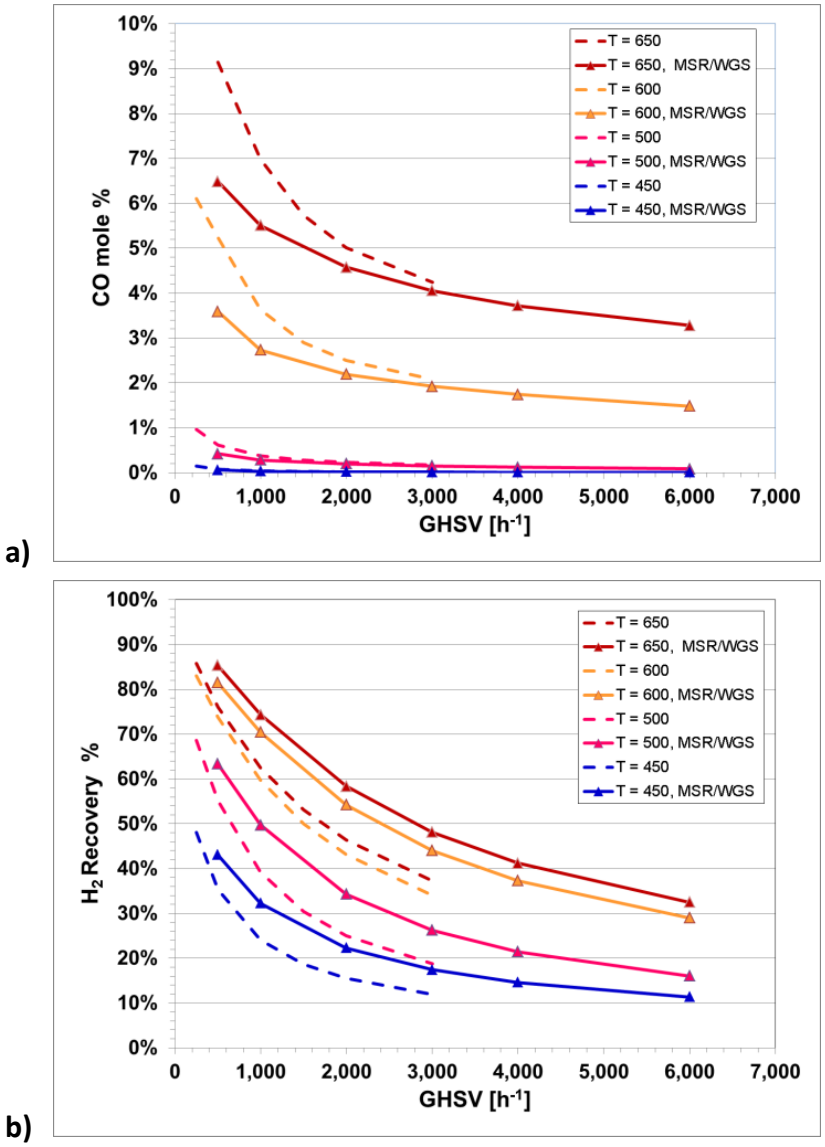

Fig 5.11 a) CO yield and b) H_2 recovery for single and dual CMRs at 5 bar and a carbon-to-steam ratio of 5.

Additionally, Figure 5.11b) shows the H_2 recovery obtained by the CMRs at different space velocities and temperatures. In both CMRs, H_2 recovery increases with higher temperatures and reduced GHSV since these conditions are favorable for higher CH_4 conversions. Additionally, it can clearly be seen that H_2 recovery increases in the dual CMR particularly as the temperature increases. For instance, the operation of the dual bed at 600^{o}C is expected to produce more H_2

than that the conventional single stage CMR. Additionally, lower CO yields intrinsically mean not only higher H_2 generation and enriched CO_2 streams at the retentate, but also the potential reduction of CO poisoning of the membrane. Several studies have shown that severe reductions in H_2 permeance occur in the presence of CO mainly caused by the adsorption of CO on the Pd surface hindering the active sites available for H_2 to adsorb (Li et al. 2000). Reacting CO with H_2O in the catalyst section allows the membrane to be less exposed to CO reducing poisoning. Furthermore, the presence of the WGS can potentially decrease coking when operating at low steam-to-carbon ratios, as carbon formation is thermodynamically favored by the dissociation of CO (Rostrup-Nielsen et al. 1993).

$$2CO \leftrightarrow C + CO_2 \tag{2-20}$$

The results obtained in the present work were compared against those shown in the literature for methane steam reforming, as shown in Figure 5.12a. The conversion of methane in traditional PBRs (TR) and membrane reactors (MR) from different literature sources was plotted against different temperatures as reported by Gallucci et al. (2004) and it is shown to be in agreement with previously reported values. Furthermore, various CO mole fractions at the outlet of the reactor were graphically represented as a function of different methane conversions as shown in Figure 5.12b. The composition of CO shown experimentally by this work is significantly lower those shown in other sources, suggesting that the additional WGS catalyst in the CMR helped in decreasing the residual CO.

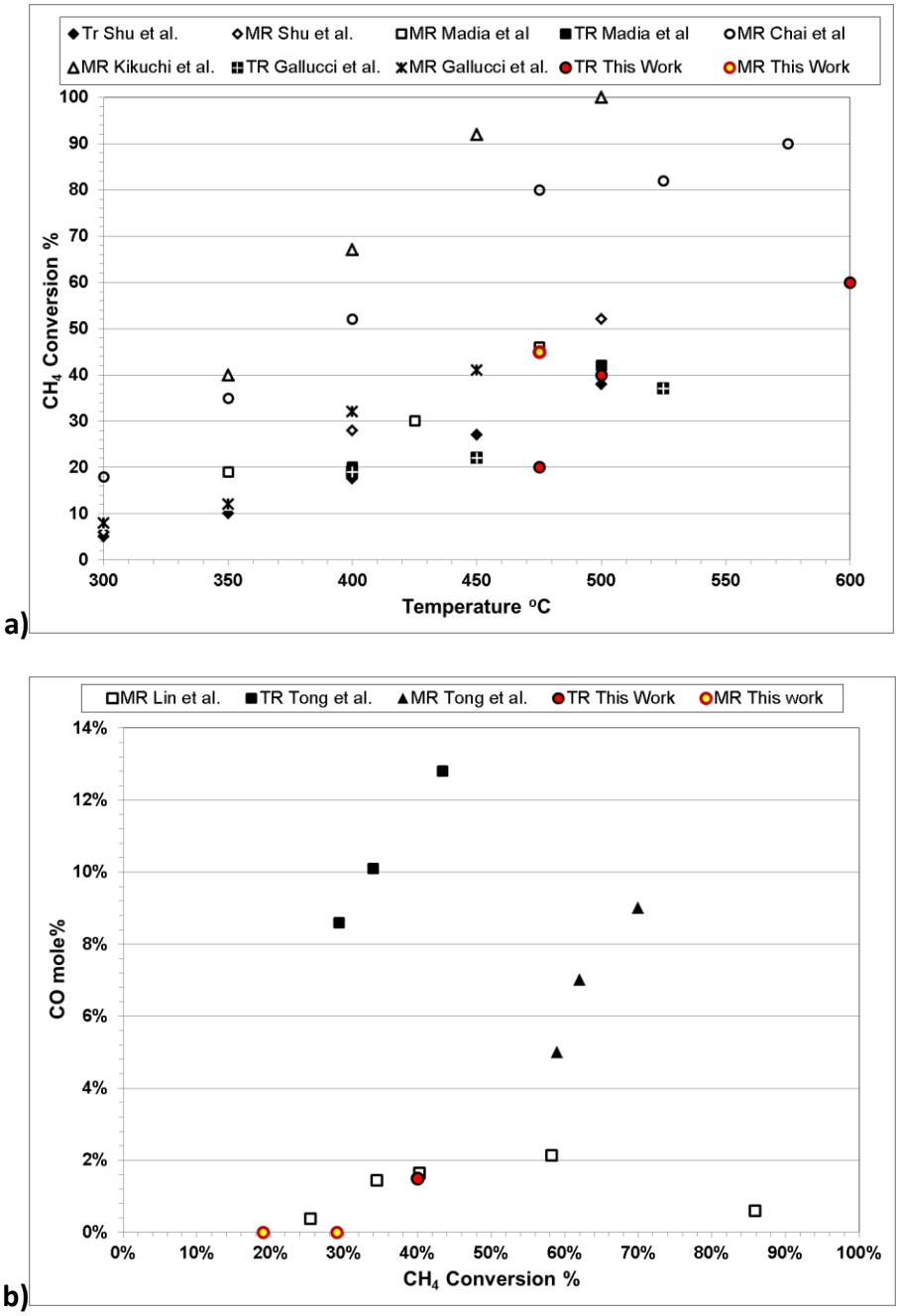

Fig 5.12 Comparison of the results presented in this work against those presented in the literature for a) methane conversion and b) CO yield at 450-500°C and 2-5 bar (Tong et al. 2006; Gallucci et al. 2004)

5.3 Conclusions

The concept of catalyst packing in series was further explored through the development of a catalytic membrane reactor (CMR) module utilizing two catalysts positioned in series. In the process system under consideration, the methane steam reforming catalyst (MSR) is placed first to generate CO and H_2, followed by a water-gas-shift layer placed in series used to react CO, thus producing a higher H_2 yield. In particular a tubular Pd/Au/Pd membrane was synthesized, characterized and accommodated throughout the reactor to remove the produced H_2 in-situ. The membrane was surrounded by a protective catalyst-cage in order to protect the surface of the membrane which helped in preventing carbon deposition on the surface of the membrane. The performance of this novel reactor was comparatively assessed against a conventional packed bed reactor (PBR) with no stages as well as five-catalyst stages. In addition, a computational fluid dynamics (CFD) simulation framework in 2-D was developed to further analyze the characteristics of the CMR. The experimental results for the conventional and CMR module are in agreement with the simulation-generated performance characterization ones. Moreover, the membrane used in this work displayed experimental H_2 permeances of 70 and 80 $Nm^3m^{-2}h^{-1}bar^{-0.5}$ at 350 and 450^oC, respectively. Notice that this configuration is reported for the first time in the pertinent literature and exhibited excellent technical performance. Indeed, it was demonstrated that excellent H_2/He selectivity is attainable after catalyst activation at 600^oC while producing H_2 with a purity of >99.9% over 350 hours of continuous operation under MSR/WGS conditions and 300 hours under pure H_2 testing conditions. The cumulative testing time of the membrane was 650 hours or one month.

The dual CMR was operated at a temperature of 475^oC, a pressure of 5 bar, steam-to-carbon ratios of 3 and 5 and gas hourly space velocities between 1,000 to 6,000 h^{-1}. This dual CMR showed higher methane conversion than the conventional reactor. Please notice that this effect, also known to be critically related to key process intensification objectives, was more noticeable at low space velocities. The CMR module had a DaPe number ranging between 0.5 to 1 demonstrating the effective membrane performance at the specified conditions. Furthermore, the dual CMR module showed a significant reduction in the CO content which was

shown to be the result of the subsequent “packing step” with the WGS catalyst introduced in the proposed module design.

6. Conclusions and Recommendations

6.1 Conclusions

Multitube palladium membrane modules that are suitable for IGCC systems are studied through 3-D Computational Fluid Dynamics (CFD) simulations generated and validated with the experimental test results. The shell-and-tube heat exchanger configuration multitube module based on a previously developed single tube module allows a high pure hydrogen productivity and at the same time, it aggregates high pressure CO_2 available for recycling, sequestration and/or conversion to useful industrial products. The study proved the feasibility of the multitube module with a total membrane surface area of 1050 cm^2 by studying the module performance including membrane permeability, hydrogen recovery, hydrogen purity and membrane usage under different operating conditions. The simulation study focused on the quantitative study of mass transfer limitations inside the module, concentration polarization, tube-to-tube performance difference and provided methods for mass transfer improvement: 1) Increase the convective force inside the module 2) Create recirculation by adding baffles to the module shell side. Between the two methods, adding baffles is preferable as it can hold the hydrogen recovery while it diminishes the concentration polarization. Furthermore, the CFD simulation was used to discover the scalability of the module by increasing the membrane surface area to 2850 cm^2. For scaled-up membrane modules, mass transfer limitation is an important parameter to consider as large modules showed severe concentration polarization effects. Overall, this project provided technical data for design and scale-up membrane module system, and complemented and enhanced the experimental testing of the membrane module.

Hydrogen productive reactions: ethanol steam reforming and methane steam reforming are discussed along with the implementation of catalytic membrane reactors (CMR). Experimental study of the process was carried out with a single membrane tube CMR with the catalysts packed on the shell side and the pure hydrogen collected from the tube side. Considering the effect of the catalyst particles on the transfer phenomena, both isothermal and non-isothermal 2-D CFD simulations were developed and validated with the experimental data. The advantage

of process intensification is proved by comparing the hydrogen production rate in both CMRs and traditional Packed Bed Reactors (PBRs) under the same operating conditions. As an effect of the endothermic property of the reaction along with the effect of continuously hydrogen removal, a “cold-spot” and methanation is observed from the simulation. It is found that applying “counter-current” sweep gas effectively reduced the area and the temperature drop inside the “cold-spot”, which is beneficial for the process as the reverse methane steam reforming is diminished. Furthermore, through the analysis of the different operating conditions, higher pressure and temperature is proposed to be beneficial to the process.

6.2 Suggestions

1. For the multitube membrane module, include a mechanism that can “close” a tube in the case of a leakage or burst on the tube so that the purity of the final product can be guaranteed.

2. The cage designed for the steam reforming process improved the reactor performance as it prevented the contact of the catalysts and the membrane surface. However, in the simulations, the effect of the cage to the flow pattern, heat and mass transfer is neglected. Thus, in order to improve the accuracy of the simulation, considering the cage within the model geometry is needed in future study.

3. Minor carbon deposition is observed in the experimental study. In our study, high steam to carbon ratio helps with reducing the carbon deposition, however, in order to simulate the process more accurately, considering the effect of the carbon deposition effect is recommended.

Nomenclature

C_p	Heat capacity	J/(kg·K)
d	Catalyst diameter	m
D_i^{eff}	Effective diffusion coefficient	m^2/s
$\mathfrak{D}_{AB}$	Binary diffusion coefficient	
Da	Damkohler number	1
F	Volume force	N/m^3
GHSV	Gas hourly space velocity	1
H_i	Enthalpy carried by hydrogen	kJ/mol
h_{fs}	Convective heat transfer coefficient	$W/(m^2K)$
I	Identity matrix	
k	Packed bed permeability	m^2
k_a, k_r	Axial and radial thermal conductivity	W/(m·K)
k_i	Reaction rate constant	varies
K_i	Equilibrium constant	varies
l	Palladium membrane thickness	um
LHSV	Liquid hourly space velocity	1
M_i	Molecular weight of component i	kg/mol
N	tube-to-particle diameter ratio	1
N_i	Flux of component i	$kg/(m^2 \cdot s)$
Nu	Nusselt number	1
P	Pressure	bar
P_i	Partial pressure of component i	bar
Pe_i	Péclet number	1
p_{H_2}	Hydrogen permeance	$Nm^3 \cdot m^{-2} \cdot h^{-1} \cdot bar^{-0.5}$
Pr	Prandtl number	1
Q_R	Heat generation of the reaction	kJ
r_i	Reaction rate	$mol\ g_{cat}^{-1} s^{-1}$
R	Gas constant	$J \cdot mol^{-1} K^{-1}$
R_i	Generation rate of component i	$mol\ g_{cat}^{-1} s^{-1}$

Re	Reynolds number	1
Sc	Schmidt number	1
T	Temperature	K
u	Linear velocity	m/s
w_i	Mass fraction of component i	1
X_i	Mole fraction of component i	1

Greek letters

β_F	Forchheimer coefficient	kg/m^4
ε_P	Packed bed porosity	1
$\Omega_{\mathfrak{D},AB}$	Collision integral	Å
μ	Fluid viscosity	$Pa \cdot s$
ρ	Density	kg/m^3
σ_{AB}	Lennard-Jones parameters	
τ	Tortuosity	1

Reference

Aboelsoud, W. 2013. "Study Of Transport Phenomena In Carbon-based Materials." *PhD dissertation, Central Florida University.*

Aboudheir A., Akande A., Idem R., Dalai A. 2006. "Experimental studies and comprehensive reactor modeling of hydrogen production by the catalytic reforming of crude ethanol in a packed bed tubular reactor over a Ni/Al2O3 catalyst." *Int. J. Hydrogen Energy* 752-761.

Abu El Hawa H. W.; Paglieri S. N.; Morris C. C.; Harale A.; Way J. D.; 2015. " Application of a Pd–Ru composite membrane to hydrogen production in a high temperature membrane reactor." *Sep. Purif. Technol* 388-397.

Adhikari S.; Fernando S.; 2006. "H2 Membrane Separation Techniques." *Ind. Eng. Chem. Res.* 875-881.

Ahmad A. L., Lau K. K., Abu Bakar MZ, and Abd Shukor SR, 2005. "Integrated CFD simulation of concentration polarization in narrow membrane channel. ." *Computers & chemical engineering* 2087-2095.

Akpan E.; Akande A.; Aboudheir A.; Ibrahim H.; Idem R.; 2007. "Experimental, kinetic and 2-D reactor modeling for simulation of the production of H2 by the catalytic reforming of concentrated crude ethanol (CRCCE) over a Ni-based commercial catalyst in a packed-bed tubular reactor." *Chem. Eng. Sci.* 3112-3126.

Al-Mufachi N.A.; Rees N.V.; Steinberger-Wilkens R.; 2015. "Hydrogen selective membranes: A review of palladium-based dense metal membranes." *Renewable and Sustainable Energy Reviews* 540-551.

Atwood K., Arnold M.R., Appel E.G.,. 1950. "Water gas shift reaction: Effect of pressure on rate over an iron- oxide-chromium oxide catalyst." *Ind. Eng. Chem* 1600-1602.

Augustine A. S., Ma Y. H., Kazantzis N. K., 2011. "High pressure palladium membrane reactor for the high temperature water–gas shift reaction." *Int. J. Hydrogen Energy* 5350-5360.

Ayturk M.E.; kazantzis N.K.; Ma Y.H.; 2009. "Modeling and performance assesment of Pd- and Pd-Au-based catalytic membrane reactors for hydrogen production." *Energy Environ* 430-438.

Barbieri G.; Violante V.; Di Maio F.P.; Criscuoli A.; Drioli E.; 1997. "Methane steam reforming analysis in a palladium-based catalytic membrane reactor." *Ind. Eng. Chem. Res* 3369-3374.

Basile A., Pinacci P., Iulianelli A., Broglia M., Drago F., Liguori S., Longo T., and Calabrò V.. 2011. "Ethanol steam reforming reaction in a porous stainless steel supported palladium membrane reactor." *Int. J. Hydrogen Energy* 2029-2037.

Battersby S.; Teixeira P.W.; Beltramini J.; Duke M.C.; Rudolph V.; Diniz da Costa J.C; 2006. "An analysis of the Peclet and Damkohler numbers for dehydrogenation reactions using molecular sieve silica (MSS) membrane reactors ." *Catal. Today* 12-17.

Beurden, P. Van. 2004. *On the catalytic aspect of steam-methane reforming.* Energy Research Centre of the Netherlands (ECN).

Bi Y.; Xu H. Li W.; Goldbach A.; 2009. "Water–gas shift reaction in a Pd membrane reactor over Pt/Ce0.6Zr0.4O2 catalyst." *Int. J. Hydrogen Energy* 2965-2971.

Bird R.B.; Stewart W.E; Lightfoot E.N.; 2007. *Transport Phenomena, second ed.* John Wiley & Sons.

Boon J.; Pieterse J.A.Z.; van Berkel F.P.F.; van Delft Y.C.; van Sint Annaland M.;2015. "Hydrogen ermeation through palladium membranes and inhibition by carbon monoxide, carbon dioxide, and steam." *J. Membr. Sci* 344-358.

Brunetti A., Caravella A., Fernandez E., Pacheco Tanaka D.A., Gallucci F., Drioli E., Curcio E., Viviente J.L., Barbieri G., 2015. "Syngas upgrading in a membrane reactor with thin Pd-alloy supported membrane." *Int. J. Hydrogen Energy* 10883-1089.

Bshish A., Yakoob Z., Narayanan B., Ramakrishnan R., Ebshish A.. 2011. "Steam-reforming of ethanol for hydrogen production." *Chem. Pap* 251-266.

Camara G. A.; Ticianelli E. A.; Mukerjee S.; Lee S. J.; McBreen J.; 2002. "The CO poisoning mechanism of the H2 oxidation reaction in proton exchange membrane fuel cells. ." *J. Electrochem. Soc.* A748-A753.

Caravella A., and Sun Y.. 2016. "Correct evaluation of the effective concentration polarization influence in membrane-assisted devices. Case study: H 2 production by Water Gas Shift in Pd-membrane reactors." *International Journal of Hydrogen Energy* 11653-11659.

Caravella A., Barbieri G., and Drioli E.. 2009. "Concentration polarization analysis in self-supported Pd-based membranes. ." *Separation and Purification Technology* 613-624.

Caravella A., Melone L., Sun Y., Brunetti A., Drioli E., Barbiri G., 2016. "Concentration polarization distribution along Pd-based membrane reactors: A modelling approach applied to Water-Gas Shift. ." *Int J Hydrogen Energy* 2660-2670.

Castro-Dominguez B., Mardilovich I. P., Ma L. C., Ma R., Dixon A. G., Kazantzis N. K., and Ma Y. H., 2016. "Integration of methane steam reforming and water gas shift reaction in a Pd/Au/Pd-based catalytic membrane reactor for process intensification." *Membranes.*

Catalano J., Guazzone F., Mardilovich I.P., Kazantzis N. K., and Ma Y.H.. 2012. "Hydrogen production in a large scale water–gas shift Pd-based catalytic membrane reactor ." *Industrial & Engineering Chemistry Research* 1042-1055.

Caygill G.; Zanfir M., Gavriilidis A.; 2006. "Scalable reactor design for pharmaceuticals and fine chemicals production 1: Potential scale-up obstacles." *Org. Process Res. Dev.* 539−552.

Chang H.F.; Pai W.J.; Chen Y.J.; Lin W.H.; 2010. "Autothermal reforming of methane for producing high-purity hydrogen in a Pd/Ag membrane reactor." *Int J Hydrogen Energ* 12986-12992.

Chein R.Y.; Chen Y.C.; Chyou Y.P.; Chung J.N.; 2014. "Three-dimensional numerical modeling on high pressure membrane reactors for high temperature water-gas shift reaction." *Int J Hydrogen Energ* 15517-15529.

Chen C.H., Ma Y.H.; 2010. "The effect of H2S on the performance of Pd and Pd/Au composite membrane." *J. Memb Sci.* 535-544.

Chen W. H.; Syu W. Z.; Hung C. I.; Lin Y. L.; Yang C.C.; 2013. "Influences of geometry and flow pattern on hydrogen separation in a Pd-based membrane tube." *Int. J. Hydrogen Energy* 1145-1156.

Chen W.H. Syu W.Z.; Hung C.I.; Lin Y.L.; Yang C.C.; 2012. "A numerical approach of conjugate hydrogen permeation and polarization in a Pd membrane tube." *Int. J. Hydrogen Energy* 12666-12679.

Coroneo M.; Montante G.; Catalano J.; Paglianti A.; 2009. "Modelling the effect of operating conditions on hydrodynamics and mass transfer in a Pd–Ag membrane module for H 2 purification." *J. Membr. Sci.* 34-41.

Coroneo M.; Montante G.; Giacinti Baschetti M.; Paglianti A.; 2009. "CFD modeling of inorganic membrane modules for gas mixture separation." *Chem. Eng. Sci.* 1085-1094.

Coroneo M.; Montante G.; Paglianti A.; 2010. "Numerical and experimental fluid-dynamic analysis to improve the mass transfer performances of Pd− Ag membrane modules for hydrogen purification." *Ind. Eng. Chem. Res.* 9300-9309.

Coroneo M; Montante G.; Paglianti A.; 2010. "Numerical and experimental fluid-dynamic analysis to improve the mass transfer performances of Pd− Ag membrane modules for H2 purification." *Ind. Eng. Chem. Res* 9300-9309.

Delgado J. M. P. Q, 2006. "A critical review of dispersion in packed beds." *Heat and mass transfer* 279-310.

de-Souza M.,; G.M. Zanin, F.F. Moraes. 2013. "Parametric study of hydrogen production from ethanol steam reforming in a membrane microreactor." *Braz. J. Chem. Eng* 355-367.

Diniz da Costa J.C.; Reed G.P.; Thambimuthu K.; 2009. "High Temperature Gas Separation Membranes in Coal Gasification." *Proceedings of the 9th International Conference on Greenhouse Gas Control Technologies1.* 295-302.

Dixon A.G., 2003. "Recent research in catalytic inorganic membrane reactors." *Int. J. Chem. Reactor Eng* 1-35.

Dixon, A.G. 2012. "Fixed bed catalytic reactor modelling—the radial heat transfer problem. ." *Can J Chem Eng* 507-527.

Doney, Scott C., Victoria J. Fabry, Richard A. Feely, and Joan A. Kleypas. 2009. "Ocean acidification: the other CO2 problem." *Marine Science.*

Du W.; Wang Q.; Saxner D.; Deskins N. A.; Su D.; Krzanowski J.E.; Anatoly I.F.; Teng X.; 2011. "Highly active Iridium/Iridium–Tin/Tin oxide heterogeneous nanoparticles as alternative electrocatalysts for the ethanol oxidation reaction." *J. Amer. Chem. Soc.* 15172-15183.

Fernandez E.; Helmi A.; Coenen K.; Melendez J.; Viviente J.L.; Tanaka D.A.P.; van Sint Annaland M.; Gallucci F.; 2015. "Development of thin Pd–Ag supported membranes for fluidized bed membrane reactors including WGS related gases." *Int. J. Hydrogen Energy* 3506-3519.

Fogler H.S.; 2005. *Elements of Chemical Reaction Engineering. Fourth ed.* New Jersey: Prentice hall.

Gade S.K.; Payzant E.A.; Park H.J.; Thoen P.M.; Way J.D.; 2009. "The effects of fabrication and annealing on the structure and hydrogen permeation of Pd–Au binary alloy membranes." *J. Membr. Sci* 227-233.

Gallucci F.; Basile A. 2008. "Pd–Ag membrane reactor for steam reforming reactions: a comparison between different fuels." *Int. J. Hydrogen Energy* 1671-1687.

Gallucci F.; Basile A.; Tosti S.; Iulianelli A.; Drioli E.. 2007. "Methanol and ethanol steam reforming in membrane reactors: An experimental study." *Int. J. Hydrogen Energy* 1201-1210.

Gallucci F.; Paturzo L.; Famà L. A.; Basile A.; 2004. "Experimental study of the methane steam reforming reaction in a dense Pd/Ag membrane reactor." *Ind. Eng. Chem.* 928-933.

Gallucci F.; van Sint Annaland M.; Kuipers J.A.M.; 2010. "Pure hydrogen production via autothermal reforming of ethanol in a fluidized bed membrane reactor: a simulation study." *Int. J. Hydrogen Energy* 1659-1668.

Grashoff G. J.; Pilkington C. E.; and Corti C. W.; 1983. "The purification of H2. ." *Platinum Metals Review* 157-169.

Gryaznov V.; 2000. "Metal containing membranes for the production of ultrapure hydrogen and the recovery of hydrogen isotopes. ." *Sep. Purif. Methods* 171-187.

Guazzone F., Catalano J., Mardilovich I.P., Wu T., Lambrecht R. C., Datta S., Kniep J., Pande S., Kazantzis N. K., Ma Y. H.. 2013. "Enhancement of the long-term permeance, selectivity stability, and recoverability of Pd–Au membranes in coal derived syngas atmospheres." *Energy & Fuels* 4150-4160.

Guazzone F.; Catalano J.; Mardilovich I.P.; Kniep J.; Pande S.; Wu T.; Lambrecht R.C.; Datta S.; Kazantzis N. K.; and Ma Y.H.. 2012. "Gas permeation field tests of composite Pd and Pd–Au membranes in actual coal derived syngas atmosphere." *International Journal of Hydrogen Energy* 14557-14568.

He G.; Mi Y.; Yue P.L.; Chen G.; 1999. "Theoretical study on concentration polarization in gas separation membrane processes." *J. Membr. Sci* 243-258.

Hedayati A., Le Corre O., Lacarrière B., Llorca J., 2016. "Experimental and exergy evaluation of ethanol catalytic steam reforming in a membrane reactor." *Catal. Today* 68-78.

Helmi A., Fernandez E., Melendez J., Tanaka D.A.P., Gallucci F., van Sint Annaland M., 2016. "Fluidized bed membrane reactors for ultra pure H2 production- a step forward towards commercialization ." *Molecules* 376-394.

Hou K., Hughes R.. 2002. "The effect of external mass transfer, competitive adsorption and coking on H2 permeation through thin Pd/Ag membranes." *J. Membr. Sci* 119-130.

Ismail A.F., Khulbe K., Matsuura T., 2015. "Gas Separation Membranes: Polymeric and Inorganic." *Science*.

Iulianelli A., Liguori S., Vita A., Italiano C., Fabiano C., Huang Y., and Basile A.. 2016. "The oncoming energy vector: hydrogen produced in Pd-composite membrane reactor via bioethanol reforming over Ni/CeO2 catalyst." *Catalysis Today* 368-375.

Jorgensen S.L.; Nielsen P.E.H.; Lehrmann P.; 1995. "Steam reforming of methane in a membrane reactor." *Catal. Today* 303-307.

Kahn, Brian. 2014. "Another year, Another Record High for Greenhouse Gases." *Climate Central.*

Kikuchi E.; Nemoto Y.; Kajiwara M.; Uemiya S.; Kojima T.; 2000. "Steam reforming of methane in membrane reactors: comparison of electroless-plating and CVD membranes and catalyst packing modes." *Catal. Today* 75-81.

Koc R.;. Kazantzis N. K; Ma Y. H.;. 2014. "Membrane technology embedded into IGCC plants with CO 2 capture: An economic performance evaluation under uncertainty." *Int.J. Greenhouse Gas Control* 22-38.

Kolios G.; Glöckler B.; Gritsch A.; Morillo A.; Eigenberger G.. 2005. "Heat-Integrated Reactor Concepts for Hydrogen Production by Methane Steam Reforming." *Fuel Cells* 52-65.

Kumar A, Prasad R., Sharma Y.C.. 2014. "Steam reforming of ethanol: production of renewable hydrogen." *Int. J. Environ.Res. Dev* 203-212.

Li A., Liang W., Hughes R., 2000. "The effect of carbon monoxide and steam on the hydrogen permeability of a Pd/stainless steel membrane." *J. Membr. Sci.* 135-141.

Lin Y.M., Liu S. L., Chuang C.H., Chu Y. T.; 2003. " Effect of incipient removal of hydrogen through palladium membrane on the conversion of methane steam reforming: Experimental and modeling." *Catal. Today* 127-139.

Lu G.Q.; Diniz da Costa J.C.; Duke M.; Giessler S.; Socolow R.; Williams R.H.; Kreutz T.; 2007. "Inorganic membranes for hydrogen production and purification: A critical review and perspective." *J. Colloid Inter. Sci.* 589-603.

Ma L.C., Castro-Dominguez B., Kanzantzis N.K., Ma Y.H.. 2015. " Integration of membrane technology into hydrogen production plants with CO2 capture: An economic performance assessment study." *Int. J. Greenh. Gas Control* 424-438.

Ma R., Castro-Dominguez B., Mardilovich I. P., Dixon A.G., and Ma Y.H., 2016. "Experimental and simulation studies of the production of renewable hydrogen through ethanol steam reforming in a large-scale catalytic membrane reactor." *Chemical Engineering Journal* 302-313.

Ma R.; Castro-Dominguez B; Dixon A. G.; and Ma Y.H.; 2017. "CFD study of heat and mass transfer in ethanol steam reforming in a catalytic membrane reactor ." *International journal of hydrogen energy* https://doi.org/10.1016/j.ijhydene.2017.08.173.

Ma Y.H., Mardilovich I.P., Engwall E.E., Composite gas separation modules having intermediate porous metal layer. . 2007. US Patent US Patent No. 7,175,694.

Ma Y.H., Mardilovich I.P., Engwall E.E.,. 2007. US Patent Patent 7,172,644.

Ma Y.H., Mardilovich I.P., Engwall E.E.. 2007. US Patent Patent 7,255,726 .

Ma Y.H., Mardilovich I.P., Engwall E.E.. 2008. US Patent Patent 7,390,536.

Ma Y.H., Mardilovich P.P., She Y.. 2000. US Patent Patent 6,152,987.

Ma Y.H.; Guazzone F.,. 2010. Methods. U.S. Patent 7,727,596.

Ma, L.C. 2014. "Pd-based catalytic membrane reactor technology option for H2 production: a techno-economic performance study in the presence of uncertainty. ." *A Ph.d thesis proposal .*

Mardilovich I.P.; Castro-Dominguez B.; Kazantzis N.K.; Wu T.; Ma Y.H.; 2015. "A comprehensive performance assessment study of pilot-scale Pd and Pd/alloy membranes under extended coal-derived syngas atmosphere testing." *Int. J Hydr Energy* 6107-6117.

Mardilovich P.P.; She Y.; Ma Y.H.; 1998. "Defect-free palladium membrane on porous stainless-steel support." *AICHE J.* 310-322.

Marigliano G.; Barbieri G.; Drioli E.; 2001. "Effect of energy transport on a palladium-based membrane reactor for methane steam reforming process." *Catal Today* 85-99.

Mas V.M; Bergamini L.; Baronetti G.; Amadeo N.; Laborde M.; 2008. "A kinetic study of ethanol steam reforming using a nickel based catalyst." *Top. Catal.* 39-48.

Mathure P.V; Ganguly S; Patwardhan A.V.; Saha R.K.; 2007. "Steam reforming of ethanol using a commercial nickel-based catalyst." *Ind. Eng. Chem. Res* 8471-8479.

Matthias, C. H. 2009. "Membrantechnik im Peripheriebereich von Brennstoffzellenfahrzeugen." *Shaker.*

McKinley D.L.; Nitro W.V., Method for hydrogen separation and purification,. 1966. U.S. Patent 3,247,648.

Medrano J.A.; Fernandez E.; Melendez J.; Parco M.; Tanaka D.A.P.; van Sint Annaland M.; Gallucci F. 2016. "Pd-based metallic supported membranes: High-temperature stability and fluidized bed reactor testing, ." *Int. J. Hydrogen Energy* 8706-8718.

Mendes D., Chibante V., Zheng J.M., Tosti S., Borgognoni F., Mendesa A., Madeira L.M.; 2010. "Enhancing the production of hydrogen via water–gas shift reaction using Pd-based membrane reactors." *Int. J. Hydrogen Energy* 12596-12608.

Mori N.; Nakamura T.; Noda K;, Sakai O.; Takahashi A.; Ogawa N.; Sakai H.; Iwamoto Y.; and Hattori T.; 2007. "Reactor configuration and concentration polarization in methane steam reforming by a membrane reactor with a highly hydrogen-permeable membrane." *Industrial & Engineering Chemistry Research* 1952-1958.

Mourgues A., and Sanchez J..2005. "Theoretical analysis of concentration polarization in membrane modules for gas separation with feed inside the hollow-fibers." *Journal of membrane science* 133-144.

Murmura M. A., Patrascu M., Annesini M.C. V., Palma, C. Ruocco, M. Sheintuch,. 2015. "Directing selectivity of ethanol steam reforming in membrane reactors. ." *Int. J. Hydrogen Energy* 5837-5848.

Murmura M.A., Diana M., Spera R., Annesini M.C.. 2016. "Modeling of autothermal methane steam reforming: Comparison of reactor configurations." *Chem Eng Process* 125-135.

Murmura M.A., Patrascu M., Annesini M.C., Palma V., Ruocco C., Sheintuch M.. 2015. "Directing selectivity of ethanol steam reforming in membrane reactors." *Int. J. Hydrogen Energy* 5837-5848.

Nenoff T.M.; Spontak R.J; and Aberg C.M.; 2006. "Membranes for Hydrogen Purification: An Important Step toward a Hydrogen-Based Economy." *MRS Bulletin* 735-744.

Olafadehan O;, Ayoola A.; Akintunde O.' Adeniyi V.; 2015. "Mechanistic kinetic models for steam reforming of concentrated crude ethanol on Ni/Al2O3 catalyst." *J. Eng. Sci. &Tech* 633-653.

Palma V.; Castaldo F.; Iaquaniello G. Ciambelli P.; 2012. "Sustainable hydrogen production by catalytic bio-ethanol steam reforming." In *Greenhouse Gases - Capturing, Utilization and Reduction*, by Ed. G. Liu, Ch.7. INTECH Open Access Publisher.

Papadias D.D., Sheldon H.D.L., Ferrandon M., Ahmed S.; 2010. " An analytical and experimental investigation of high-pressure catalytic steam reforming of ethanol in a hydrogen selective membrane reactor." *Int. J. Hydrogen Energy* 2004-2017.

Parsley D.; Ciora Jr. R.J.; Flowers D.L.; Laukaitaus J.; Chen A.; Liu P.K.T.; Yu J.; Sahimi M.; Bonsu A.; Tsotsis T.T.; 2014. "Field evaluation of carbon molecular sieve membranes for the separation and purification of hydrogen from coal- and biomass-derived syngas." *J. Memb Sci* 81-92.

Patel M., Jindal T.K., Pant K.K.. 2013. "Kinetic study of steam reforming of ethanol on Ni-based Ceria–Zirconia catalyst." *Ind. Eng. Chem. Res* 15763-15771.

Patrascu M., Sheintuch M.. 2015. "On-site pure hydrogen production by methane steam reforming in high flux membrane reactor: Experimental validation, model predictions and membrane inhibition." *Chem. Eng. J.* 862-874.

Peela N.R.; Kunzru D.; 2011. "Steam reforming of ethanol in a microchannel reactor: kinetic study and reactor simulation." *Ind. Eng. Chem. Res* 12881-12894.

Peters T.A.; Stange M.; Klette H.; Bredesen R.; 2008. "High pressure performance of thin Pd–23%Ag/stainless steel composite membranes in water gas shift gas mixtures; influence of dilution, mass transfer and surface effects on the hydrogen flux ." *J. Membr. Sci* 119-127.

Piemonte V., De Falco M., Favetta B., and Basile A; 2010. "Counter-current membrane reactor for WGS process: membrane design. ." *Int J Hydrogen Energ* 12609-12617.

Ravanchi, M.T., Kaghazchi, T. and Kargari, A., 2009. Application of membrane separation processes in petrochemical industry: a review. Desalination, 235(1-3), pp.199-244.

Richardson C. J, Nassehi V., 2003. "Finite element modelling of concentration profiles in flow domains with curved porous boundaries. ." *Chem. Eng. Sci.* 2491-2503.

Roldán, R. 2015. "Technical and economic feasibility of adapting an industrial steam reforming unit for production of hydrogen from renewable ethanol." *Int. J. Hydrogen Energy* 2035-2046.

Rosen, M. 2015. "The Prospects for Renewable Energy through Hydrogen Energy Systems." *Journal of Power and Energy Engineering,* 373-377.

Rostrup-Nielsen J.R.; Hansen J.H.B.;. 1993. "CO2-Reforming of methane over transition metals." *J. Catalysis* 38-49.

Ryi S.K.; Lee S.W.; Oh D.K., Seo B.S., Park J.W., Park J.S., Lee D.W., Kim S.S.; 2014. "Electroless plating of Pd after shielding the bottom of planar porous stainless steel for a highly stable H2 selective membrane." *J Membr Sci* 93–99.

Sahoo D.R.; Vajpai S.; Patel S.; K.K. Pant, 2007. " Kinetic modeling of steam reforming of ethanol for the production of hydrogen over Co/Al2O3 catalyst." *Chem. Eng. J.* 139-147.

Sanders D.F.; Smith Z.P.; Guo R.; Robeson L.M.; McGrath J.E.; Paula D.R.; Freeman B.D.; 2013. "Energy-efficient polymeric gas separation membranes for a sustainable future: A review." *Polymer* 4729-4761.

Shu J.; Grandjean B.P.A.; Kaliaguine S.; 1995. "Asymmetric Pd-Ag/stainless steel catalytic membranes for methane steam reforming." *Catal. Today* 327-332.

Sidhu TPK.; Govil A.; Roy S.; 2017. "Optimal monolithic configuration for heat integrated ethanol steam reformer." *Int J Hydrogen Energ* 7770-7785.

Sonwane C.G., Wilcox J., Ma Y.H., 2006. "Achieving optimum hydrogen permeability in PdAg and PdAu alloys." *J. Chem. Phys* 1-10.

Sun J.; Qiu X.P.; Wu F.; Zhu W.T.; 2005. "H2 from steam reforming of ethanol at low temperature over Ni/Y2O3, Ni/La2O3 and Ni/Al2O3 catalysts for fuel-cell application ." *Int. J. Hydrogen Energy* 437-445.

Thompson, Andrea. 2015. "2015 Begins With CO2 above 400 PPM Mark." *Climate Central.*

Tong J.; Matsumura Y;. 2006. "Pure hydrogen production by methane steam reforming with hydrogen-permeable membrane reactor." *Catal. Today* 147-152.

Tosti S.; Basile A. Bettinali L.; Borgognoni F.; Gallucci F.; Rizzello C.; 2008. "Design and process study of Pd membrane reactors." *Int. J Hydr Energy* 5098-5105.

Tosti S.; Basile A.; Borgognoni F.; Capaldo V.; Cordiner S.,; S. Di Cave, F. Gallucci, C. Rizzello, A. Santucci, and E. Traversa. 2008. "Low temperature ethanol steam reforming in a Pd-Ag membrane reactor: Part 1: Ru-based catalyst." *J. Membr. Sci.* 250-257.

Tosti S.; Basile A.; Borgognoni F.; Capaldo V.; Cordiner S.; Di Cave S.; Gallucci F.; Rizzello C; Santucci A.; Traversa E.; 2008. "Low-temperature ethanol steam reforming in a Pd–Ag membrane reactor: Part 2. Pt-based and Ni-based catalysts and general comparison." *J. Membr. Sci.* 258-263.

U.S. Energy Information Administration (U.S. EIA). 2014. "Annual Energy Outlook 2014 with projections to 2040." http://www.eia.gov/forecasts/aeo/pdf/0383(2014).pdf.

U.S. Office of Energy Efficiency & Renewable Energy. Available online. 2016 March 1. http://energy.gov/eere/fuelcells/hydrogen-production-natural-gas-reforming.

U.S. Office of Energy Efficiency and Renewable Energy. n.d. "H2 Production: Natural Gas Reforming." http://energy.gov/eere/fuelcells/H2-production-natural-gas-reforming.

Uemiya S.; 1999. "State of the art of supported metal membranes for gas separation. ." *Sep. Purif. Methods* 51-85.

Uemiya S.; Sato N.; Ando H.; Kikuchi E.; 1991. "The water gas shift reaction assisted by a palladium membrane reactor." *Ind. Eng. Chem. Res* 585-589.

Uriz I.; Arzamendi G.; López E.; Llorca J.; Gandía L. M.; 2011. "Computational fluid dynamics simulation of ethanol steam reforming in catalytic wall microchannels." *Chem. Eng. J.* 603-609.

Vásquez Castillo J. M.; Sato T.; Itoh N.; 2015. " Effect of temperature and pressure on hydrogen production from steam reforming of biogas with Pd–Ag membrane reactor." *Int. J. Hydrogen Energy* 3582-3591.

Völler J.; Follmann M.; Bayer C.; Melin T., 2009 "Model Development and Implementation of a Membrane Shift Reactor. ."

Vortmeyer, D. 1975. "Axial heat dispersion in packed beds. ." *Chem Eng Sci* 999-1001.

Ward T. L.; Dao T.; 1999. "Model of hydrogen permeation behavior in palladium membranes." *Journal of Membrane Science* 211-231.

Wellington S.L.; Matzakos A.N.; Mardilovich I.P.; Ma Y.H.; Engwall E.E.; Membrane enhanced reactor. 2006. Patent US Patent WO 2006034086 A1.

Wenten I. G; Khoiruddin K.; Aryanti P. T. P.; and Hakim A. N.; 2016. "Scale-up Strategies for Membrane-Based Desalination Processes: A Review." *Journal of Membrane Science and Research 2* 42-58.

Xu J., Froment G.F.; 1989. "Methane steam reforming, methanation and water-gas shift: I. Intrinsic kinetics." *AIChE J* 88-96.

Yang M., Liu M., Yu D., Zheng J., Wu Z., Zhao S., Chang J., and Wei Y.. 2017. "Numerical simulation of scaling-up for AEC-MBRs regarding membrane module configurations and cyclic aeration modes. ." *Bioresource technology* 933-943.

Yun S; Oyama, S.T., 2011. Correlations in palladium membranes for hydrogen separation: a review. Journal of membrane science, 375(1-2), pp.28-45.

Zanfir M., Baldea M., Daoutidis P.. 2011. "Optimizing the catalyst distribution for countercurrent methane steam reforming in plate reactors." *AIChE J.* 2518-2528.

Zhai X.; Ding S.; Cheng Y.; Jin Y.; Cheng Y.; 2010. "CFD simulation with detailed chemistry of steam reforming of methane for hydrogen production in an integrated micro-reactor." *Int. J. Hydrogen Energy* 5383-5392.

Zhang J.; Liu D. Y.; He M. F; Xu H.Y.; and Li W. Z.; 2006. "Experimental and simulation studies on concentration polarization in H 2 enrichment by highly permeable and selective Pd membranes." *Journal of membrane science* 83-91.

Zhang J.; Liu D.; He M.; Xua H.; Li W; 2006. "Experimental and simulation studies on concentration polarization in H2 enrichment by highly permeable and selective Pd membranes." *J. Membr. Sci.* 83-91.

Appendix:

1D simulation code:

```
#Constants
Rho = 1.35E6                          # unit [gcat/m^3]
Am = 3.14*((0.038/2)^2-(0.028/2)^2)  # unit [m^2]

#Definitions

#Reaction rate constant
k2 = (4.55E-5/T)*exp(-2030*(1/T))
k3 = 5.43E-3*exp(-8074.33*(1/T))
k4 = 3.711E14*exp(-28879*(1/T))
k5 = 8.960E13*exp(-29336.1*(1/T))

K3 = exp(4400/T-4.036)
K4 = 1E10*exp(-26830/T+30.114)
K5 = K3*K4
KCO = 8.23E-10*exp(8497.71*(1/T))
KM = 6.64E-9*exp(4604.28*(1/T))
KH = 6.12E-14*exp(9971.13*(1/T))
KW = 1.77E5*exp(-10666.35*(1/T))

FT = FW+Fe+FM+FCO+FCO2+FH
yW = FW/FT          # Water mole fraction
ye = Fe/FT          # EtOH mole fraction
```

```
yM = FM/FT          # Methane mole fraction
yCO = FCO/FT        # CO mole fraction
yCO2 = FCO2/FT      # CO2 mole fraction
yH = FH/FT          # H2 mole fraction
Ph2 = yH*P          # H2 partial pressure at retentate side

FFT = Fe+FM+FCO+FCO2+FH
yye = Fe/FFT        # EtOH dry basis mole fraction
yyM = FM/FFT        # Methane dry basis mole fraction
yyCO = FCO/FFT      # CO dry basis mole fraction
yyCO2 = FCO2/FFT    # CO2 dry basis mole fraction
yyH = FH/FFT        # H2 dry basis mole fraction

# Variables

T = 450+273                                 # unit [K]
Rg = 8.314                                  # unit [KJ/kmol K]
P = 3E5                                     # unit [pa]
Fpurge = 0.00004836                         # Purge mole flow rate, unit [mol/s]   65[sccm]
Pper = (Fper_H2/(Fper_H2+Fpurge))*1E5       # Tube side H2 partial pressure unit[pa]

l(0) = 0            # unit [m]
l(f) = 0.4064       # unit [m]

r2 = k2*P*ye                                                    # unit [mol ethanol/g cat s]
r3 = k3*P / (yH*den^2)  *  (  yCO*yW - (yCO2*yH/K3)  )          # unit [mol ethanol/g cat s]
```

```
r4 = k4/(yH^2.5*den^2*P^0.5) * (yM*yW - (yCO*yH^3*P^2/K4))      # unit [mol ethanol/g cat s]

r5 = k5/(yH^3.5*den^2*P^0.5) * (yM*yW^2 - (yCO2*yH^4*P^2/K5))   # unit [mol ethanol/g cat s]

den = 1 + P*(KCO*yCO+KH*yH+KM*yM) + KW*yW/yH


Mh2 = 859                                   # H2 permeance [mol/m^2-h-atm^0.5]


d(FW) / d(l) = (-r3-r4-2*r5)*0.8*Rho*Am

FW(0) =0.000318159      # Initial value [mol/s]

d(Fe) / d(l) = -r2*0.8*Rho*Am

Fe(0) = 0.000106053      # Initial value [mol/s]

Fe0 = 0.000106053        # Initial value [mol/s]

d(FCO) / d(l) = (r2-r3+r4)*0.8*Rho*Am

FCO(0) = 0               # Initial value [mol/s]

d(FCO2) / d(l) = (r3+r5)*0.8*Rho*Am

FCO2(0) = 0              # Initial value [mol/s]

d(FH)/d(l) = (r2+r3+3*r4+4*r5)*0.8*Rho*Am - 3.14 * (0.028) * Mh2 /3600* ( (Ph2/1E5/1.01325)^0.5 - (Pper/1E5/1.01325)^0.5 )

FH(0) = 1E-20            # Initial value [mol/s]

d(Fper_H2)/d(l) = 3.14 * (0.028) * Mh2/3600 * ( (Ph2/1E5/1.01325)^0.5 - (Pper/1E5/1.01325)^0.5 )  Fper_H2(0) = 1E-25      # Initial value [mol/s]


d(FM)/d(l) = (r2-r4-r5)*0.8*Rho*Am

FM(0) = 0                # Initial value [mol/s]

X = (Fe0-Fe)/(Fe0)       # Ethanol Conversion

YH = (FH+Fper_H2)/Fe0    # H2 yield

YM = FM/Fe0              # Methane yield
```

```
YCO2 = FCO2/Fe0          # CO2 yield
YCO = FCO/Fe0            # CO yield
```